Optimising the benefits of spectral x-ray imaging in material decomposition

A thesis submitted in partial fulfilment
of the requirements for the Degree of
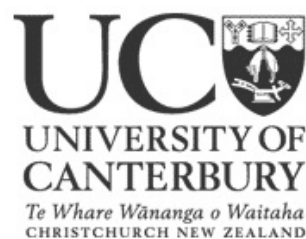
Doctor of Philosophy

in Medical Physics

by

Syen Jien Nik

Department of Physics and Astronomy

University of Canterbury

Christchurch, New Zealand

2013

UC

UNIVERSITY OF
CANTERBURY
Te Whare Wānanga o Waitaha
CHRISTCHURCH NEW ZEALAND

Abstract

The extra energy information provided by spectral x-ray imaging using novel photon counting x-ray detectors may allow for improved decomposition of materials compared to conventional and dual-energy imaging. The information content of spectral x-ray images, however, depends on how the photons are grouped together. This thesis deals with the theoretical aspect of optimising material discrimination in spectral x-ray imaging. A novel theoretical model was developed to map the confidence region of material thicknesses to determine the uncertainties in thickness quantification. Given the thickness uncertainties, photon counts per pixel can be optimised for material quantification in the most dose efficient manner. Minimisation of the uncertainties enables the optimisation of energy bins for material discrimination.

Using Monte Carlo simulations based on the BEAMnrc package, material decomposition of up to 3 materials was performed on projection images, which led to the validation of the theoretical model. With the inclusion of scattered radiation, the theoretical optima of bin border energies were accurate to within $2\,\mathrm{keV}$. For the simulated photon counts, excellent agreement was achieved between the theoretical and the BEAMnrc models regarding the signal-to-noise ratio in a decomposed image, particularly for the decomposition of two materials.

Finally, this thesis examined the implementation of the Medipix detector. The equalisation of pixel sensitivity variations and the processing of photon counting projection images were studied. Measurements using the Medipix detector demonstrated promising results in the charge summing and the spectroscopic modes of acquisition, even though the

spectroscopic performance of the detector was relatively limited due to electronic issues known to degrade the equalisation process.

To conclude, the theoretical model is sufficient in providing guidelines for scanning parameters in spectral x-ray imaging and may be applied on spectral projection measurements using e.g. the redesigned MedipixRX detector with improved spectroscopic performance, when it becomes available.

Acknowledgements

Having two Senior Supervisors departing the University of Canterbury during the course of this thesis was somewhat unfortunate, yet I am grateful to have worked with all of the three Senior Supervisors. I would like to thank Richard Watts for his ideas on the theoretical model. I am indebted to Juergen Meyer, who has been a pleasure to work with. This thesis would not have been possible without his mentorship. My appreciation also goes to Phil Butler and Anthony Butler for the opportunities I have had with the MARS research team.

I gratefully acknowledge Rune Thing for his contribution on the simulation model and I would like to mention the colleagues in the MARS group, past and present, who have all contributed toward developing the spectral CT imaging system. Both works were necessary for the progress of this thesis.

I wish to thank James Robar and Laurent Kreplak (both from the Dalhousie University in Halifax, Canada) for making the internship on truncated CT data reconstruction possible after the Canterbury earthquakes.

Finally, and most importantly, I would like to express my deepest feelings to my family and my newly wedded wife Sandy.

Contents

List of Figures

LIST OF FIGURES

List of Tables

Chapter 1

Introduction

X-rays were discovered by Wilhelm Conrad Roentgen in 1895 and in one of his experiments the very first x-ray image was produced. For over a century since, x-rays have been an indispensable imaging tool in many applications, including in security screening, in non-destructive testing and, in particularly, in medical imaging in the form of radiography and computed tomography (CT). In the United States, approximately 62 million CT scans were conducted in 2006 (Mettler et al. 2008, McCollough et al. 2009). The number of general radiography procedures in the United States in 2006 was about 324 million, including 129 million chest x-ray and 34 million mammography procedures (Mettler et al. 2008). A national survey in New Zealand reported that 98300 CT scans (excluding extremity procedures) were performed in 2007 (Stirling & Cotterill 2009). From 2007 to 2012, New Zealand's national breast screening programme conducted 1.3 million screening episodes (BreastScreen Aotearoa 2013). It was also estimated that 2.2 million plain radiography procedures were performed in New Zealand in 2010 (Stirling 2013)[1]. In these conventional x-ray images, contrast between materials is determined by their effective x-ray absorption values. As such, certain

---

[1] Scans performed using mobile theatre equipments are excluded in this figure.

materials, such as iodine and calcium, may appear similar in conventional x-ray images.

In his classical paper, Hounsfield (1973) hypothesised that two materials can be identified in a set of dual-energy scans performed separately at two x-ray tube voltages. Previous developments of CT imaging focused on increasing the scanning speed and acquisition of more slices. It is not until recent decades that dual-energy CT (DECT) has been employed in clinical settings (Kalender 2006). The incident source spectra in DECT are produced by mounting two x-ray tubes in the scanner, operating at different energies (Flohr et al. 2006). Alternatives to this dual-source configuration will be discussed later. Although several clinical applications have been pioneered, material analysis in dual-energy imaging is somewhat limited since only two spectra are measured. Furthermore, information is degraded in DECT due to the inherent overlap between the spectra of the high and low energy scans (Johnson et al. 2010).

This thesis focuses on an emerging technique called spectral x-ray imaging. Spectral imaging uses only a single x-ray source, while a photon counting detector (PCD) measures the energy distribution of the x-ray spectrum to provide energy-sensitive images. Prototype spectral CT scanners have been developed for research purposes (Schlomka et al. 2008, Butler et al. 2008). The overall benefits of spectral x-ray imaging include improved diagnosis, in addition to the potential of reducing radiation dose. The advanced photon counting technology can produce higher image quality in spectral CT compared to conventional CT (Tapiovaara & Wagner 1985, Shikhaliev 2008b). Increased contrast agent resolution (Shikhaliev & Fritz 2011) and improved discrimination between materials can also be facilitated, as more data points are acquired compared to dual-energy imaging (Frey et al. 2007, Niederlöhner et al. 2005).

1.1   Aim

The primary aim of this thesis was to study the feasibility of spectral x-ray imaging and to develop theoretical guidelines for scanning parameters in spectral x-ray imaging. By minimising the incident photon flux while maintaining sufficient information richness in an x-ray measurement, materials within an imaging object can be identified with the highest dose efficiency. In spectral x-ray imaging, the amount of information regarding the object contained in a measurement can be further affected by the arrangement of the energy subdivisions within a PCD (Frey et al. 2007, Niederlöhner et al. 2005, Roessl & Proksa 2006). The theoretical framework therefore aims to optimise the partitioning of transmitted spectrum in a PCD and to estimate the optimal incident beam quantity, for the most efficient material discrimination using spectral x-ray imaging. The next aim was to validate the theoretical model by means of Monte Carlo simulations. The final part of the thesis aimed to examine the practical limitations of a PCD, called the Medipix detector (Ballabriga et al. 2011a). An overview of the thesis is given in the next section.

1.2   Outline

In Chapter 2, the fundamental contrast mechanisms in x-ray images are reviewed. An introduction to x-ray interactions with matter is presented and a discussion of the principles of spectral imaging follows. In Chapter 3, a novel model to optimise the collection of energy information for spectral imaging is presented. The optimisation is based on a framework for material thickness estimation assuming an ideal photon counting detector. Chapter 4 introduces a simulation model for validation, based on the BEAMnrc code system. A thickness estimation method is presented and applied to the simulated spectral images. Upon validating the

theoretical model, a comparison between spectral and dual-energy mammography with respect to optimal dose is discussed. The focus is shifted in Chapter 5 to experimental work on actual photon counting measurements. The candidate's contribution to various technical aspects of an in-house developed spectral micro-CT scanning system is discussed. Preliminary measurements using the advanced features of the Medipix detector are presented. The work is then summarised and future directions are discussed in Chapter 6. Finally, an additional project relating to CT reconstruction with synthetically truncated projection data that the candidate worked on is presented in Appendix B. This work was carried out during an internship at the Nova Scotia Cancer Center in Halifax, Canada after the temporary closure of the University of Canterbury due to the Canterbury earthquakes in 2011.

1.3   Academic contributions

During the course of this thesis, the candidate has published one journal article (Nik et al. 2011) and one conference paper (Doesburg et al. 2012). Two journal articles are being prepared for submission (Nik et al. 2013, Walsh et al. 2013). Work from this thesis has contributed to two other publications for which the candidate is a co-author (Ronaldson et al. 2011, Walsh et al. 2011a). The candidate has presented his work at three international conferences and a local meeting, as well as given invited talks on spectral imaging at two international research institutions. Publications and presentations resulting from work in this thesis are listed below in a chronological order, along with their respective descriptions.

PUBLICATIONS

M F Walsh, A M T Opie, J P Ronaldson, R M N Doesburg, **S J Nik**, J L Mohr, R Ballabriga, A P H Butler and P H Butler (2010). First CT using Medipix3 and the MARS-CT-3 spectral scanner. *Journal of Instrumentation* **6** C01095 (Conference Contribution - Full conference paper)

First CT images acquired using the in-house developed CT scanner, named the Medipix All Resolution System (MARS), with a Medipix3 detector were reported. An advanced feature of the Medipix3 detector, called charge summing mode (see section 2.5.1), was demonstrated to be capable of spatially reconstructing alpha particles of multiple incorrect counts into single valid occurrences. The candidate contributed to the equalisation procedure of the detector and the processing of spectral projections. This paper was published in the proceedings of the *12th International Workshop on Radiation Imaging Detectors (iWoRID)*.

J P Ronaldson, M Walsh, **S J Nik**, J Donaldson, R M N Doesburg, D van Leeuwen, R Ballabriga, M N Clyne, A P H Butler and P H Butler (2010). Characterization of Medipix3 with the MARS readout and software. *Journal of Instrumentation* **6** C01056 (Conference Contribution - Full conference paper)

This paper evaluated the electronic stability, image quality and spectroscopic performance of the Medipix3 detector. The conventional single pixel mode of operation was shown to be acceptable for ongoing research. However, imaging performance in the charge summing mode was expectedly limited, with temporal instabilities noted in several detector parameters. The candidate contributed to the equalisation procedure of the detector and the processing of spectral projections. This paper was published in the proceedings of the *12th iWoRID*.

S J Nik, J Meyer, R Watts (2011) Optimisation of material discrimination using spectral x-ray imaging. *Physics in Medicine and Biology* **56** 5969-5983. (Journal Article)

A comprehensive description of the theoretical model, which the candidate has developed, was given in this paper. Novel results on the optimisation of energy parameters for discriminating materials related to small animal and breast imaging were presented. The candidate prepared this article.

R M N Doesburg, T. Koenig, **S J Nik**, S. T. Bell, J P Ronaldson, M F Walsh, A P H Butler and P H Butler (2012). Spectrum measurement using Medipix3 in Charge Summing Mode. *Journal of Instrumentation* **7** C11004 (Conference Contribution - Full conference paper)

This paper presented the measurements of a relatively intense americium gamma source using the charge summing mode. Spectroscopic performance and limitations

of the detector were discussed. The candidate personally prepared the article for publication as part of the proceedings for the *14th iWoRID*.

M F Walsh, **S J Nik**, S Procz, M Pichotkac, R M N Doesburg, N De Ruiter, C J Bateman, A I Chernoglazove, R K Panta, A P H Butler and P H Butler (2013) Spectroscopic CT data acquisition with Medipix3.1 (Journal Article - Preprint)
The novel results of using another advanced feature of the Medipix3.1 detector, known as the spectroscopic mode, to simultaneously obtain images at eight energy ranges will be presented. Data acquisition of a customised phantom and a mouse was performed in collaboration with local and overseas collaborators. The candidate was responsible for enabling and testing the feature in the in-house developed detector readout system, as well as contributed considerably towards preparing the article. This paper has been accepted for publication in *Journal of Instrumentation*.

S J Nik, R S Thing, R Watts, T Dale, B Currie and J Meyer (2013) Optimal material discrimination using spectral x-ray imaging: Monte Carlo validation and application to mammography. (Journal Article - under preparation)
This paper will describe the simulation model presented in this thesis. Results on the validation of the theoretical model and on the optimisation of dose with regard to mammography will be presented. The candidate obtained all of the results and has prepared this paper, which is planned to be submitted to *IEEE Transactions on Medical Imaging*.

Presentations (*presenter)

S J Nik*, J Meyer, A P H Butler, P H Butler, R Watts (2010) Optimisation of energy thresholds in spectral X-ray imaging for biological material discrimination. *Health Research Society of Canterbury (HRSC) Clinical Meeting*, Chirstchurch, New Zealand. In *New Zealand Medical Journal*, 123, 1324. (Oral)
This talk presented the initial developments of the theoretical model.

R S Thing, **S J Nik**, R Watts, T Dale, B Currie and J Meyer* (2010) Simulation of energy selective x-ray images for material discrimination. *New Zealand Physics and Engineering in Medicine conference (NZPEM 2010), Dunedin, New Zealand.* (Oral)
This presentation introduced the development and validation of the Monte Carlo simulation model.

S J Nik*, J Meyer, R Watts (2010) Optimisation of material discrimination using

spectral CT. *Engineering and Physical Sciences in Medicine and the Australian Biomedical Engineering Conference (EPSM ABEC 2010)*, Melbourne, Australia. (Oral)
Preliminarily results of the theoretical model were presented in this talk.

R S Thing, **S J Nik***, T Dale, B Currie, R Watts and J Meyer (2010) A virtual spectral CT scanner. *Engineering and Physical Sciences in Medicine and the Australian Biomedical Engineering Conference (EPSM ABEC 2010)*, Melbourne, Australia. (Oral)
This presentation introduced the development and validation of the simulation model. The candidate presented the talk on behalf of R S Thing.

R Doesburg, T Koenig, **S J Nik***, S Bell, J P Ronaldson, M Walsh, A P H Butler, P H Butler, R Watts (2012) Spectrum measurement using Medipix3 in Charge Summing Mode *14th iWoRID*, Figueira da Foz, Portugal. (Oral)
Results of the charge summing mode measurements were presented and limitations of the Medipix3 detector were discussed. This presentation corresponds to the publication Doesburg et al. (2012) in *Journal of Instrumentation*.

S J Nik*, R S Thing, R Watts, J Meyer (2012) Material quantification in spectral x-ray imaging: optimization and validation. *54th Annual American Association of Physicists in Medicine (AAPM) Meeting* in Charlotte NC, USA. (Oral)
This talk summarised the simulation model and presented results on the validation of the theoretical model using simulation.

S J Nik* An overview of the Medipix detector. *Biomedical Imaging Division, School of Biomedical Engineering & Sciences*, Virginia Tech - Wake Forest University in Blacksburg, USA. (Oral)
This invited presentation at Virginia Tech explained the technical details and operations of the Medipix detector to a collaborator with a MARS-CT scanner.

S J Nik* Spectral x-ray CT using energy-resolving photon counting detector. *Environmental Science & Research* in Christchurch, NZ. (Oral)
This invited talk introduced the operation of the MARS-CT scanner. A summary of the applications of the imaging system was presented.

Chapter 2

Background

The behaviour of x-rays after passing through matter is dependent on the attenuation properties of its materials. *Attenuation* according to Bushberg et al. (2003) is 'the removal of photons from a beam of x- or gamma rays as it passes through matter'. Materials with higher densities and higher atomic numbers attenuate more. Just like when Roentgen imaged his wife's hand, the bones of her hand and her wedding ring cast a darker shadow on the photographic plate than the penumbra of her soft tissue, resulting as white structure on the developed film. Attenuation is also a function of the x-ray energy. X-rays of lower energy, or soft x-rays, are more likely to be attenuated by matter. Harder x-rays are less likely to be attenuated. The variable transparency of matter to x-ray forms the fundamental contrast in x-ray imaging.

In this chapter, the basics of x-ray and CT imaging, the physics of x-ray attenuation and some current imaging techniques are discussed. An emerging x-ray detection modality called the photon counting detector and its potential and prospective implementations will be introduced.

2.1 X-ray and CT imaging

A projection measurement is an image of x-ray transmission through an object, as measured by an x-ray detector. Applications of x-ray projection imaging range from the visualisation of bony structures such as in chest radiography, or in dental radiography, to the visualisation of soft tissue in mammography. Unlike in an x-ray radiograph, overlapping structures are not superimposed in CT images. An x-ray CT scanner is designed to reconstruct the internal structure of an object, after taking projection measurements from multiple directions. While this research focuses on the fundamental physics of projection images, this is the basis for CT imaging and thus, the ideas presented in this thesis are expandable to CT. The image acquisition and reconstruction chain in x-ray CT imaging is therefore briefly reviewed.

2.1.1 An overview of CT imaging

X-ray CT is generally thought to have been co-invented by Godfrey N Hounsfield (Hounsfield 1973) and Allan M Cormack (Cormack 1963). Standard clinical CT features an x-ray tube and a detector array rotating around the patient. The x-ray beam is collimated to give a fan-beam, illuminating a thin cross-sectional slice of the imaging object. For each slice, the attenuation value of an imaging object is calculated at every two-dimensional position (x, y). For a ray that casts through the object, the transmitted number of photons along the x-ray path r is

$$N = N_0 \mathrm{e}^{-\int \mu(r)dr}, \tag{2.1}$$

where $\int \mu(r)dr$ defines the line integral of the attenuation along the ray measured on a projection. This line integral sums up the attenuation distribution, $\mu(x, y)$, of the overlapping structures along the ray path, r.

The first and second generations of CT scanners required the translation of a narrower x-ray beam and a detector, which has become obsolete. Rather, in the long-lasting third generation geometry, the detector arc and the x-ray source subtends an angle adequately covering the size of the patient (Bushberg et al. 2003). The transient fourth generation uses a fan-beam, with the detectors arranged in a fixed ring around the gantry. After a full rotation of the CT gantry, the cross-sectional map of $\mu(x, y)$ can be reconstructed following a series of corrections for the reduction of image artifacts. The most widely implemented reconstruction algorithm is known as the filtered backprojection (FBP) (Slaney & Kak 2001), while other analytical and iterative reconstruction methods remain a highly active area of research.

2.2 X-ray contrast

In the diagnostic energy range of $10\,\mathrm{keV}$ to $150\,\mathrm{keV}$, the possible types of photon interaction with matter are Rayleigh scattering, Compton scattering and the photoelectric effect. During a photoelectric interaction, the incident photon disappears (is absorbed) after transferring all its energy to an electron, causing it to be ejected from the atom. In both Compton and Rayleigh scattering events, the interacting photon changes direction of travel without being absorbed. In Rayleigh scattering, the interaction occurs with the entire atom, as opposed to a single electron in a Compton scattering event.

All these interactions result in the removal of the x-ray from its original path, either by being scattered or by being absorbed and all interactions contribute to the attenuation. The linear attenuation coefficient μ, describes the total attenuation of a material as a result of Rayleigh scattering, Compton scattering and

the photoelectric effect, where at an energy E,

$$\mu(E) = \mu_R(E) + \mu_C(E) + \mu_P(E). \tag{2.2}$$

Subscripts R, C and P denote Rayleigh, Compton and photoelectric components, respectively. The contribution due to Rayleigh scattering can be as low as 5% above 70 keV in soft tissue (Bushberg et al. 2003) and is often ignored. The μ_C and μ_P components can be approximated by:

$$\begin{aligned}
\mu_C(E) &= \rho_e f_{KN}(E) \\
\mu_P(E) &= \rho_e C_P \frac{Z^m}{E^n}.
\end{aligned} \tag{2.3}$$

Z is the atomic number of the element while ρ_e is the electron density of the atom in electrons/cm^3 (McCullough 1975). The exponents in the photoelectric components has been determined experimentally to be $m = 3.8$ and $n = 3.2$ (Macovski 1983). The constants C_P is 9.8×10^{-24} (McCullough 1975). The Klein-Nishina formula ($f_{KN}(E)$) describes the energy dependency of the Compton scattering and can be written as (Macovski 1983)

$$f_{KN}(E) = \frac{1+\alpha}{\alpha}\left[\frac{2(1+\alpha)}{(1+2\alpha)} - \frac{1}{\alpha}ln(1+2\alpha)\right] + \frac{1}{2\alpha} - \frac{1+3\alpha^2}{1+2\alpha}, \tag{2.4}$$

with $\alpha = $ E/E$_e$. Here E$_e \approx 511$ keV denotes the rest mass energy of an electron. The photoelectric absorption effect may feature an abrupt discontinuity in the attenuation, known as the absorption edge within or outside the diagnostic energy range. For now, lets consider only the description of the photoelectric effect with no absorption edges. The effect of absorption edges will be addressed in section 2.4.

Briefly speaking, the total attenuation depends on the energy of the incoming

photon (E), the atomic number (Z) and the electron density (ρ_e) of the absorbing material. As described in (2.3), the Compton scattering and photoelectric absorption probabilities decrease with energy at different rates, which is depicted in figure 2.1. The photoelectric absorption, which is more dominant at lower energies, falls off rapidly as E increases. Compton scattering decreases comparatively slower and is the more dominant contribution to the total attenuation at higher energies. For calcium, as an example, the crossover of these two attenuation components occurs at approximately 85 keV (see figure 2.1). Additionally, μ_P has a stronger dependency on the atomic number, while μ_C is directly proportional to ρ_e.
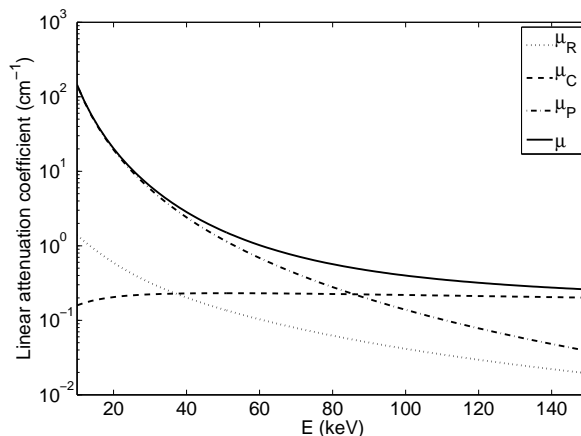
Figure 2.1: *The contributions of the Rayleigh scattering, Compton scattering and photoelectric absorption, together with the total linear attenuation, are plotted for calcium to show the different falloff rates of the attenuation components.*

Disregarding the effect of Rayleigh scattering, the linear attenuation μ of a material in (2.2) can be described as a linear combination of the Compton and the photoelectric basis functions. $f_{KN}(E)$ and $1/(E^{3.2})$ are the attenuation basis functions. Given two linearly independent acquisitions, the coefficients of the basis functions can be estimated to reconstruct the attenuation basis images (Alvarez & Macovski 1976). The Compton and the photoelectric basis images,

respectively, represent the electron density and the atomic number, which are useful depictions of an object's constituents. Materials with lower atomic number mainly correspond to the Compton basis and the high-Z materials to the photoelectric component. When the composite materials of a measured object are discriminated in this manner, we say that they are *decomposed*. Material decomposition, in the absence of K-edge (see section 2.4), can be regarded as solving a system of two linear equations for two variables. In this context, the two unknowns can be determined provided there are at least two spectrally distinct measurements. The specifics of decomposition techniques will be outlined in section 2.6.

The effective Z is a measure of the average atomic number for a compound and a mixture of materials. Bone, due to the presence of calcium ($Z = 20$), has a considerably higher effective Z of about 13, compared to soft tissue, which is mostly made up of lower Z materials such as hydrogen, carbon, nitrogen and oxygen. Soft tissue has an effective atomic number of about 7.6 (Bushberg et al. 2003) and is regarded to be similar to that of water. The decomposed photoelectric and Compton basis images would thus reveal bone and soft tissue, respectively. Moreover, bone can be written as a mixture of 0.832 portion of lucite and 0.237 portion of aluminium (Lehmann et al. 1981). In fact, any material can be rewritten as a combination of two other materials, since the latter two materials are themselves a linear combination of the two attenuation basis functions. The measurements of bone and soft tissue in the above example can be decomposed equally well into two material basis functions, rather than the Compton and the photoelectric basis functions. If the attenuation spectra of calcium and water were chosen for the decomposition, the locations of bone and soft tissue would appear on the calcium and water basis images, respectively.

2.3   Dual-energy x-ray and CT imaging

In dual-energy CT, the spectra required for the decomposition must be sufficiently distinct for a useful material decomposition. A straightforward method is to sequentially acquire images of two different incident energy spectra by means of two separate rotations of the CT gantry. A second set of projections can be captured upon switching the x-ray source voltage. The low and high energy scans are unlikely to be perfectly registered due to e.g. patient and/or organ movements during the delay between the two acquisitions. Another disadvantage is that the time it takes may be suboptimal with respect to undesired distribution of contrast agents (Johnson et al. 2010). An ideal setup, which is technically not yet feasible is to simultaneously emit two monochromatic x-ray beams at optimally selected energies.

Dual-source (Flohr et al. 2006, Johnson et al. 2007) or rapid voltage switching (Kalender et al. 1986, Grasruck et al. 2009) techniques can be regarded as a surrogate, whereby two polychromatic beams are emitted. The 80 kVp and 140 kVp tube spectra, with average energies of 53 keV and 71 keV, respectively, are considered sufficiently distinct in clinical practice (Johnson et al. 2010). In a dual-source configuration, each of the two sources is coupled with a detector, with the source-detector pairs sustain an offset of 90 degrees (figure 2.2) and a complete dual-energy scan can be acquired with a single gantry rotation. Because they are operated independently, the filtrations and currents of the x-ray tubes can be individually optimised for increased beam separation. However, there can be an increase in hardware complexity and in cost due to the additional source and detector pair (Johnson et al. 2010), which also limits the size of the field-of-view in the restricted space in a CT gantry.

The rapid voltage switching approach requires less hardware modifications, by utilising only a single source with the ability to swiftly alternate between the
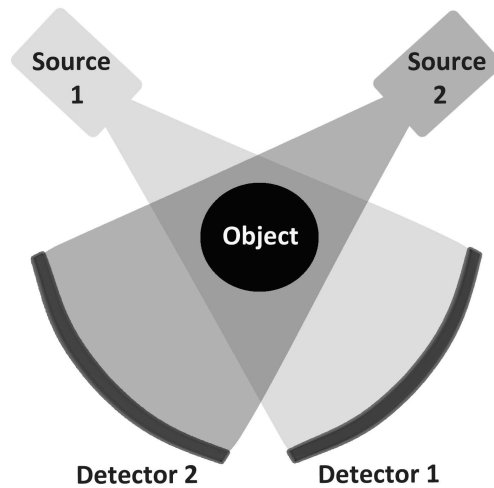
Figure 2.2: *The dual-source configuration. Two source and detector pairs arranged at 90 degrees simultaneously produce projections at two tube voltages as the gantry rotates around the patient.*

low and high tube voltages (figure 2.3). As the single source-detector pair rotates around the patient, dual-energy projections are collected sequentially with minimal misregistrations. Compared to the dual-source DECT, the overall acquisition has to be slower to accommodate for the additional projection measurements. The switching between kVps is also not instantaneous. The voltage does not fully follow a pulsed curve, which reduces spectral separation (Johnson et al. 2010).

By placing a layered detector, two measurements can be acquired at low and high energies with a single x-ray source. The first layer of the detector preferentially absorbs low energy photons and exhibits weaker attenuations at the higher energies (figure 2.4). A different scintillator with stronger sensitivity for the higher energy range targets the remaining photons that penetrated the first layer. This technique therefore allows for simultaneous, rather than sequential, dual-energy acquisition and is ideal for e.g. cardiac imaging. The spectral difference obtainable using a layered detector, however, remains the lowest among the
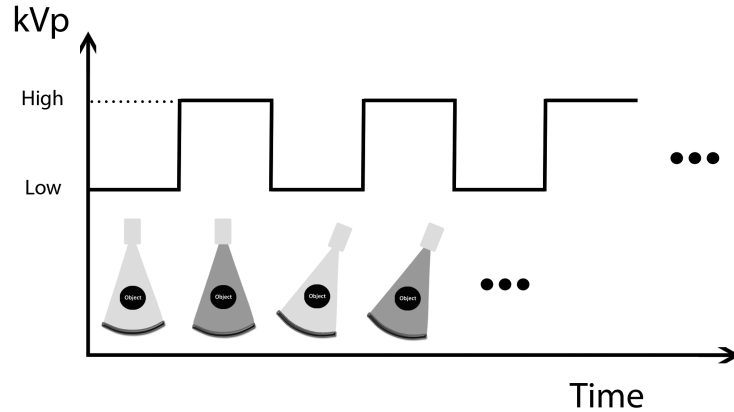
Figure 2.3: *The rapid voltage switching mode of DECT acquisition. The x-ray tube is capable of switching for one tube voltage to another within a very short time. The overlapping projections are measured separately by a single detector to assemble a dual-energy dataset.*

three DECT modes (Johnson et al. 2010).

Dual-energy x-ray imaging thrives on the energy dependency of the Compton and photoelectric interaction mechanisms to provide a decomposition of materials. Most of the clinical applications has been identified as the depiction of heavier elements, particularly calcium and iodine ($Z = 53$). These heavier elements increase the localised attenuation primarily because of their higher atomic numbers Z. When used in projection imaging, the lower or the higher energy image can be suitably weighted to remove (or subtract) the contrast from soft-tissue or bony structure. In chest radiography, for example, dual-energy subtraction is applied to emphasize the subtle pulmonary abnormalities on the water-weighted image, while contrast from the ribs exists only in the bone-weighted image (Bushberg et al. 2003). Similar subtraction of low and high energy scans is applied in CT angiography (Johnson et al. 2010). Vasculature can be highlighted in an angiogram by removing the bony structure in order to examine vascular conditions such as aortic aneurysm or pulmonary embolism. Previously impossible iodine
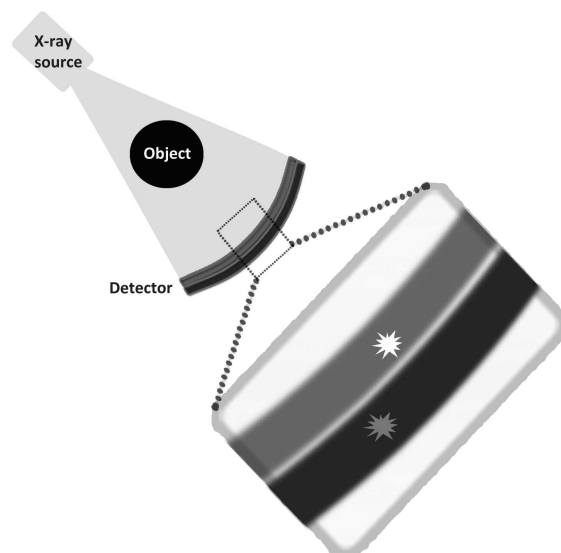
Figure 2.4: *The dual-layer detector configuration. The two detector materials demonstrate different preferential absorbances. Lower and higher effective spectra are captured respectively by the top and bottom layers, while the x-ray source is operated at a kVp settings.*

and calcium separation has therefore been pioneered in DECT, along with the quantification of calcification, depictions of collagen and characterization of other tissues (Flohr et al. 2006, Johnson et al. 2007, Graser et al. 2009).

2.3.1 Energy integrating detectors

The detectors employed in the current clinical CT and radiographic systems use a scintillating material to convert x-ray photons into visible light. The light photons are then converted into electric signal that are proportional to the x-ray energies by a photodiode. These detectors are known as *energy integrating detectors* because they measure the total amount of energy deposited during an exposure. The distribution of photon energies and the number of events are not recorded. Using the same notations as (2.1), the detected signal, *ds*, of an energy

integrating detector can be formulated as

$$ds = \int E N_0(E) \mathrm{e}^{-\int \mu(r)dr} dE. \tag{2.5}$$

Due to the integration over the energy spectrum, only an average attenuation of the imaging object can be measured. An energy integrating detector cannot take advantage of the polyenergetic spectrum, which contains much information about photon energies. The energy weighting in (2.5) further reduces information contained in the measurements since attenuation contrast between different materials is greater at higher energies than at lower energies. A means to recover the energy information lost in the energy integrating detectors will be presented in section 2.5.

2.4 K-edge imaging

Besides simply increasing the local attenuation, iodine features a sharp discontinuity in its attenuation curve, caused by the binding energy of the innermost (K) shell electrons. Only photons with energies higher than the binding energy have the possibility to knock out the K-shell electrons. Accordingly, photons with energies just above the K-shell binding energy of iodine are attenuated more strongly than those just below. The sudden increase in the photoelectric absorption probability is manifested in the attenuation at the particular *K-edge energy*. The mass attenuation coefficient, which is the ratio of linear attenuation to mass density, is plotted to show the K-edges of several high-Z materials in figure 2.5. The K-edge of iodine is located at 33.2 keV. This K-edge discontinuity is unique for each element and cannot be modelled by the continuous Klein-Nishina and $1/(E^{3.2})$ curves. A new basis function representing the material with a K-edge has to be introduced.

In order to utilise the K-edge discontinuity in material decomposition, how-ever, it is important that there are sufficient transmitted photons below the K-edge energy level. Calcium, for instance, has a K-edge energy of 4 keV, which is too low to be considered within the diagnostic energy. Likewise, photons with energies below the K-edge of iodine do not penetrate greatly through an object of interest in diagnostic imaging. As pointed out in section 2.3, the mean en-ergy of an 80 kVp tube is 53 keV. The vast majority of the transmitted photons have energies greater than the K-edge of iodine since their average energy is well above 33 keV. Gadolinium ($Z = 64$), on the other hand, has a K-edge located at 50.2 keV. While iodine is omnipresent in conventional CT imaging, gadolinium is therefore seen as a more promising candidate in the context of K-edge imaging (Roessl & Proksa 2007). Gold has an atomic number of 79 (K-edge energy = 80.7 keV) and is emerging as another potential x-ray contrast agent.
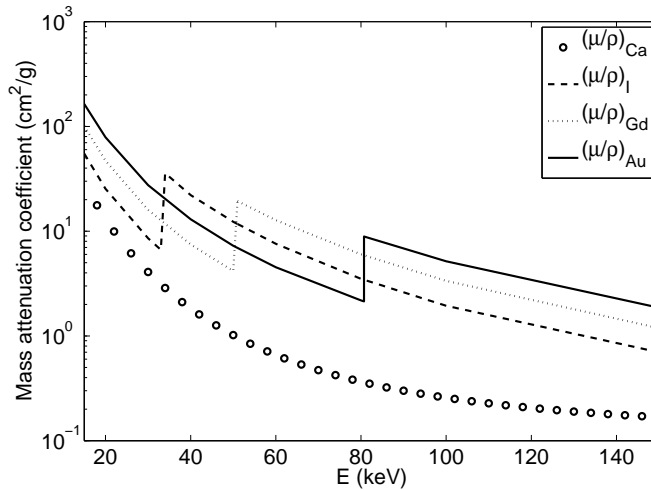
Figure 2.5: *K-edges as a result of K-shell binding energies are prominent for iodine (at 33.2 keV), gadolinium (50.2 keV) and gold (80.7 keV). K-edge energy increases according to the atomic number. Calcium's K-edge (4 keV) is considered too low for diagnostic x-ray imaging. Mass attenuation value (μ/ρ) is obtained from Berger et al. (2005) and is plotted in place of μ to neglect the factor of material density (ρ).*

With the existence of a K-edge, three basis functions representing the linear

attenuation curves of three materials (two without K-edge, one with K-edge) that are not linearly dependent on each other can be formed. To be specific, iodine, soft tissue and calcium can be represented by either the linear combination of the Klein-Nishina and $1/(E^{3.2})$ (equation (2.3)) plus the attenuation of iodine (the K-edge material), or equally well by the three individual material attenuation functions. The objective of K-edge imaging can hereby be simplified as: acquire three measurements in order to solve for three unknowns, namely the amount of the three materials. The potential of this three-dimensional imaging technique has been identified earlier by including an additional measurement to the two provided by DECT. A straightforward approach is to apply a set of three appropriately selected monoenergetic beams (Sukovle & Clinthorne 1999). When three polychromatic x-ray spectra were used, Riederer & Mistretta (1977) favoured strongly filtering two beams to have mean energies straddling the iodine's K-edge, with the third beam at a higher energy.

2.5   Spectral x-ray and CT imaging

A different way of obtaining energy-sensitive x-ray images is by recording the energy of the detected photons in addition to their spatial positions. CT systems for the acquisition of energy resolved images, often referred to as 'spectral CT', have been demonstrated to be feasible (Delpierre et al. 2002, Schlomka et al. 2008, Shikhaliev 2008b, Butler et al. 2008). Several families of PCDs with energy-resolving capabilities, such as the Medipix (Llopart et al. 2002, Ballabriga et al. 2011a), Pilatus (Broennimann et al. 2006) and XPAD (Delpierre et al. 2002, Pangaud et al. 2007) detectors have been built to achieve this. While spectral CT may sometimes refer to the implementation of DECT as described in section 2.3 (e.g. in Heismann et al. (2012)), 'spectral x-ray imaging' and 'spectral CT' are

used in this work strictly to refer to the acquisition with an energy-sensitive PCD with a single x-ray source/voltage. Elsewhere, this imaging technique has also been referred to as spectroscopic, multi-energy, colour, photon counting or spectral CT.
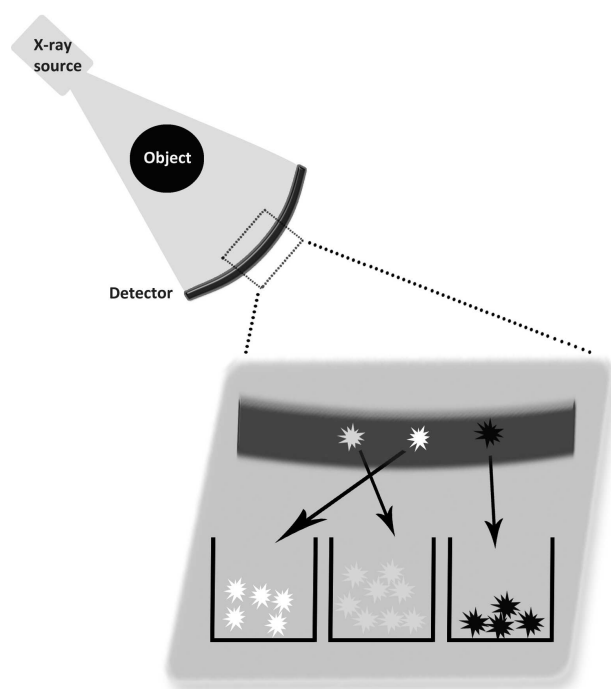
Figure 2.6: *Illustration of photon binning in a PCD. When detected, photons within a particular energy range are grouped together. PCDs have the ability to dissect the transmitted spectrum into multiple narrower ranges. Three energy bins are shown for illustration purposes.*

PCDs use a semiconductor sensor layer to directly convert x-ray photons into an electrical signal. When the semiconductor material is ionised, an electron-hole pair is generated and a pulse with an amplitude relative to the photon energy is induced in that pixel. Conventional x-ray detectors measure the total deposited energy of all detected photons. In a PCD, the pulse created by a photon detection event is individually counted and analysed (see e.g. Llopart et al. (2002),Pangaud

et al. (2007)). The energy-resolving capability of PCDs is achieved with pulse height discriminators within the readout Application Specific Integrated Circuit (ASIC). Each pixel in a PCD is connected to a tunable pulse height discriminator to compare the charge created with preset levels and therefore can be considered an individual spectrometer. If the preset threshold is exceeded, the associated counter is incremented to record the number of photons with energies higher than that level.

Photon counts associated with a higher energy level can be subtracted from that of a lower energy to form data for an *energy bin* (figure 2.6). Additional discriminators are provided in some detectors, e.g. the Medipix2 and the XPAD3C detectors, as energy high threshold, such that a single energy bin can be formed throughout acquisition (Llopart et al. 2002, Pangaud et al. 2007). Only photons with energies within this window are counted. PCDs are in theory capable of measuring over an arbitrary number of energy ranges, rather than the two spectra measured in DECT. As many as 8 independent discriminators are provided in the Medipix 3 detectors (Ballabriga et al. 2011a). The decomposition into as many materials as the number of discriminators is theoretically feasible, provided that there are suitable contrast agents with K-edge energies sufficiently far apart for effective K-edge imaging. Note that simultaneous detection of too many contrast agents may be superfluous to clinical necessity.

One immediate advantage of imaging in multiple narrower energy ranges is the reduction of beam hardening. When the softer x-rays are preferentially filtered, a beam is said to be 'hardened'. As energy integrating detectors intrinsically apply much lighter weights on the low energy photons, a distortion of the transmitted spectrum can be observed (Shikhaliev 2005). Beam hardening results in an overestimation of the regional attenuation values. PCDs weight each photon equally and thus reduce beam hardening distortions. Furthermore, Giersch et al.

(2004) simulated photon counting and energy integrating images of soft tissues to show that the former can provide a higher image signal-to-noise ratio (SNR) when compared to the latter. The image quality can be further enhanced, by virtue of weighting photons according to their energies, although at the expense of increased beam hardening artefact (Shikhaliev 2005). Finally, by focusing on the energies at which the materials differ at most in terms of x-ray attenuation, energy-sensitive x-ray imaging can improve subtle tissue contrast, which may help diagnoses of diseases such as breast cancer (Bones et al. 2010).

2.5.1 Medipix detectors

One example of the PCDs is the Medipix detector family. Designed and built by an international collaboration based at the European Organization for Nuclear Research (CERN) [1], the Medipix detector was initially developed for high energy physics and has been proposed for use in medical imaging. The first version of the Medipix detector, the Medipix1 consisted of 64×64 pixels each of the size of $170 \times 170\,\mu m^2$ and served as a proof of concept (Campbell et al. 1998). The spatial resolution was improved to $55 \times 55\,\mu m^2$ in the Medipix2 (Llopart et al. 2002). In addition, the input polarity of the ASIC can be switched between positive and negative in order to collect both electrons and holes (Pfeiffer 2004), which allowed the use of alternative sensor layers. For example, cadmium-telluride has a comparatively higher absorption coefficient but generates the opposite type of charge carrier than silicon. The chip can also be connected on three of its sides, allowing the assembly of larger detectors.

The current state of development is Medipix3. Compared to its predecessors, one advantage of the Medipix3 is the capability to distinguish eight bins simultaneously, however, at cost of the spatial resolution. The conventional Single Pixel

---

[1] http://medipix.web.cern.ch/MEDIPIX/

Mode (SPM) operates with up to two energies per pixel at a pixel pitch of 55 µm and is available in both Medipix2 and 3. Mapping four readout ASIC pixels to a single semiconductor unit of $110\,\mu m^2$ enables the 'spectroscopic mode' of photon detection in Medipix3 (Ballabriga et al. 2011a).

Furthermore, the spectral distortion as a result of the charge sharing effect can be mitigated using the Medipix3 detectors. Due to the spreading of a charge cloud into adjacent pixels, the SPM often suffers from count-loss or multiple invalid counts of lower energies. As illustrated by the circles in figure 2.7a, some of the 10 keV monoenergetic photons were registered as apparent photons of lower energies. When operated in Charge Summing Mode (CSM), the Medipix3 has the ability to communicate among 2×2 neighbouring pixels in order to reconstruct the incoming charge pulses as they appear following a photon detection event. The arbitration circuit then allocates the total charge that is higher then the pre-set threshold to the pixel with the largest contribution (Ballabriga et al. 2011a), based on the 'winner takes all' scheme in figure 2.7b. A Gaussian shaped 10 keV monoenergetic (triangles in figure 2.7a) can be preserved in the CSM, thus improving the energy resolution of the detector.

2.5.2 Other photon counting detectors

Numerous PCDs have been developed in parallel with the Medipix over the past decade or so. Table 2.5.2 gives a brief overview of the available PCDs. A thorough review is beyond the scope of this thesis but basic information and corresponding references detailing the specific technicalities of each detector are provided.

(a)   (b)
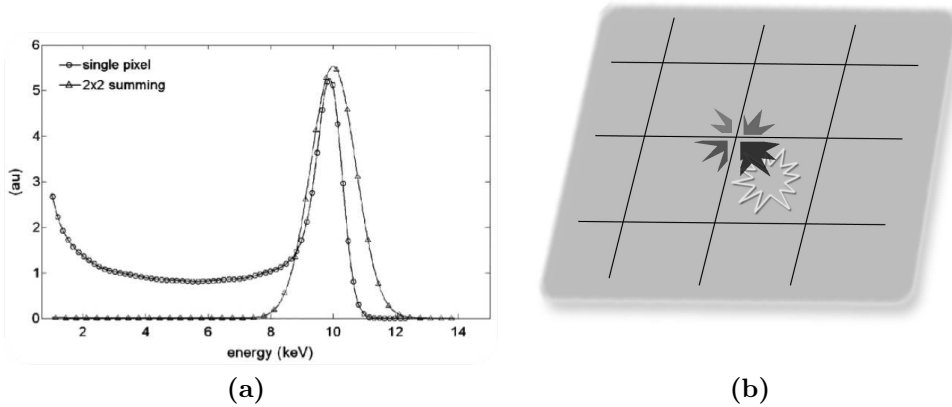
Figure 2.7: *(a) Charge sharing occurs in SPM when the induced charge is spread unevenly among abutting pixels. Each pixel is mistakenly assigned with a signal of a lower energy, causing the 10 keV monoenergetic spectrum to be distorted, as indicated by the circles (Ballabriga 2009). (b) Given the distributed signal, communication among the 2×2 neighbouring pixels in the CSM can reconstruct the original amplitude of the photon energy. The 'winner takes all' scheme in the Medipix3 then allocates the corresponding count to the member with the maximum contribution (bottom right pixel in this illustration). The charge sharing tail thus disappears (triangles) in the CSM 10 keV monoenergetic spectrum in (a).*

2.6 Material decomposition

The Medipix detectors, as well as other PCDs, have been employed for the implementation of K-edge imaging, in which the decomposition of materials has been performed on the image or projection space (Giersch et al. 2005, Schlomka et al. 2008, Firsching et al. 2009, Le & Molloi 2011). In *image-based decomposition*, phantoms containing known materials was first measured and reconstructed at different energies. The CT numbers of the energy-sensitive images can be used to calibrate pixel values to the known material constituent (see e.g. Le & Molloi (2010) and Ronaldson et al. (2012)). The least squares method, for example, then matched the spectral calibration against measured pixel value of the reconstructed images. This image-based approach is thought to be computationally less intensive but can be susceptible to the beam-hardening distortions in the

Table 2.1: Photon counting detectors with energy-resolving capabilities used in x-ray imaging.

Detector	Developer	Pixels matrix	Pixel size (µm^2)
ChromAIX [a]	Aeroflex	4×16	300×300
DIXI[b]	Uni. Uppsala	31×32	270×270
Medipix[c]	CERN[d]	256×256	55×55
MPEC[e] (later CIX[f])	Uni. Bonn	32×32	200×200
Pilatus[g]	PSI[h]	487×195	172×172
XPAD[i]	ESRF[j]	80×120	130×130

[a] Steadman et al. (2011)
[b] Edling et al. (2004)
[c] Pangaud et al. (2007)
[d] European Organization for Nuclear Research
[e] Lindner et al. (2001)
[f] Krüger et al. (2008)
[g] Bech et al. (2008)
[h] Paul Scherrer Institute
[i] Pangaud et al. (2007)
[j] European Synchrotron Radiation Facility

reconstructed pixel values (Frey et al. 2007).

Given the photon counts acquired by a PCD detector at multiple energies, the least squares method can be applied in the *projection-based decomposition* to estimate a sinogram of material composition that is most likely to have produced the spectral projection measurements (Frey et al. 2007). Similarly, the decomposition can be formed as an optimisation problem using the maximum likelihood estimator (MLE) (Roessl & Proksa 2007), which has been experimentally implemented by Schlomka et al. (2008). Another projection-based decomposition method involves fitting a polynomial function to calibration data (Alvarez 2011). Determining the fitting coefficients maps the spectral line integrals to material thicknesses. Given the resultant sinograms, basis images can be reconstructed, although a thorough knowledge of the detector-specific spectral response is required in this projection-based approach (Firsching et al. 2009, Frey et al. 2007).

The objective of either projection or image based decomposition is to produce

basis images with optimum SNR (Tapiovaara & Wagner 1985, Roessl & Proksa 2007). The SNR is a common measure of the image noise. It is intuitive that noise in the measurement propagates through to the decomposition and we have seen that the material attenuations are energy-dependent. For an ideal detector and some monoenergetic beams, the decomposition accuracy is dependent on the x-ray energies as well as the beam quantities. Higher photon counts leads to higher SNR in the measurements. This results in improved decomposition and thus lower basis image noise. While it is possible to 'tweak' a polychromatic x-ray beam (e.g. using filtration), it is more convenient in a PCD to select the energy level of the discriminator. Two key parameters therefore determine the detected counts in a PCD: the incident photon flux rate and the discriminator level. The energy bins must be carefully chosen to minimise the decomposition noise. The radiation dose has to be As Low As Reasonably Achievable (Slovis 2003). A previous work applied the statistical detection theory (Alvarez 2010), whereby the detector performance for differentiating a feature from a background material was examined. However, as Firsching et al. (2006) pointed out, determining the effective values of attenuation functions across the spectrum (matrix M in Alvarez's (2010) paper) requires the input of material quantity.

The next chapter presents a novel theory for optimising noise in the material basis images via the selection of binning energies. The amount of photons required to achieve a given imaging task is estimated. The proposed theory does not assume the prior knowledge of material quantity and is based on a projection based decomposition method, which is achieved by minimising the z-score between a measurement and an expected count.

2.7   Concluding remarks

CT scanners are capable of taking multiple projections to reconstruct a thin cross-section through the imaging object. Contrast in an x-ray image is provided by the varying attenuations of materials. The main modes of photon interaction in the diagnostic energy range are Compton scattering and the photoelectric effect. They have contrasting dependency on photon energy and on material properties. Two attenuation basis functions have been identified as fitting functions to the energy-dependent curves, allowing for decomposition of measurements into two attenuation basis images. Low- and high-Z materials are often depicted in separate images. Material attenuation spectra can be substituted for the Klein-Nishina and the photoelectric basis functions. The resulting decomposed images are consequently material-specific. The dual-energy spectra can be acquired by means of installing two sources of low and high tube voltages, rapidly alternating the kVp of an x-ray tube or employing a detector with layered scintillators of varying absorbances.

Materials of interest to diagnostic imaging may or may not consist of a K-shell photoelectric absorption edge within the energy range considered. K-edge energy increases with atomic number and is thus distinct to each material. When featured, K-edge imaging introduces a new dimension to material decomposition. Decomposition of a material with K-edge from the two material/attenuation bases requires an additional spectrum to be measured. Spectral x-ray using energy-resolving PCDs can be thought of as an expansion of dual-energy x-ray imaging. PCD has the advantage of increased signal-to-noise ratio, among others. More excitingly, in K-edge imaging, spectral x-ray imaging has the ability of simultaneous identification of more materials. Each pixel in a PCD may operate with at least two discriminators to determine if the photon energy exceeds the pre-defined thresholds, and whether to allocate the count in the low or high energy

29

bin. Some PCDs incorporate more than two discriminators per pixel to acquire multi-energy images. CT values or pixelated line integrals measured by a PCD can be decomposed into a linear combination of three basis functions, provided a K-edge discontinuity is captured in one of the energy bins. Energy bins have to be wisely arranged to minimise noise propagation from the measurements to the decomposition. To achieve this, a method to optimise the binning strategy by minimising the decomposition noise is presented in the next chapter.

Chapter 3

Optimisation of material discrimination in spectral x-ray imaging

Based upon Alvarez & Macovski's (1976) technique of dual-energy imaging, the advent of spectral x-ray imaging has enabled three-component decomposition. Given the projection data, material decomposition can be realised by estimating the thicknesses of the materials prior to reconstruction. Higher numbers of energy bins have been demonstrated to be beneficial in material quantification (Frey et al. 2007). For a limited number of bins, the optimal arrangement of energy windows that maximises the spectral information for material separation remains unclear. Tapiovaara & Wagner (1985) provided an optimisation based on the difference in transmittance between two objects. By formulating a likelihood ratio of two hypotheses, Alvarez (2010) computed the optimal detector performance for recognizing the presence of a feature within a background material. The suitability of energy thresholds for material decomposition has been investigated by evaluating the Cramér-Rao lower bound (CRLB) (Roessl

& Herrmann 2009, Wang & Pelc 2011). The CRLB is given by the inverse of the Fisher information matrix and indicates the minimum attainable noise of an estimator, e.g the maximum likelihood estimator.

This chapter proposes a different metric to compute energy bins with optimal spectral information for material separation. Our approach maps the statistical confidence region in the thickness space under the influence of Poisson counting noise. Uncertainty of the thickness estimation is given by the quantitative bounds of the confidence region. Minimizing the thickness uncertainties leads to the optimisation of energy bins, without requiring the CRLB and the considerable manipulation of the Fisher information matrix. As mentioned in section 2.6, the determination of the effective attenuation basis functions can be avoided, too. This leads us to a method to optimise energy bins and counts required per pixel in spectral x-ray imaging. The framework is applied to discriminate materials of interest to small animal and breast imaging.

Material of this chapter has been published in *Physics in Medicine and Biology* (Nik et al. 2011).

3.1   Methods

Suppose an object along an x-ray path consists of m known materials. The number of transmitted photons, N as governed by the Beer-Lambert equation is:

$$N(E, \boldsymbol{t}) = N_0(E)\mathrm{e}^{-\sum_{i=1}^{m} \mu_i(E)t_i}, \tag{3.1}$$

where N_0 is the number of incident photons, E denotes energy and the vector $\boldsymbol{t}$ represents the thicknesses of the m materials t_i with $i = 1, \ldots, m$. The linear attenuation coefficients μ_i, again, describe the total attenuation of material i. The advent of PCDs with energy-resolving capabilities allows N, the number of

detected photons between energies E_l and E_h, to be registered, where

$$N(E_l, E_h, \boldsymbol{t}) = \int_{E_l}^{E_h} N_0(E) \mathrm{e}^{-\sum_{i=1}^{m} -\mu_i(E)t_i} \, dE. \tag{3.2}$$

Models for calculating incident photon fluence, $N_0(E)$, are well established (Tucker, Barnes & Chakraborty 1991, Tucker, Barnes & Wu 1991). Given the number of detected photons, there exists a $\boldsymbol{t}$ such that the equality in (3.2) is true. The implementation of an iterative algorithm (Lagarias et al. 1998) to compute $\boldsymbol{t}$ will be presented in section 4.1.3. At least as many bins, n, as materials, m, have to be fitted ($n \geq m$) for the discrimination of m materials. Henceforth, it is assumed that photons are binned into a minimum of $n = 2$ energy bins, for the separation of at least $m = 2$ materials. Photons with energies between and inclusive of $E_{(l,k)}$ and $E_{(h,k)}$ are allocated into energy bin k for $k = 1, \ldots, n$, where $E_{(l,k)}$ and $E_{(h,k)}$ are the low and high limits for bin k, respectively. The photon count in bin k is denoted N_k.

3.1.1 Optimisation metric

In photon counting statistics, N_k follows a Poisson distribution with a mean of λ_k; the standard deviation is $\sigma_k = \sqrt{\lambda_k}$. For any set of thicknesses $\boldsymbol{t}$, the mean vector, $\boldsymbol{\lambda} = \{\lambda_k\}$ for the $k = 1, \ldots, n$ distributions can be computed using (3.2). Given a measurement $\boldsymbol{x} = \{x_k\}, k = 1, \ldots, n$, a null hypothesis H_0 is established, such that there is no difference between the measurement and the expected counts, where

$$H_0 : \boldsymbol{x} = \boldsymbol{\lambda}. \tag{3.3}$$

As λ_k is sufficiently large in the regime of spectral imaging, N_k can be approximated to a Gaussian distribution. For measurements consisting of $n = 1$ bin, the null hypothesis can be tested using a two-tailed z-test with the test statistic

given by

$$z = \frac{\boldsymbol{x} - \boldsymbol{\lambda}}{\boldsymbol{\sigma}} = \frac{x_1 - \lambda_1}{\sqrt{\lambda_1}} = \frac{x - \lambda}{\sqrt{\lambda}}. \tag{3.4}$$

The standardised distance, expressed as the z-score in (3.4), provides a measure of the difference between two mean values in the number of standard deviations (Rencher 1995). Measurements that are one Poisson standard deviation ($\sqrt{\lambda_k}$) away from the mean would result in a value of $z = 1$ in the formulation and an acceptance region of 68.3% (see e.g. James (2006)). A 15.8% rejection region can thus be setup for each of the two tails of the distribution, corresponding to a z-score of $z = \pm 1$. The null hypothesis can be accepted for an observed z-score of $|z| \leq 1$ and the thickness t of $m = 1$ material is considered consistent with the measurement $\boldsymbol{x} = x$ for $n = 1$ energy bin. Similarly, a larger acceptance region can be formed e.g. 95.4% with $z = \pm 2$.

For $n > 1$ energy bins, the Mahalanobis distance (MD), which is an equivalent measure to (3.4) for higher dimensions (Rencher 1995), is calculated between $\boldsymbol{x}$ and $\boldsymbol{\lambda}$. Under the assumption that N_k is uncorrelated within an individual set of $\boldsymbol{t}$, the MD is

$$\begin{aligned}
z &= \left\{ \sum_{k=1}^{n} \left[\frac{(x_k - \lambda_k)}{\sigma_k} \right]^2 \times \frac{1}{n} \right\}^{\frac{1}{2}} \\
&= \left\{ \left[\sum_{k=1}^{n} \left(x_k - \lambda_k(\boldsymbol{t}) \right)^2 \times \frac{1}{\lambda_k(\boldsymbol{t})} \right] \times \frac{1}{n} \right\}^{\frac{1}{2}},
\end{aligned} \tag{3.5}$$

in which a factor of $1/n$ has been introduced for convenience to negate the dependency of z on the number of energy bins. Mapping the z-score in the thickness space therefore leads to an elliptical contour plot for $m = 2$ materials and $n = 2$ bins, indicating a multivariate normal distribution (Rencher 1995, James 2006). A confidence region formed by a z-score of unity is shown as the black ellipse in figure 3.1, which contains a probability content, β, of 63%. The β-value may be interpreted as meaning that there is a 63% chance that given a measurement

$\boldsymbol{x}$, the actual thicknesses would lie within this particular region. Similarly, the 98% confidence region formed by a z-score of 2 is represented by the grey ellipse. Located at the center of the two-dimensional ellipse is a z-score of zero, corresponding to $\boldsymbol{\tau} = \{\tau_i\}, i = 1, \ldots, m$, where $\boldsymbol{\tau}$ is the combination of thicknesses that is most consistent with the measurement $\boldsymbol{x}$. The confidence ellipse can be expanded into any higher dimensions e.g. a volume for $m = 3$ materials.
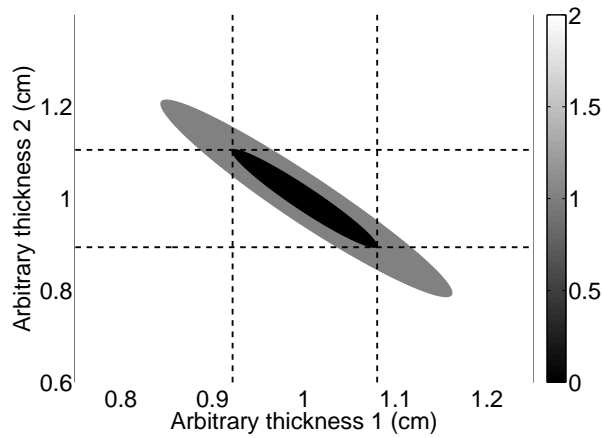
Figure 3.1: *The black ellipse marks the 63% confidence region formed by a z-score of unity. The colorbar indicates the value of the z-score. The outer ellipse represents the confidence region for a z-score of 2 for $m = 2$ materials, encompassing a probability content of 98%. Expanding this to $m = 3$ materials results in a confidence volume.*

3.1.2 Statistical verification

To statistically verify the metric, the measurement $\boldsymbol{x}$ is simulated using (3.2) for a known set of materials and a incident given x-ray spectrum. A reference set of thicknesses $\boldsymbol{\tau}$ has to be defined *a priori* for this purpose. The probability content, β, of any 2-dimensional isovalue contour (or volume for $n = 3$) can then be determined by assuming a multivariate Gaussian distribution $N_p(\boldsymbol{x}, \Sigma_x)$ with $p = n$ degrees of freedom, where $\boldsymbol{x}$ and Σ_x are the mean vector and the covariance matrix of the distribution $N_p(\boldsymbol{x}, \Sigma_x)$, respectively. Let $\boldsymbol{\theta} = \{\theta_i\}, i =$

$1, \ldots, m$ represent the thickness set that is most consistent with a particular random member of this distribution and let Θ be a $s \times m$ matrix consisting of s vectors of $\boldsymbol{\theta}$. Θ can be constructed by solving (3.2) for $\boldsymbol{t}$ for a given random sample of size s from the distribution $N_p(\boldsymbol{x}, \Sigma_x)$. Specifically, the confidence region formed by all $\boldsymbol{\theta}$ with

$$\boldsymbol{\zeta}'\boldsymbol{\zeta} = (\boldsymbol{\theta} - \boldsymbol{\tau})'(\Sigma_t)^{-1}(\boldsymbol{\theta} - \boldsymbol{\tau}) \leq \chi_p^2(\alpha) \qquad (3.6)$$

contains $\beta = (1-\alpha)$ percentage of Θ, where $\boldsymbol{\zeta} = (\Sigma_t^{1/2})^{-1}(\boldsymbol{\theta} - \boldsymbol{\tau})$ (Rencher 1995).

Σ_t represents the covariance matrix of all the thickness solutions and $\chi_p^2(\alpha)$ is the upper $(100 \times \alpha)^{th}$ percentile of a chi-square distribution with $p = n$ degrees of freedom. With the uncorrelated N_k in the simulated distribution $N_p(\boldsymbol{x}, \Sigma_x)$, it follows from (3.5) and (3.6) that $z^2 = (\boldsymbol{\zeta}'\boldsymbol{\zeta})/n$ (Rencher 1995). A Poisson counting noise of $\sqrt{\lambda_k}$ would hence give rise to $z = 1$ in (3.5), which leads to e.g. a χ^2 value of 2 for $p = n = 2$ degrees of freedom.

The β values obtained were verified by means of a straightforward MC simulation, against chi-square statistics for probabilities ranging from 0.25 to 0.01 for $p = n = 2$ and $p = n = 3$ degrees of freedom. Setting a threshold of unity for z, by virtue of the Poisson counting noise, introduced a β value of 63% for $p = n = 2$. Likewise, a confidence volume of 61% can be obtained with $z = 1$ for $p = n = 3$.

3.1.3 Thickness uncertainties

In Roessl & Herrmann (2009) and Wang & Pelc (2011), threshold performance was maximised based on variance of a single material upon determining the CRLB based on the Fisher information matrix. We propose a novel alternative that does not require the iterative determination of the effective basis functions or

the manipulation of the Fisher information, thereby simplifying the approach. Qualitatively, the size of the confidence region gives an indication of the optimality of the energy bins. However, quantitatively measuring the area (or volume) of the elliptical region requires the covariance matrix of the thickness population. The bounding box of the ellipsoidal confidence region, as depicted in figure 3.1, enables the calculation of the standard deviations (σ) and correlation coefficient (ρ) of the thicknesses for the formation of the covariance matrix of the thickness population, V (James 2006):

$$V = \begin{pmatrix} \sigma_1^2 & \rho\sigma_1\sigma_2 & \rho\sigma_1\sigma_3 \\ \rho\sigma_1\sigma_2 & \sigma_2^2 & \rho\sigma_2\sigma_3 \\ \rho\sigma_1\sigma_3 & \rho\sigma_2\sigma_3 & \sigma_3^2 \end{pmatrix}.$$

To optimise, we combine σ_i and τ_i of all materials of interest to formulate our figure of merit (FOM) as

$$\text{FOM} = \left(\sum_{i=1}^{m} (\sigma_i/\tau_i)^2 \right)^{-\frac{1}{2}}. \tag{3.7}$$

Given the number of energy bins n, the objective of the model is to locate $E_{(l,k)}$ and $E_{(h,k)}$ for $k = 1, \ldots, n$ that give the smallest confidence region in the thickness space to maximise the FOM. An exhaustive search through the space of all possible combinations of energy bins $E_{(l,k)}$ and $E_{(h,k)}$ is feasible with low n, e.g. $n \leq 3$. Alternatively, an optimisation module such as the Simulated Annealing algorithm (Kirkpatrick 1984) can be employed for higher values of n. It should be noted that among $n = 2, 5, 10$ energy bins, $n = 5$ is claimed to provide an optimal compromise between the image quality and the complexity of the PCD electronics (Shikhaliev 2006). Increase in SNR was shown to be relatively minor for the increase from $n = 5$ to $n = 10$.

3.1.4 Model testing

For the purpose of testing the characteristics of the above model, two simplified hypothetical attenuation and an incident x-ray spectra were chosen (figure 3.2). The attenuation profiles in figure 3.2a were flat except for a deliberate step in one of the spectra to enable the prediction of results from specified test cases. A $E_{(l,1)}$ of 10 keV was set to suppress the electronic noise floor of PCDs (Delpierre et al. 2002, Butler et al. 2008, Bornefalk & Danielsson 2010), while a $E_{(h,2)}$ of 120 keV represents the common x-ray tube voltage of 120 kVp.

For the incident x-ray spectrum, a stepwise function was chosen to provide an approximation of a realistic x-ray spectrum as shown in figure 3.2b. The step at 41 keV in the attenuation spectrum for material T2 reflects the K-edge of a material. The performance of the model was examined using two bins with 1 keV bin width. Furthermore, two adjacent bins with wider bin widths were formed by setting $E_{(l,2)} = E_{(h,1)} + 1\,\text{keV}$. This is equivalent to identifying $E_{(h,1)}$ with the highest FOM as the optimal bin border position.
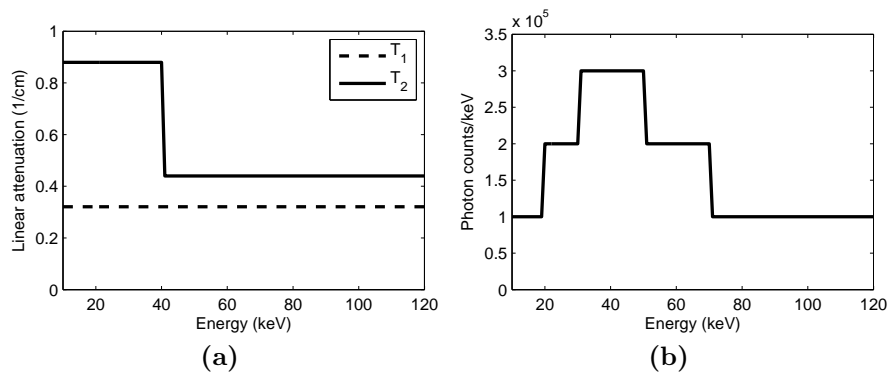
Figure 3.2: *(a) Simplified attenuation and (b) x-ray energy spectra used to test the model. Deliberate steps were included in the spectra for predictions of results in model verification.*

3.2 Model application

The attenuation spectra of iodine, water and calcium were employed to implement the model on realistic cases. The attenuation values were provided by the XCOM Photon Cross Sections Database (Berger et al. 2005). Energy was considered discretely in steps of 1 keV. An incident x-ray spectrum from a tungsten/rhenium anode with a tube voltage of 120 kVp and target angle of 8° shown in figure 3.3 was modelled, following a bench-marked model by Tucker, Barnes & Chakraborty (1991). This was achieved using the established MC code system BEAMnrc (Rogers et al. 1995). The internal tube filtration included 1.5 mm of beryllium and 2.7 mm of aluminum, as specified by Roessl & Proksa (2007). The tube current was set to be 0.15 mA to enable the comparisons of results with those of Wang & Pelc's (2011).
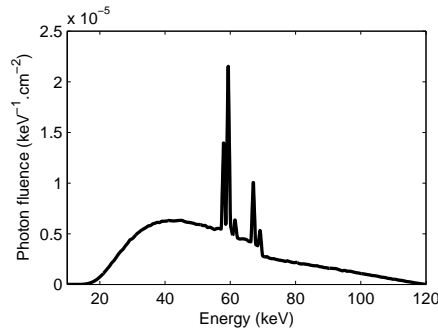
Figure 3.3: *Incident x-ray spectrum employed in model application. This was modelled for a 90/10 atomic percent tungsten/rhenium alloy target (Tucker, Barnes & Chakraborty 1991) with a target angle of 8°. The tube voltage was 120 kVp with internal tube filtration of 1.5 mm beryllium and 2.7 mm aluminum (Roessl & Proksa 2007).*

3.2.1 Discriminating materials with K-edge

Iodine is widely used as a contrast agent in CT imaging, while water and calcium serve as representations of soft tissue and bone, respectively. The differ-

entiation of iodine from these materials has been demonstrated using DECT (Flohr et al. 2006), as well as spectral CT for small animal imaging (Anderson et al. 2010) and breast imaging (Shikhaliev 2008b). The bin border position of two adjacent bins was optimised for the combinations of iodine/calcium and iodine/water, in the same manner as for the artificial attenuation spectra in section 3.1.4. The reference thicknesses for calcium, τ_{Ca}, was chosen to be 0.22 cm to approximately match the total transmittance of 0.01 cm of iodine over the entire energy range considered. For demonstration purposes, we have chosen the density to be 4.93 g cm^{-3} and 1.55 g cm^{-3} for iodine and calcium, respectively.

Another demanding challenge in medical imaging is the identification of thin materials amongst other biological tissues. For this reason, a τ_{H_2O} was defined to be 1.5 cm for the discrimination of iodine and water. This, too, gives an overall transmittance comparable to 0.01 cm of iodine. Furthermore, the two borders ($E_{(h,1)}$ and $E_{(h,2)}$) of three adjacent bins were optimised for iodine, calcium and water for the foregoing reference thicknesses. The choice of iodine in this metric is to demonstrate the effect of optimised energy thresholds on the discrimination of materials with a K-edge discontinuity. However, it should be noted there is nothing unique about iodine. Materials with K-edge energies suitably situated to provide sufficient transmittance in all energy bins, such as barium and gadolinium could act as a substitute to iodine in this model application.

3.2.2 Discriminating materials without K-edge

To serve as a comparison to the optimal bin positions for separating calcium and water computed by Wang & Pelc (2011), the attenuation spectra of calcium and water, as well as as a $E_{(l,1)}$ of 20 keV were used. Reference thicknesses of 0.5 cm for calcium and 20 cm for water were employed (Wang & Pelc 2011). In addition to the optimal border of two abutted bins, the optimal values of $E_{(h,1)}$

and $E_{(l,2)}$ for two separated bins were verified against the previous study. For the discrimination of two materials with similar attenuation coefficient, attenuation spectra of water and fat were chosen to represent glandular tissue and adipose tissue, respectively, in a human breast (Shikhaliev 2008b). An equal reference thickness of 1 cm was defined for both fat and water and $E_{(l,1)}$ was set to be 10 keV for the same reason presented in section 3.1.4. The final application of the model presented in this work was on the discrimination of 0.1 cm of calcium, 1 cm of water and 1 cm of fat, resembling microcalcification, glandular tissue and adipose tissue, respectively.

3.2.3 Counts per pixel estimation

For a given incident x-ray spectrum, a pertinent problem is to determine the minimum exposure to achieve an imaging task. The Rose's criterion (Rose 1946) of SNR ≥ 5 is often used as a target for image quality (e.g. in Ducote et al. (2011)). When decomposing a homogenous material i with thickness τ_i, the SNR within the uniform region-of-interest (ROI) can be provided by the ratio of the reference thickness to the standard deviation of thickness population, (τ_i/σ_i). Likewise, in estimating the material quantity in a pixel, σ_i represents the uncertainty in the estimation. An imaging task can be setup as achieving the τ_i/σ_i value of 5, in the quantification of thickness τ_i, or in the homogenous ROI of the decomposed image i. The minimum number of photons per unit area required in order to accomplish the imaging task can be subsequently computed to fulfill the ALARA principle (Slovis 2003).

To directly compare with the BEAMnrc MC simulation in chapter 4, however, in this work, the image noise was estimated for the simulated detected counts. The image noise is computed as variance (σ_i^2) as in Roessl et al. (2011) and Ducote et al. (2011). It can be seen later that the simulated image noise is readily avail-

able upon decomposing the simulated projection. In the optimisation metric, the diagonal elements of the covariance matrix described in section 3.1.3 incorporates σ_i^2 and can therefore be utilised for the prediction of image noise (or SNR). This enables a direct comparison between the σ_i^2 values obtained from the metric and the simulation. For the discrimination of iodine/water, σ^2 was determined at an interval of $1\,\mathrm{keV}$ for $E_{(h,1)}$ ranging from $20\,\mathrm{keV}$ to $100\,\mathrm{keV}$, whereas $E_{(h,1)}$ was fixed at $33\,\mathrm{keV}$ and σ^2 was computed for $E_{(h,2)}$ between $36\,\mathrm{keV}$ to $100\,\mathrm{keV}$ for the discrimination of iodine, calcium and water.

3.3 Results

3.3.1 Model testing

With the hypothetical spectra in figure 3.2a and using two $1\,\mathrm{keV}$ bins, the metric produces the expected results. Given the same attenuation values, higher incident photon counts provides a higher SNR and hence a better discrimination of materials. This is illustrated in figure 3.4 where the FOM is optimal when N_0 in figure 3.2b is the highest with $E_{(l,1)}$ between $31\,\mathrm{keV}$ and $40\,\mathrm{keV}$ ($E_{(h,1)} = E_{(l,1)} + 1\,\mathrm{keV}$) and $E_{(l,2)}$ between $41\,\mathrm{keV}$ and $50\,\mathrm{keV}$ ($E_{(h,2)} = E_{(l,2)} + 1\,\mathrm{keV}$). The FOM increases according to a factor of $\sqrt{\delta N}$ where δN is the factor of increment in number of incident counts. For the given hypothetical x-ray spectrum, the incident counts at e.g. $E_{(l,1)} = 35\,\mathrm{keV}$ and $E_{(l,2)} = 45\,\mathrm{keV}$ is higher by a factor of 1.5 than those of $E_{(l,1)} = 25\,\mathrm{keV}$ and $E_{(l,2)} = 60\,\mathrm{keV}$. A FOM of 36.2 for $E_{(l,1)} = 35\,\mathrm{keV}$ and $E_{(l,2)} = 45\,\mathrm{keV}$ is correspondingly $\sqrt{1.5}$ times higher than 29.6 for $E_{(l,1)} = 25\,\mathrm{keV}$ and $E_{(l,2)} = 60\,\mathrm{keV}$. The materials are understandably indistinguishable for energy levels that exhibit the same attenuations, i.e. when $E_{(l,1)}$ and $E_{(l,2)}$ are simultaneously located below $40\,\mathrm{keV}$ or above $41\,\mathrm{keV}$. The optimal border for two adjoined bins with $E_{(l,1)}$ and $E_{(h,2)}$ at $10\,\mathrm{keV}$ and $120\,\mathrm{keV}$, respec-

tively, agrees with the deliberate step in attenuation spectrum T2 in figure 3.2a, i.e. optimal $E_{(h,1)} = 40\,\mathrm{keV}$ ($E_{(l,2)} = 41\,\mathrm{keV}$).
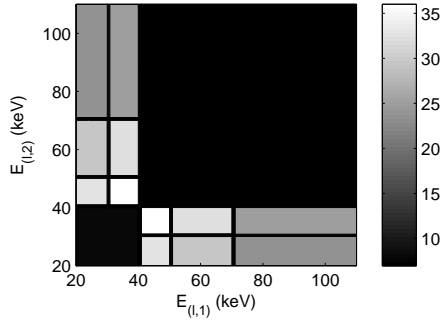
Figure 3.4: *FOM for distinguishing hypothetical attenuation spectra T1 and T2 and x-ray spectrum presented in figure 3.2 using two 1 keV bins. Expectedly, the FOM increases according to a factor of $\sqrt{\delta N}$, where δN is the factor of increment in number of incident counts. See text for detailed FOM increment.*

3.3.2 Discriminating materials with K-edge

For distinguishing $0.01\,\mathrm{cm}$ of iodine and $0.22\,\mathrm{cm}$ of calcium, the results show that $E_{(h,1)}$ of $33\,\mathrm{keV}$ ($E_{(l,2)} = 34\,\mathrm{keV}$) is determined to be the optimal bin border position as shown in figure 3.5, which coincides with the K-edge discontinuity in the iodine attenuation spectrum. This is consistent with previous work by Roessl & Herrmann (2009), in which an energy threshold placed at the K-edge of gadolinium is shown to provide the best SNR in the gadolinium basis image.

For the case of $0.01\,\mathrm{cm}$ of iodine and $1.5\,\mathrm{cm}$ of water, a FOM of 91.5 is obtained for $E_{(h,1)}$ of $60\,\mathrm{keV}$ ($E_{(l,2)} = 61\,\mathrm{keV}$). This offers a 33.8% improvement compared to the FOM of 68.4 for $E_{(h,1)}$ located at the K-edge of iodine ($33\,\mathrm{keV}$). Figure 3.5b shows the 63% confidence regions of the thickness estimates for $E_{(h,1)} = 60\,\mathrm{keV}$ and $E_{(h,1)} = 33\,\mathrm{keV}$, circumscribed by the same isoline of $z = 1$ defined in section 3.1.1. The improved accuracy in estimating material thicknesses is apparent with the smaller confidence region for $E_{(h,1)} = 60\,\mathrm{keV}$ shown in figure 3.5b.

For the case with three materials, $E_{(h,1)}$ of 33 keV and $E_{(h,2)}$ of 51 keV are determined to be optimal with a FOM of 56.16 for the separation of 0.01 cm of iodine, 0.22 cm of calcium and 1.5 cm of water using three abutted energy bins (Figure 3.6a). The optimal confidence volume is displayed in figure 3.6b.
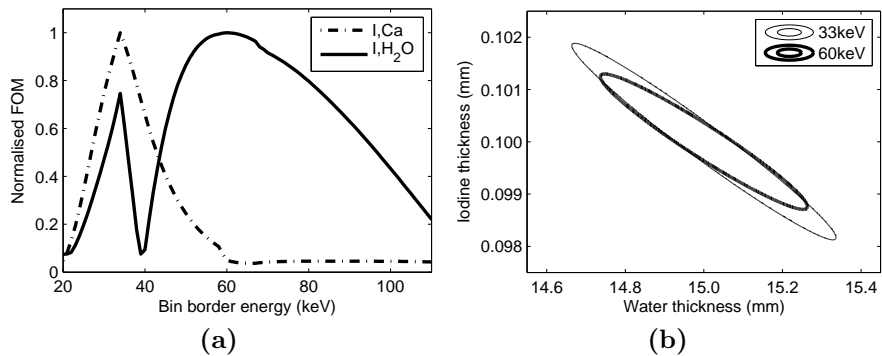
Figure 3.5: *(a) Normalised FOM for 0.01 cm of iodine/0.22 cm of calcium and for 0.01 cm of iodine/1.5 cm of water. The highest FOM for iodine/calcium occurs when the border of two adjacent bins is located at the K-edge of iodine (33 keV). Two bins bordering at 60 keV provides the highest FOM in the iodine/water discrimination. optimised bins are capable of providing 33.8% better discrimination than two bins bordering at the iodine K-edge, seen as the smaller 63% confidence region (thick line) in (b). The 63% confidence region for $E_{(h,1)} = 33$ keV enclosed by the same $z = 1$ contour line is plotted using thin line for comparison.*

3.3.3 Discriminating materials without K-edge

A previous study shows that by having $E_{(l,1)} = 20$ keV and $E_{(h,2)} = 120$ keV, the optimal bin border for two abutted bins for discriminating 0.5 cm of calcium and 20 cm of water is located at 55 keV (Wang & Pelc 2011). In our metric, $E_{(h,1)}$ of 55 keV ($E_{(l,2)} = 56$ keV) or $E_{(h,1)}$ of 56 keV ($E_{(l,2)} = 57$ keV) yields an equal maximum of 24.3 in the FOM. A comparably good agreement (within $\pm$ 1 keV) is achieved for two disjoined bins with $E_{(h,1)}$ of 53 keV and $E_{(l,2)} = 74$ keV producing the highest FOM of 27.5 (9% improvement in FOM compared to the two adjoined bins). We determined that optimal energy thresholds of $E_{(h,1)}$ of
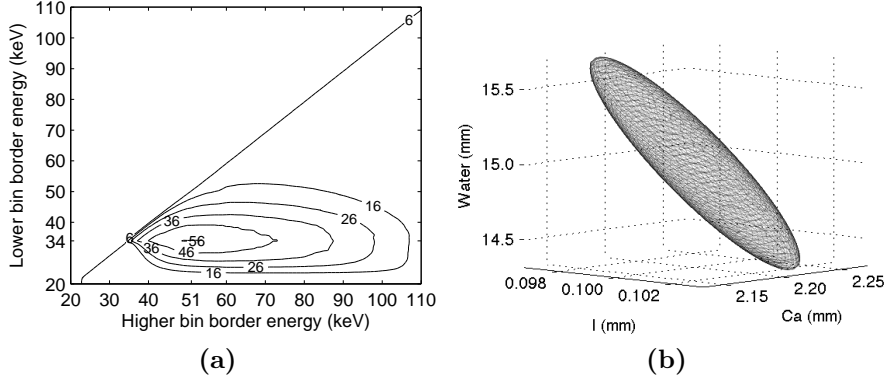
Figure 3.6: *(a) FOM for discriminating* 0.01 cm *of iodine,* 0.22 cm *of calcium and*
1.5 cm *of water using three abutted energy bins. The K-edge of iodine* ($E_{(h,1)} =$
33 keV*) and* $E_{(h,2)} = 51$ keV *are optimal (marked by contour level 56). (b) Wire-*
frame of the 61% confidence volume for the optimal bins. Note the small range on
the thickness axes.

53 keV and $E_{(l,2)} = 73$ keV proposed by Wang & Pelc (2011) give an equivalently
high FOM after rounding up to 3 significant figures. A summary of comparisons
between the two methods is shown in table 3.1.

The results for 1 cm of fat and 1 cm of water are presented in figure 3.7a.
The optimal confidence region obtained with $E_{(h,1)}$ of 33 keV ($E_{(l,2)} = 34$ keV) is
compared to that of iodine/calcium in figure 3.7b. The 63% confidence region for
water and fat shows uncertainties of greater than 10% for both materials; uncer-
tainties for iodine and calcium are about 1%. The FOM for the discrimination of
1 cm of fat, 1 cm of water and 0.1 cm of calcium using three abutted energy bins
ranges from 2.42 to 2.48, indicating that the optimisation of $E_{(h,1)}$ and $E_{(h,2)}$ does
not have a substantial effect on the FOM. When compared to figure 3.6b, the 61%
confidence region is clearly elongated on the axes of water and fat (figure 3.8).

3.3.4   Counts per pixel estimation

Image noise (σ^2) was computed for the discrimination of two and three materials.
These are plotted at an interval of 1 keV in figure 3.9 and figure 3.10, respectively.

	Two abutted bins	Two separated bins
	Optimal border	Optimal thresholds
Nik *et al.*	$E_{(h,1)} = 55\,\text{keV}$	$E_{(h,1)} = 53\,\text{keV}$
	(Equivalently $E_{(h,1)} = 56\,\text{keV}$)	$E_{(l,2)} = 74\,\text{keV}$
Wang & Pelc (2011)	$E_{(h,1)}$ around $55\,\text{keV}$	$E_{(h,1)} = 53\,\text{keV}$
		$E_{(l,2)} = 73\,\text{keV}$

Table 3.1: Comparison of optimal energy thresholds for discriminating $0.5\,\text{cm}$ calcium and $20\,\text{cm}$ water between the proposed metric and the method based on the maximum likelihood estimator used by Wang & Pelc. Positions of energy thresholds agree to within $\pm\,1\,\text{keV}$. Two separated bins improve the FOM by 9% compared to two abutted bins (see text for FOM values).

The lowest σ^2 values can be found at the corresponding optimal $E_{(h,1)}$ and $E_{(h,2)}$ values presented in section 3.3.2. The vertical axis was rescaled in the lower panel of figure 3.9 to provide an enlarged view around the optimal σ^2. A step-wise function can be noted in figure 3.10, particularly in figure 3.10b, which was due to a limit on the memory allocation imposed by Matlab (Mathworks Inc.).

For iodine and water, the optimal σ^2 are $6.63 \times 10^{-6}\,\text{cm}^2$ and $2.60 \times 10^{-1}\,\text{cm}^2$, respectively. In the discrimination of 3 materials, these are $6.11 \times 10^{-6}\,\text{cm}^2$, $3.04 \times 10^{-3}\,\text{cm}^2$ and $2.67 \times 10^{-1}\,\text{cm}^2$, for iodine, calcium and water respectively. It should be noted that the σ^2 values were computed based on the photon flux simulated in the BEAMnrc model, which will be presented in more details in chapter 4. A table summarising the optimal σ^2 values can hence be found in table 4.1. This is to enable the comparisons with σ^2 values obtained from the simulation (see figure 4.8 and figure 4.9).

3.4 Discussion

Previous works studied the optimisation of energy windows for material separation by examining the SNR between the transmitted signal of two objects (Tapiovaara & Wagner 1985), as well as by computing the CRLB of material
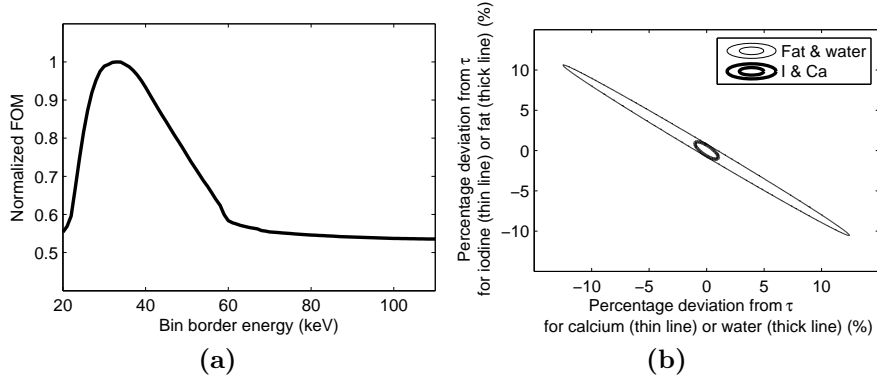
Figure 3.7: *(a) Normalised FOM plot for* 1 cm *of fat and* 1 cm *of water. The highest FOM is found at $E_{(h,1)}$ of* 33 keV *($E_{(l,2)} = 34$ keV) with $E_{(l,1)} =$10 keV and $E_{(h,2)} = 120$ keV. (b) The optimal confidence regions for water and fat (thin line) are compared to that of iodine and calcium (thick line). The estimation of water and fat thickness yielded uncertainties of greater than 10% at best, which is much larger than the optimal uncertainties of iodine and calcium (about 1%).*

estimates (Roessl & Herrmann 2009, Wang & Pelc 2011). Employing the statistical detection theory, Alvarez (2010) examined the detector performance for differentiating a feature from a background material. While the goal of our model is largely similar to the published methods, the Mahalanobis distance (z-score for higher dimensions) allows for a measure of statistical consistency between the thicknesses and a given measurement of photon counts without requiring the Fisher information (CRLB) or the determination of the effective attenuation basis functions. Extensive sampling of the thickness space enables the map of the correlated thickness estimates to be constructed. Circumscribing the quantitative bound on the confidence region allows for the uncertainties of material thickness estimation to be computed.

Material (or attenuation) basis images can be obtained upon decomposing projection data using the maximum likelihood process (Roessl & Proksa 2007) or the least squares theory (Le & Molloi 2010). The MD in (3.5) is equivalent to the latter without requiring the determination of effective attenuation coeffi-
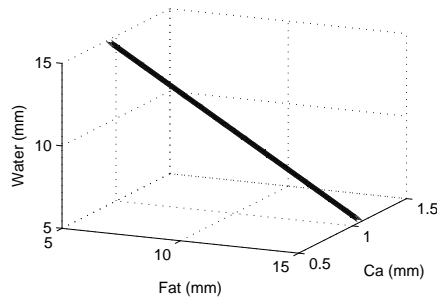
Figure 3.8: *The 61% confidence region for separating* 1 cm *of fat,* 1 cm *of water and* 0.1 cm *of calcium using three equidistant bins. The similar attenuations of water and fat extends the confidence region throughout the entire ranges of water and fat thicknesses. FOM for all combinations of $E_{(h,1)}$ and $E_{(h,2)}$ lie between 2.4 and 2.5. The limited range of the FOM suggests that optimising $E_{(h,1)}$ and $E_{(h,2)}$ between* 20 keV *and* 110 keV *has no noticeable effect on the discrimination of* 1 cm *of fat,* 1 cm *of water and* 0.1 cm *of calcium using three abutted energy bins.*

cient. Pixelated measurements can be compared to the expected counts for any statistically significant differences, which will be presented in chapter 4. Further, Wang & Pelc (2011) considered only the variance of one material in their penalty factor, i.e. the variance for calcium. While the incorporation of all materials of interest in the FOM is straightforward, the relatively small amount of calcium becomes the driving component in our FOM. An agreement of optimal thresholds is therefore achieved with Wang & Pelc's (2011) numerical example of 0.5 cm calcium and 20 cm of water.

For three materials without K-edge within the imaging energy spectrum, two materials can be separated as any one of the materials is a linear combination of the remaining pair. Utilising the mapping of thickness uncertainties, the confidence region in figure 3.8 reveals a thin elongated volume, indicating only one material (calcium), along with the sum of water and fat can be resolved. The relative proportion of water and fat cannot be determined, which is expected given the linear dependence of the three material attenuation profiles.

The linear attenuation ratio between iodine and calcium, plotted in figure 3.11,
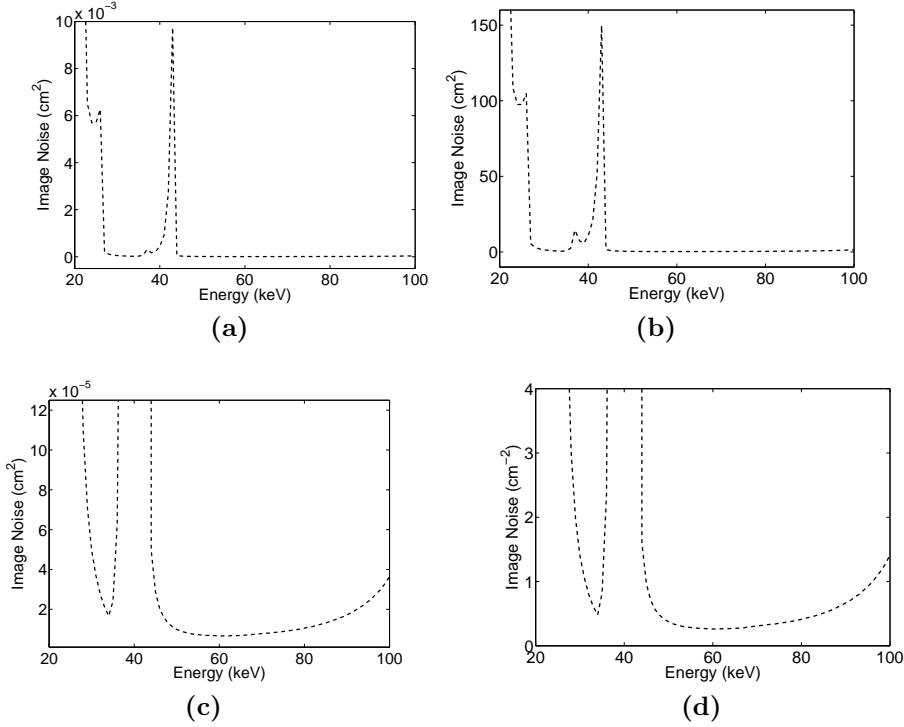
Figure 3.9: Image noise (σ^2) as predicted by the covariance matrix for (a) iodine
and (b) water in the discrimination of iodine/water. Note that the σ^2 values were
computed based on the photon flux simulated in the BEAMnrc model, which will
be presented in chapter 4. The vertical axis was rescaled in the lower panel plotted
to focus on the lowest σ^2 values for (c) iodine and (d) water at the optimal $E_{(h,1)}$
value.

describes the dissimilarity of the two materials at each energy. This is influenced
by the number of incident photons for maximum material discrimination. The
lowest and highest attenuation ratios of iodine and calcium are binned separately
when $E_{(h,1)} = 33\,\text{keV}$, which justifies the coincidence of optimal $E_{(h,1)}$ with the
K-edge of iodine. For the separation of iodine and water, however, there exists
another FOM peak at an energy different from the K-edge of iodine realising the
ideal combination of ratio balance and statistics in both windows for the given
incident spectrum. With two bins abutting at the iodine K-edge ($33\,\text{keV}$), the
low ratios weighted by the low counts at the highest energies partially neutralise
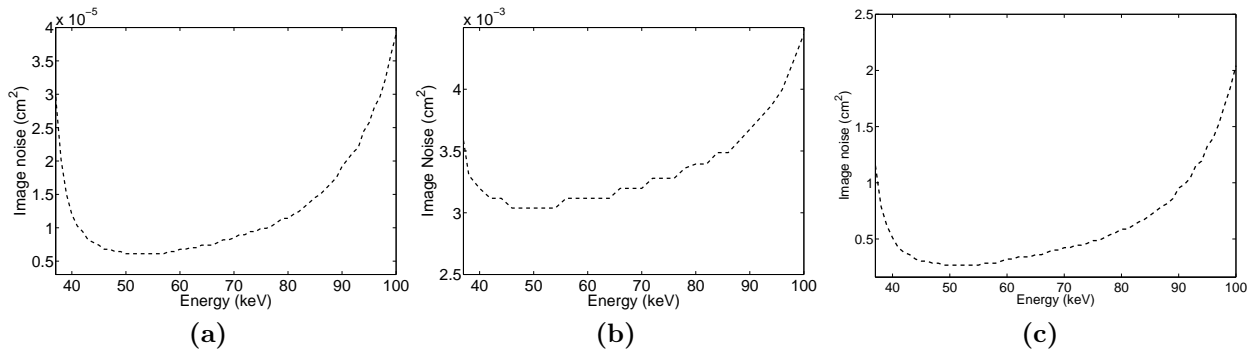
Figure 3.10: Image noise (σ^2) as predicted by the covariance matrix for (a) iodine, (b) calcium and (c) water for the discrimination of 3 materials. The step-wise function in (b) was caused by a limit on the largest matrix size and the maximum element in an array allowed in Matlab.

the maximum ratios immediately above the K-edge, causing the mean ratio in bin $k = 2$ to be moderately high. The mean ratio in bin $k = 1$ remains low and this leads to the local FOM peak at the K-edge of iodine as shown in figure 3.6a. The dip in the FOM value indicates that both bins have similar weighted mean ratios when $E_{(h,1)} \approx 40 \, \text{keV}$. Increasing $E_{(h,1)}$ above $40 \, \text{keV}$ contributes more high ratios into bin $k = 1$ while lowering the mean in bin $k = 2$. An optimum is reached as $E_{(h,1)}$ approaches $60 \, \text{keV}$, which gives rise to the FOM peak in figure 3.6a.

To demonstrate that this result and its explanation are not unique to the particular iodine and water thicknesses, the optimal bin border positions for two additional iodine thicknesses, namely $0.005 \, \text{cm}$ and $0.02 \, \text{cm}$, were computed with a constant τ_{H_2O} of $1.5 \, \text{cm}$. The location of the highest FOM value changes according to the iodine thickness. When compared to values presented in section 3.3.2, optimal $E_{(h,1)}$ for discriminating iodine and water decreases $3 \, \text{keV}$ to $57 \, \text{keV}$ for $\tau_I = 0.005 \, \text{cm}$ and increases to $64 \, \text{keV}$ for $\tau_I = 0.02 \, \text{cm}$, with a FOM of 78.0 and 85.4 for the earlier and latter cases, respectively. For the same rationales mentioned above, a local maximum exists for all three thicknesses of iodine when $E_{(h,1)} = 33 \, \text{keV}$, as illustrated in figure 3.12. The higher optimal $E_{(h,1)}$ energy
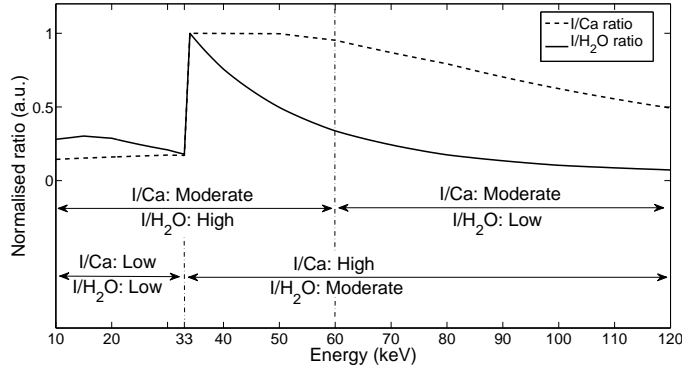
Figure 3.11: *Normalised linear attenuation ratio for iodine/water (solid line) and
iodine/calcium (dotted line). Relative means of attenuation ratios are indicated
with texts in the figure below the curves. When weighted by the incident spectrum,
an optimal difference in attenuation ratios between the two energy bins (leads to
optimal material contrast) can be produced by setting $E_{(h,1)}$ to be $60\,keV$ for the
discrimination of iodine and water. Furthermore, the same is achieved for iodine
and calcium when $E_{(h,1)} = 33\,keV$, which justifies the position of the highest FOM
for the two materials in figure 3.6a.*

is expected for thicker τ_I in order to compensate for the lower counts in bin
$k = 1$ due to the beam hardening effect by a greater thickness of iodine (Roessl &
Proksa 2006). $E_{(h,1)}$ of $60\,keV$ for $\tau_I = 0.01\,cm$ encompasses the characteristic K_{α_1}
and K_{α_2} x-ray lines of tungsten, located at $58.0\,keV$ and $59.3\,keV$, respectively
(Deslattes et al. 2005). This counteracts the doubling of iodine thickness from
$\tau_I = 0.005\,cm$ to $0.01\,cm$ to provide ample counts in bin $k = 1$. An expected
increase of $E_{(h,1)}$ to $64\,keV$ can be seen for $\tau_I = 0.02\,cm$.

Regarding figure 3.10b, the step-wise function is due to a limit in Matlab on
the largest possible matrix size and the maximum element in an array allowed.
This imposed a limit on the step size of the thickness range that could be sam-
pled to form our confidence region. This subsequently hinders the resolution on
the change of the size of the confidence region. For the decomposition of two
materials, the typical sample size is 300 - 400 in one dimension (with other arrays
formed). For the decomposition of three materials, the upper limit is 200 in one
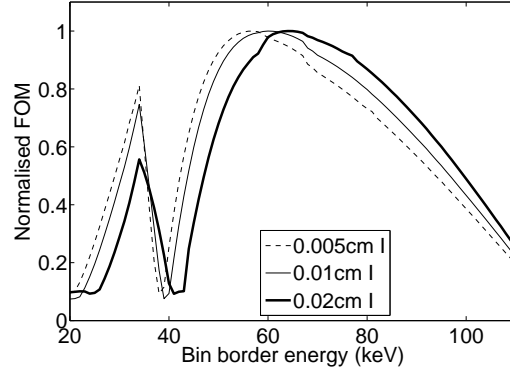
Figure 3.12: *Normalised FOM for discriminating three thicknesses of iodine, namely* 0.005 cm, 0.01 cm *and* 0.02 cm *from* 1.5 cm *of water. Results for* $\tau_I = 0.01$ cm *and* $\tau_{H_2O} = 1.5$ cm *in figure 3.5a is repeated using the thin solid line. With* $E_{(l,1)} = 10$ keV *and* $E_{(h,2)} = 120$ keV, *local maxima occur at the K-edge of iodine for all three thicknesses of iodine while the highest FOM value in each of the three cases is found at* 57 keV, 60 keV *and* 64 keV *for* $\tau_I = 0.005$ cm, 0.01 cm *and* 0.02 cm, *respectively.*

dimension before Matlab ran out of allocated memory. One potential solution is to run the code on a different platform with the combination of a different version of Matlab[1].

3.5 Concluding remarks

A novel method to optimise energy windows for material discrimination in spectral x-ray imaging with photon counting detectors was developed. The proposed framework framework maps the z-scores in the thickness space for consistency with the measured counts. Multivariate statistics enables the confidence region of the thickness estimates to be constructed. Energy bins are optimised according to the bounding box of the confidence region without requiring the Fisher information (CRLB). The covariance matrix of the thickness population can be formulated without the determination of the effective attenuation basis functions.

---

[1] http://www.mathworks.com/support/solutions/en/data/1-IHYHFZ/index.html

Employing adjacent energy bins with fixed ends, the bin border position is optimised for different biological materials and radiological contrast agents significant to small animal and breast imaging. In concurrence with a study on the effectiveness of gadolinium quantification upon varying one threshold energy (Roessl & Herrmann 2009), separation of iodine and calcium was found to be optimal with the two bins bordering at the K-edge of iodine. Furthermore, a specific comparison with results published by Wang & Pelc (2011) shows agreement on optimal positions of energy thresholds for discriminating $0.5\,\mathrm{cm}$ of calcium and $20\,\mathrm{cm}$ of water to within $\pm\,1\,\mathrm{keV}$.

Two bins abutting at an energy higher than the iodine K-edge are found to be optimal for the discrimination of iodine and water. Given the incident spectrum, this is to achieve a greater difference in the mean attenuation ratios and optimal statistics in both windows. With $1.5\,\mathrm{cm}$ of water, the optimised position of bin border varies from $57\,\mathrm{keV}$ for $0.005\,\mathrm{cm}$ of iodine to $64\,\mathrm{keV}$ for $0.02\,\mathrm{cm}$ of iodine. The increasing position of optimal $E_{(h,1)}$ is to compensate for the reduced photon counts in the lower energy bin due to the beam hardening by the thicker amount of iodine.

The mapping of confidence regions suggest that water (glandular tissue) and fat (adipose tissue) separation may still prove to be practically difficult even with the advent of spectral x-ray imaging. For the discrimination of calcium, water and fat, only the thickness of calcium can be resolved. The elongated confidence region suggests that only the sum of water and fat can be resolved but not the relative proportion of the two materials, as expected.

The covariance matrix incorporates the standard deviation, σ, and was used to compute the prediction of image noise. In order to compare with the image noise of the decomposed projection, variance of thickness estimation, σ^2, was determined based on the simulated counts in the BEAMnrc model. However,

the optimisation framework can be utilised to optimise photon counts required for achieving an imaging target, e.g. a SNR ≥ 5 based on the Rose's criterion. The simulation model, as well as the comparisons, will be presented in details in chapter 4.

Chapter 4

Monte Carlo simulation of optimal material decomposition

Despite its promising potential, the performance of PCDs is at present limited due to charge sharing (Ballabriga et al. 2011a), scattered radiation (Roessl et al. 2011), finite energy resolution (Schlomka et al. 2008) and low read-out speed (Roessl et al. 2010). To investigate the achievable potential of spectral x-ray imaging in quantifying high atomic number materials, for example, Roessl et al. (2011) resorted to the ideal environment of CT simulations to bypass the limitations. Earlier, Roessl & Proksa (2007) simulated the feasibility of K-edge imaging using an energy-resolving photon counting detector. Likewise, Leng et al. (2011) tested their image reconstruction algorithm modified to target noise reduction on simmulated data, while Weigel et al. (2011) generated MC CT images for x-ray tube voltages optimised for a breastlike phantom. The above examples are simulations of x-ray imaging using commercial MC packages, whereas Giersch et al. (2003) compiled an open source simulation tool called Roentgen Simulation based on other established simulation libraries. Roentgen Simulation was later used to study the implementation of a reconstruction technique for ma-

terial quantification by Firsching et al. (2006). Using the MCNP open source package (Brown 2003), Frey et al. (2007) simulated data for the comparisons of DECT and spectral CT in material quantification upon applying their material decomposition method.

Similarly, in this chapter, our approach to decompose spectral x-ray spectrum into material basis images was evaluated using MC simulated data. We chose a different MC simulation code system, known as BEAMnrc (Rogers et al. 1995), because of its availability, ease of use as well as the group's previous experience with the system (Currie 2007, Thing et al. 2011). Noise of the decomposed images was quantified and compared with the theoretical estimates. This leads to the validation of the optimisation of energy bins, which allows the estimation of a theoretical minimum dose achievable with a spectral x-ray detector for obtaining a desired level of SNR in a decomposed image. A dose comparison against a seminal paper on depiction of calcification in mammography can therefore be achieved.

Material of this chapter were presented at the *54th Annual American Association of Physicists in Medicine (AAPM) meeting* in Charlotte, NC, USA in July 2012 (Nik et al. 2012) and a manuscript is in preparation for the *IEEE Transactions on Medical Imaging* based on materials in this chapter.

4.1 Methods

The BEAMnrc system is based on the Electron Gamma Shower code system EGSnrc and comes with extensive documentation (Rogers et al. 2004, Kawrakow et al. 2011, Ma & Rogers 2009) plus interactive graphical interfaces (Treurniet et al. 2009, Kawrakow et al. 2006). BEAMnrc has been widely used predominantly for MeV application for radiotheraphy. The implementation of BEAMnrc

on the lower energy range of keV has been demonstrated for dose calculation in
CT (Bazalova & Verhaegen 2007), material segmentation using DECT (Bazalova
et al. 2008) as well as x-ray fluorescence CT (Bazalova et al. 2012). The recogni-
tion of the package through publication statistics and a review on the advantages
on BEAMnrc over other MC packages was provided by Rogers (2006).

4.1.1   BEAMnrc simulation

Simulations in this work were carried out on the BlueFern® supercomputer at the
University of Canterbury, Christchurch, New Zealand[1]. The scanning geometry
was set up to correspond to the locally built Medipix All Resolution System
(MARS) micro-CT scanner (MARS Bioimaging Ltd, New Zealand) (Butler et al.
2008, Anderson et al. 2010). The 90/10 atomic percent tungsten/rhenium alloy
anode target was simulated with the XTUBE component module. CIRCAPP
was used to replicate the round exit window and SLABS to include the 1.5 mm
beryllium and 2.5 mm aluminum filtration (Roessl & Proksa 2007). The electron
beam impinging on the target was simulated as a 120 keV monoenergetic, parallel
rectangular source energy incident from the side to enable validations of optimal
energy bins with the previous work. More details about the MC model and
validation of it can be found in Thing (2010).

The simulation of the scanning system is split into two parts. First the tube
housing was simulated and a phase space (phsp) file scoring the energy, position,
direction and interaction history of each particle was recorded. The phsp file
immediately after the exit window of the x-ray tube (phsp1 in figure 4.1) was in
turn used as the input to the simulation of particle transport through the imaging
object. The source-to-object distance (SOD) was set to 7.5 cm. A second phsp
file (phsp2 in figure 4.1) was placed at the source to detector distance (SDD) of

---

[1] http://www.bluefern.canterbury.ac.nz

11.5 cm recoding particles reaching the detector plane. Our imaging object was designed using the FLATFILT component module to be a uniform water cylinder containing at least one cylindrical layer of contrast material (see figure 4.1) to allow for decomposition of $m \geq 2$ materials. The layer(s) of contrast material(s) and the water cylinder had a radius of 0.3 cm and 0.6 cm around the beam axis, respectively. Material thicknesses were defined in section 4.1.4 to be the same as in section 3.2.1. Spaces at the back of the x-ray tube filtration and between the imaging object and the detector plane consisted of air specified by the SLABS component module.

Cross sections including Rayleigh scattering were generated with the PEGS4 code system for all the materials used in this work. The directional bremsstrahlung splitting (DBS) and photon forcing were used in the x-ray production to improve simulation efficiency. Examining the effects of simulation options, such as recycling the incident phsp file (Rogers et al. 2004, Treurniet et al. 2009), is out of the scope of this study. The DBS splitting field radius and the source-to-surface distance of the splitting field used were 2.8 cm and 13.5 cm, respectively. National Institute of Standards and Technology (NIST) bremsstrahlung cross-section data was used (Rogers et al. 2004). All MC simulations were run with 3×10^8 primary histories, which is equivalent to 3×10^8 electrons emerging from the x-ray cathode. The cut-off energy was 1 keV for both electrons and photons.

One of the main differences between the BEAMnrc simulation and the optimisation algorithm described in chapter 3 is the inclusion of scattered radiation. In BEAMnrc, the interaction of each particle with the imaging object was tracked via the LATCH bit identification tag to create additional images/spectra with only primary photons. Particle interactions with the air regions were ignored. Information in the phsp files were decoded particle by particle using an in-house developed MATLAB code. The data was organised in a stack of two-dimensional
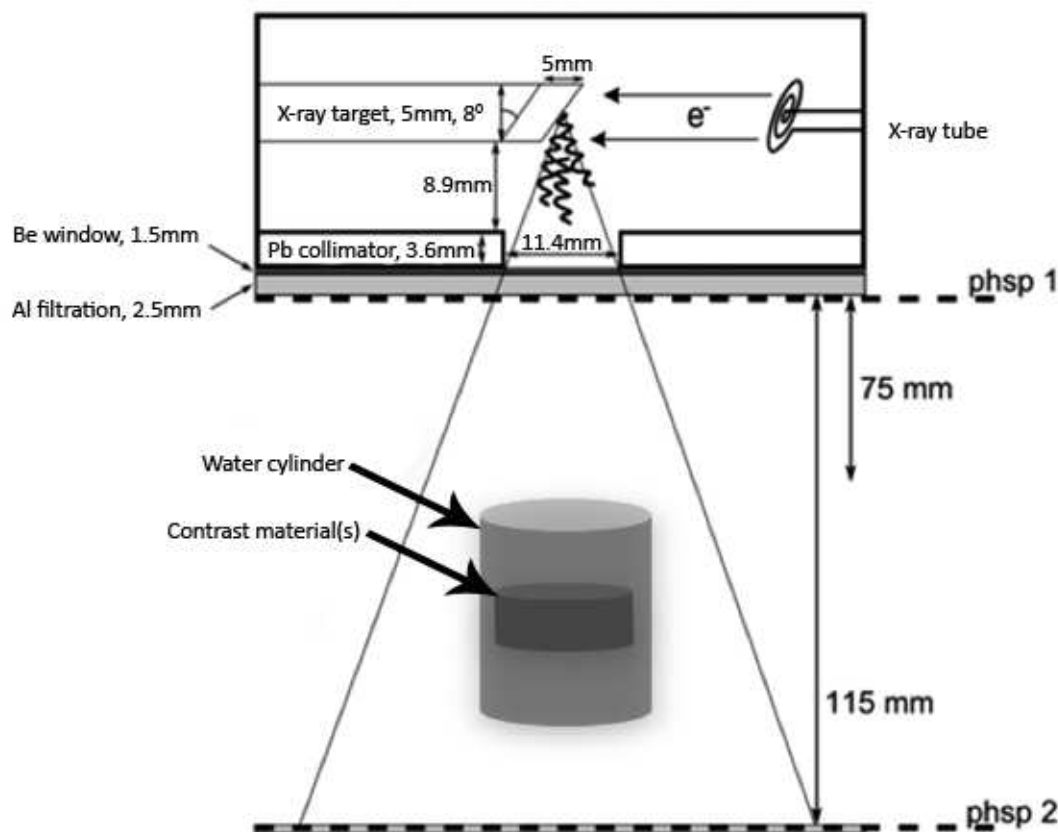
Figure 4.1: *Simulation setup on the BEAMnrc system resembling the geometry of the in-house developed Medipix All Resolution System micro-CT scanner (MARS Bioimaging Ltd, New Zealand) (Butler et al. 2008, Anderson et al. 2010). The phantom was designed to simulate contrast layer(s) embedded within a water cylinder for material decomposition of up to 3 materials.*

matrices containing particles within 1 keV ranges to allow for retrospective formation of energy-selective images (Thing 2010, Thing et al. 2011). The spatial variation in the photon counts was corrected by using an open beam image of 1 keV to 120 keV prior to material decomposition.

4.1.2 BEAM Data Processor

The statistical weights scored on each pixel represents the localised probability of photons being detected. The BEAMnrc package comes with a utility programme

for analysing the phase space file generated in the simulation (Ma & Rogers 2009). Spectral distribution, given in photon fluence/keV/incident particles of the simulated phase space file was derived using BEAM Data Processor (BEAMDP). In our simulations, the number of incident particles is the number of primary histories. The simulated photon counts per pixel can therefore be computed at any given energy upon processing phsp2 using BEAMDP. Spectra obtained from the phsp2 files were normalised against the fluence output from BEAMDP for the conversion of statistical weights into photon fluence.

4.1.3 Thickness estimation

For the given SOD, SSD, object size and the number of primary history in figure 4.1, it was found that the detector pitch of 220 µm achieved an adequate balance between simulated image resolution and spectral SNR for acceptable accuracy in thickness estimation. The pixelated measurements were binned as input to $\boldsymbol{x}$ in (3.5) for estimation of $\boldsymbol{t}$. Material decomposition was performed pixel-by-pixel using the spectrum scored on phsp2 in a 128×128 pixel detector grid. A direct way to find the solution for (3.5) is by mapping a look-up table of counts for an extensive sample of thicknesses. The solution can then be provided by locating the thicknesses that are most consistent with the binned measurements:

$$\boldsymbol{t} = \arg \min_{\boldsymbol{t}} \left\{ \left[\sum_{k=1}^{n} \left(x_k - \lambda_k(\boldsymbol{t}) \right)^2 \times \frac{1}{\lambda_k(\boldsymbol{t})} \right] \times \frac{1}{n} \right\}^{\frac{1}{2}}. \qquad (4.1)$$

The accuracy of the solution given by the look-up table, however, is dependent on the sample size (Alvarez 2011) and a huge set of data points may therefore be required for sufficient accuracy. Alvarez (2011) formulated a maximum likelihood approach by utilising a calibration phantom to approximate the effective attenuation, which is subjective to the selection of regional values and may require a

further error correction computation. In this work, a more direct approach was re-
alised by applying an iterative search algorithm using the MATLAB *fminsearch*
function, which implements the Nelder-Mead algorithm (Lagarias et al. 1998).
This was carried out for both the simulated projection data with and without the
inclusion of scattered radiation in the BEAMnrc model. By using the look-up
table solution as our initial estimates, the MD in (3.5) was minimised without
requiring the likelihood function. Furthermore, the determination of the effective
attenuation over an energy range can be avoided.

In their decomposition, Firsching et al. (2006) employed the mass attenuation
coefficient $\left(\frac{\mu_i}{\rho}\right)$ to reconstruct the areal density $a_i := \rho_i \cdot t_i$ of the materials.
Equivalently, μ_i in (3.2) can be substituted by $\frac{\mu_i}{\rho}$ and a_i (in place of t_i) of the
materials can be determined when the mass attenuation coefficients are chosen as
the basis functions in the proposed method. Likewise, attenuation components
of the photoelectric and the Compton effect contributions together with a total
mass attenuation of a K-edge material can be incorporated for the determination
of basis-material densities along the x-ray path.

4.1.4 Validation of optimal material discrimination

For a constant x-ray tube voltage and current, the theoretical model in chapter 3
provided a solution of choosing energy bins for spectral imaging based on the
smallest confidence region under the influence of Poisson statistics. To reiterate,
a limitation of this model is that it does not take into account scattered radiation.
To achieve optimal spectrum weighted attenuation difference in discriminating
$0.01\,\mathrm{cm}$ of iodine and $1.5\,\mathrm{cm}$ of water, figure 3.5 shows that the optimal bin border
$(E_{(h,1)})$ is at $60\,\mathrm{keV}$. When $E_{(h,1)}$ is fixed at the iodine K-edge of $33\,\mathrm{keV}$, the
optimal higher bin border $(E_{(h,2)})$ was found to be at $51\,\mathrm{keV}$ for the discrimination
of iodine, calcium and water.

Using the BEAMnrc framework, projections for an object consisting of τ_I = 0.01 cm of iodine between two 0.75 cm cylindrical layers of water background (τ_{H_2O} = 1.5 cm) were simulated. The discrimination of more materials using the reconstructed image has been proposed via mass/volume conservation (Liu et al. 2009, Ronaldson et al. 2012) or by segmenting pixels into classes of materials prior to the decomposition (Le & Molloi 2011, Alessio & MacDonald 2013). While, in the projection space, the same may be achieved by assigning up to 4 dimensionality to the linear attenuation coefficients (Bornefalk 2012), we focus on the decomposition of up to 3 materials. The projection data of τ_I = 0.01 cm and τ_{Ca} = 0.22 cm stacked between two 0.75 cm cylindrical layers of water background was simulated. The density for iodine and calcium was defined to be the same as in chapter 3, i.e. 4.93 g cm^{-3} and 1.55 g cm^{-3}, respectively. The precision of material decomposition on the BEAMnrc model was examined by determining the image noise (variance = σ^2), where σ is the standard deviation, given by the averaged difference between the output and its mean value. Mean and variance of the central 690 pixels in the region with contrast material(s) were computed. The simulated variance was computed for bin border energies ranging from 20 keV to 100 keV for the decomposition of two materials and 36 keV to 100 keV for the decomposition of three materials. Bin border energies below 20 keV and above 100 keV were considered suboptimal.

Another important measure for material quantification is the averaged difference between the output and the actual value of thicknesses, known as the bias. The mean square error (MSE) incorporates both the bias and variance. The following FOM was therefore formulated as a validation of optimal material discrimination against the theoretical model:

$$\text{FOM} = \left(\sum_{i=1}^{m} MSE_i/\tau_i^2 \right)^{-\frac{1}{2}}. \tag{4.2}$$

(4.2) was evaluated for bin border energies ($E_{(h,1)}$) from $20\,\text{keV}$ to $100\,\text{keV}$ for
the decomposition of iodine and water. For the decomposition of 3 materials, the
lower bin border energy ($E_{(h,1)}$) was held at the K-edge of iodine ($33\,\text{keV}$), while
a FOM curve was plotted the upper bin border energies ($E_{(h,2)}$) ranging from
$36\,\text{keV}$ to $100\,\text{keV}$ for the higher energy bin.

4.2   Results

4.2.1   BEAMnrc simulations

The $120\,\text{keV}$ monoenergetic electrons incident on the x-ray anode described in
section 4.1.1 produced approximately 1.20×10^8 photons per exposure. The open
beam spectrum on the detector plane was used for the aforementioned normal-
isation of incident counts in the optimisation algorithm and the conversion of
statistical weights into photon fluence. Figure 4.2 demonstrated negligible differ-
ences against Tucker, Barnes & Chakraborty's (1991) model generated by Spec-
gen (Glenn Stirling, National Radiation Laboratory, Christchurch, New Zealand).
The uncertainty of the simulation given by BEAMDP was plotted as error bars
on the spectrum. A comparison of Specgen with other packages such as xcomp5r
and TASMIP can be found in Meyer et al. (2004). A representative set of pro-
jection images in figure 4.3a shows two concentric circular regions. The darker
inner region (i) shows the pixels with higher attenuation due to the contrast ma-
terial(s) within the water cylinder and the outer mid-gray region (ii) represents
the water region without contrast material. While decomposition was performed
on the full-field projections, only the ROI with the overlapping contrast materials
(region i) was analysed.
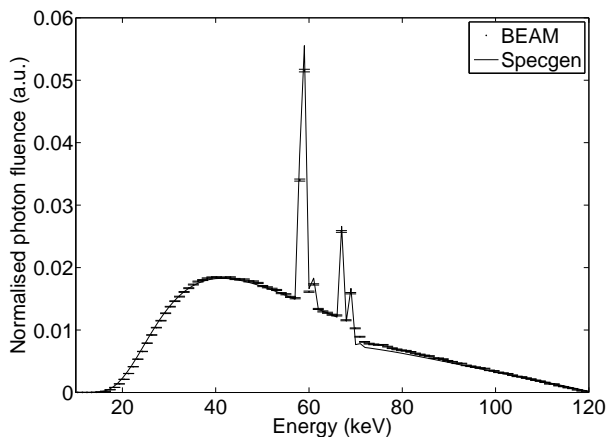
Figure 4.2: *Comparison of the simulated incident energy spectrum with a reference spectrum from Specgen (Glenn Stirling, National Radiation Laboratory, Christchurch, New Zealand) obtained using Tucker, Barnes & Chakraborty's (1991) model of W/Rh target shows negligible difference.*

4.2.2 Validation of optimal material discrimination

The top row of figure 4.4 shows a representative set of the decomposed material basis projection images, with their respective profiles through the middle horizontal axis plotted in the bottom row of figure 4.4. Decomposition was carried out using (4.1). The profiles were normalised with respect to τ_i, which produced values around unity in the presence of materials, demonstrating the accuracy of the decomposition. A more quantitative measurement of the decomposition's precision and accuracy is summarised in figure 4.5 and figure 4.6. The solid line represents the mean thickness over the 690 pixels within region (ii) in figure 4.3a, whereas the error bars show the standard deviation (σ) for the decomposition using a particular bin border energy. The reference thicknesses (τ_i) was plotted with dotted lines to provide an indication on the bias of the decomposition.

The variance (σ^2) and the MSE are tabulated in table 4.1 to show the consistency with the estimated image noise given by the theoretical algorithm described in section 3.1.3. Specifically, the theoretical variance (variance$_{A_i}$), the simulated
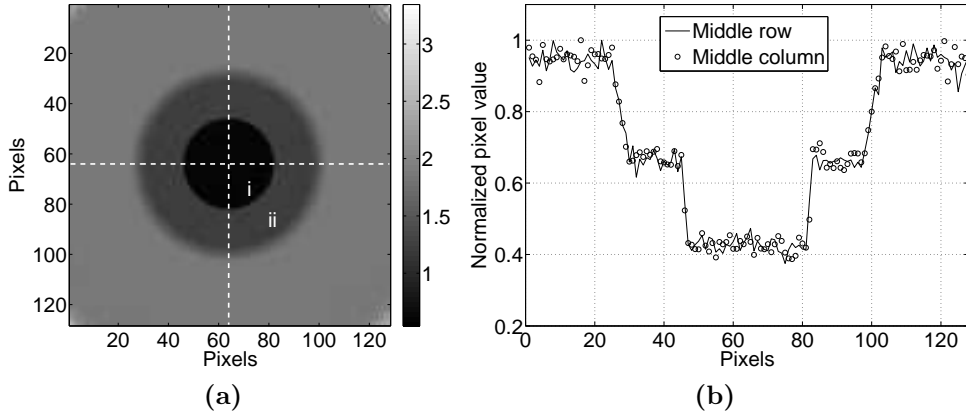
Figure 4.3: A representative (a) projection image and (b) the profiles upon correction using the open beam data. Colorbar in (a) indicates arbitrary unit upon normalisation. The inner (region i) and outer (region ii) concentric circular regions are the ROIs with and without contrast material(s) within the water cylinder, respectively. Statistical analysis was performed on the pixels within the inner region. The profile across the horizontal axis is relatively constant and is plotted in (b) using a solid line as a reference for the corrected middle column profile (circles).

variance (variance$_{B_i}$) and the MSE were averaged over the 5 keV around the theoretical optimal bin border energy, i.e. optimal $E_{(h,1)} \pm 2$ keV and optimal $E_{(h,2)} \pm 2$ keV for the decomposition of two and three materials, respectively. The minimal bias around the optimal bin border was reflected in the similar MSE and variance values for the decomposition of two materials. Note that some bin border energy, e.g. 28 keV for the decomposition of iodine/water in figure 4.5, provided inaccurate material thicknesses.

For the case of three materials (figure 4.6), a higher MSE compared to the variance, particularly for the calcium image, was obtained with the inclusion of scattered radiation. This can be seen in the deviation of the solid line from τ_{Ca} (dotted line) in figure 4.6b. Figure 4.7b shows a considerable reduction in the bias of thickness estimation for calcium upon rejection of scattered radiation. Variance$_{B_i}$, MSE and bias for the decomposition of 3 materials prior to and upon scatter rejection can also be found in table 4.1. Figure 4.8 and figure 4.9 show
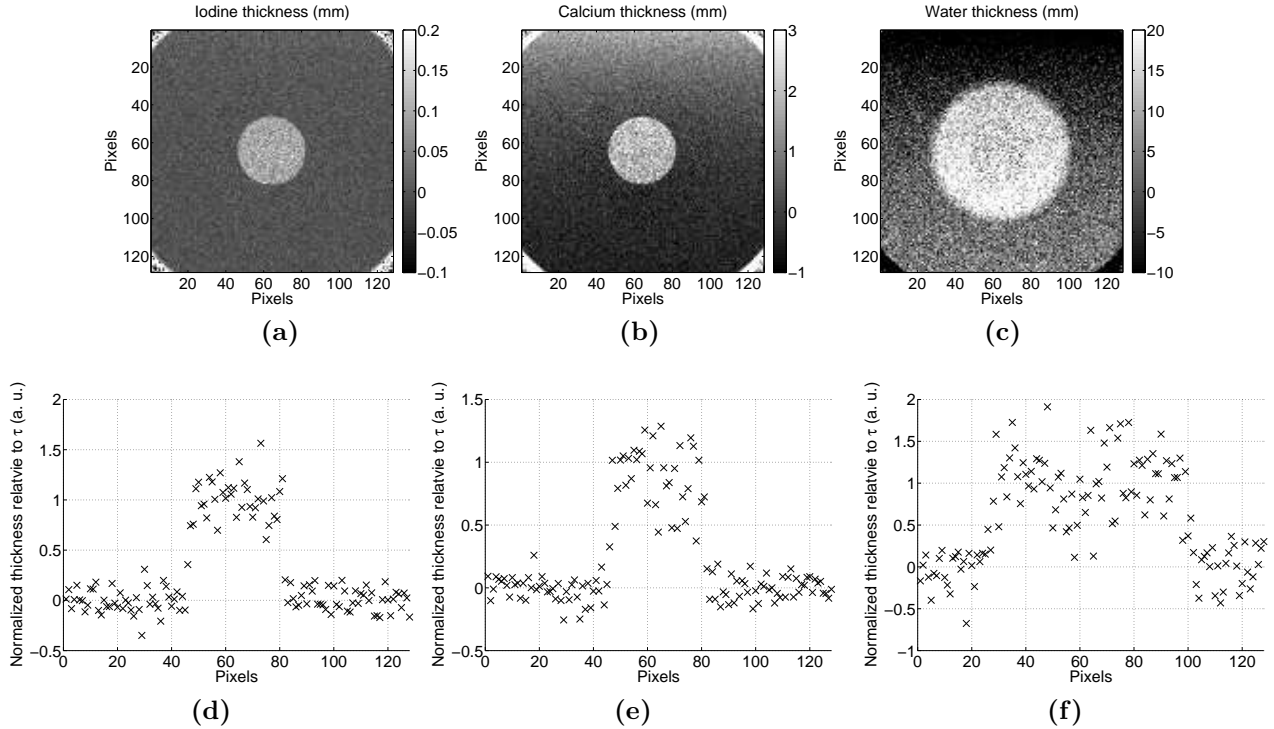
Figure 4.4: The decomposed material basis of (a) iodine, (b) calcium and (c) water. The respective profiles (d - f) through the middle row of pixels were normalised to τ_i to illustrate the accuracy of the estimations. A more quantitative analysis of the accuracy as well as the precision can be found in figure 4.8, figure 4.9 and table 4.1.

a comparison variance$_{B_i}$ to variance$_{A_i}$ for the decomposition of two and three materials, respectively. The minimisation of the combined σ^2 in the decomposition leads to the optimisation of energy bins. The predicted image noise from figure 3.9 and figure 3.10 were reproduced using dotted lines to compare with the simulated variances (solid lines).

The FOM curves based on (4.2) obtained using the BEAMnrc model largely agree with the ones obtained from the optimisation algorithm. Figure 4.10 shows the highest FOM value given by the BEAMnrc model is $2\,\mathrm{keV}$ lower than the theoretical optimum at $60\,\mathrm{keV}$ for the decomposition of $0.01\,\mathrm{cm}$ iodine and $1.5\,\mathrm{cm}$ water. Similarly, the highest FOM value obtained for the the BEAMnrc models

Figure 4.5: Mean and standard deviation obtained for the material basis images
for (a) iodine and (b) water, displayed at an interval of $2\,\mathrm{keV}$. The calculation of
these error bars allows the quantification of image noise and comparison with the
theoretical prediction (figure 4.8), which leads to validation the optimisation of bin
border energy based on our FOM. Optimal bin border energies are indicated by
the smallest error bars. The average bias over $5\,\mathrm{keV}$ around the optimal bin border
is 1.24% for (a) and 6.06% for (b).

Table 4.1: A summary of mean square error (MSE), variance and bias obtained
using the theoretical (subscript A) and BEAMnrc (subscript B) models.

		Materials		
		I (0.01 cm)	H$_2$O (1.5 cm)	Ca (0.22 cm)
2 materials (2 bins)	variance$_A$(cm^2)	6.71×10^{-6}	2.62×10^{-1}	-
	variance$_B$(cm^2)	9.78×10^{-6}	4.25×10^{-1}	-
	MSE (cm^2)	9.78×10^{-6}	4.33×10^{-1}	-
3 materials	variance$_A$(cm^2)	6.11×10^{-6}	2.67×10^{-1}	3.04×10^{-3}
	variance$_B$(cm^2)	4.82×10^{-6}	3.33×10^{-1}	2.02×10^{-3}
	MSE (cm^2)	4.95×10^{-6}	3.33×10^{-1}	2.61×10^{-3}
	Bias (%)	3.88	0.91	11.14
3 materials (Scatter rejected)	variance$_B$(cm^2)	5.25×10^{-6}	3.47×10^{-1}	2.31×10^{-3}
	MSE (cm^2)	5.27×10^{-6}	3.47×10^{-1}	2.31×10^{-3}
	Bias (%)	1.67	1.22	0.21

was located at $49\,\mathrm{keV}$ compared to $51\,\mathrm{keV}$ for the theoretical optimum. The FOM
for $\pm2\,\mathrm{keV}$ around the theoretical optimum was observed to be $>96\%$ of the peak
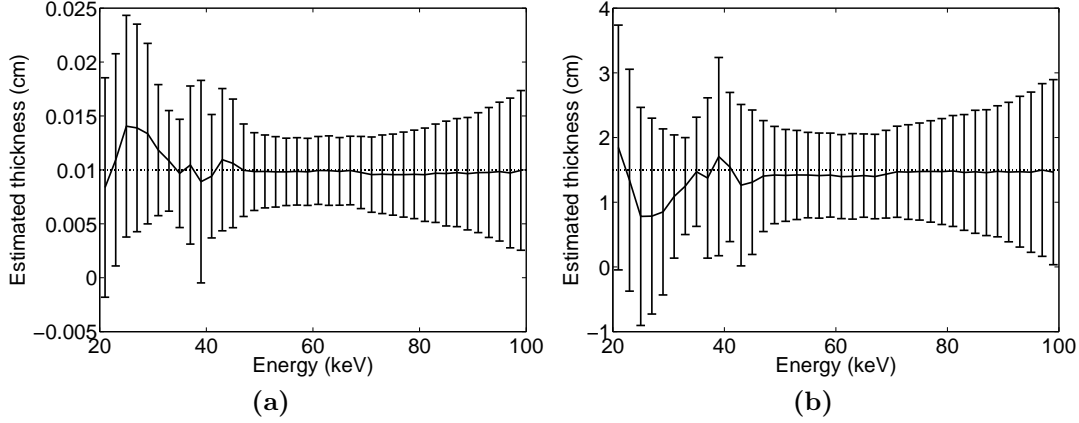value for the BEAMnrc model in both cases.
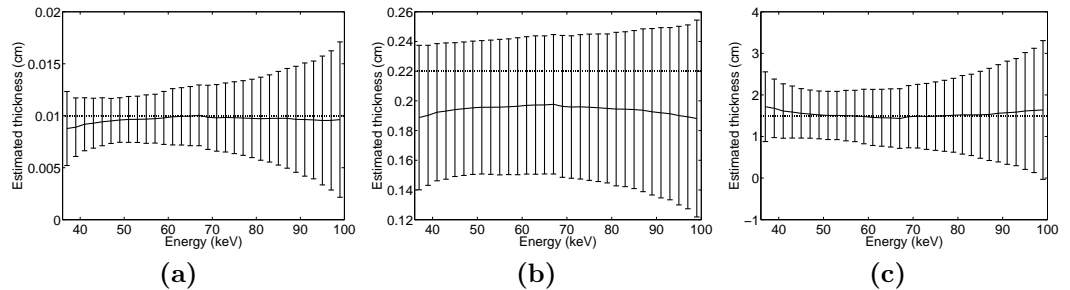
Figure 4.6: Mean and standard deviation obtained for the material basis images for (a) iodine (b) calcium and (c) water, displayed at an interval of 2 keVs. A comparison with the image noise predicted by the theoretical model is shown in figure 4.9. The average bias over 5 keV around the optimal bin border is 3.88% for (a), 11.14% for (b) and 0.91% for (c). The improvement on the bias upon the rejection of scattered radiation is shown in figure 4.7.
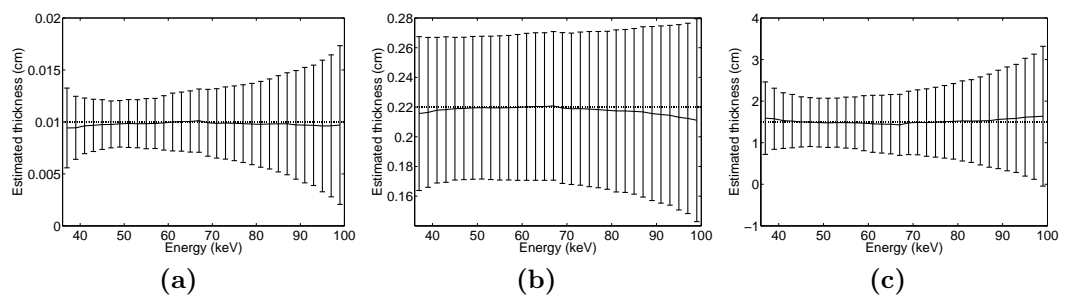
Figure 4.7: Mean and standard deviation obtained for the material basis images for (a) iodine (b) calcium and (c) water with only the primary photon included. Rejection of scattered radiation improved the accuracy of material quantification, particularly in (b) (c.f. figure 4.6b).

4.3 Discussion

BEAMnrc simulations allow for the optimisation of material discrimination to be validated in an idealised environment. No imperfections other than the scattered radiation have been taken into account in the simulations and an ideal detection quantum efficiency of the detector was assumed. As shown, optimisation of energy bins can provide better confidence in material thickness estimation. Some energy bins may even provide inaccurate material estimates (see figure 4.5).
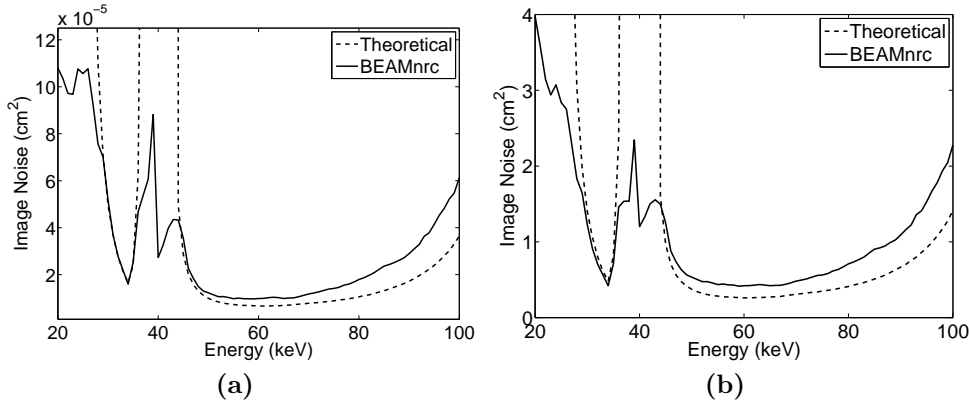
Figure 4.8: Image noise of the material basis images for (a) iodine and (b) water. σ^2 values from figure 3.9 were repeated using dotted lines to show the consistency with the theoretical predictions. Similar to figure 3.9, the theoretical values were allowed to extend beyond the vertical axis to focus on the lowest of σ^2 values. A minimisation of these values leads to the maximisation of FOM and thus the optimisation of energy bins.

While it can be intuitive to place a energy threshold at the K-edge of imaging material, there may be a more optimal energy as shown in figure 4.10a due to better counting statistics. For non K-edge imaging, the optimisation is particularly crucial to provide an optimal photon binning scheme. Furthermore, some contrast agent with higher atomic number and higher K-edge energy and may not be optimal for achieving a balance between contrast and counts. Given the achievable energy resolutions of the current PCDs (Shikhaliev 2006, Ballabriga et al. 2011a, Schlomka et al. 2008), we reason that the optimisation algorithm provides a sufficient guideline for the location of energy bins when implemented for material discrimination using spectral x-ray imaging.

Upon comparing with the simulated variance, the theoretical prediction of image noise presented some limitations. The simulated σ^2 incorporated both image noise sources from the projection and the open beam image. The normalisation of the spatial variation in photon counts in section 4.1.1, which was primarily due to the heel effect, introduced a further photon counting noise inherent to the open

70
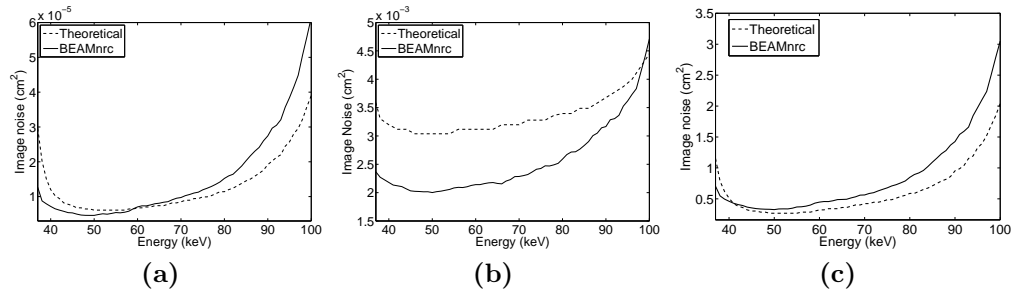
Figure 4.9: Image noise of the material basis images for (a) iodine, (b) calcium and (c) water. Discrepancy in (b) was due to the memory limit in Matlab, which resulted in a step-wise function for the theoretical prediction of calcium image noise.

beam image. The heel effect resulted in reduced x-ray intensity on the anode side of the image, caused by the x-ray absorption by the anode target, and must be normalised for accurate decomposition. Software limitation also prohibited more accurate resemblance between predicted and simulated variances for the decomposition of three materials, particularly for calcium (figure 4.9b), as discussed in section 3.4. Regarding figure 4.8, the confidence region in the theoretical model can expand infinitely when the statistics for a bin border energy is poor. The predicted image noise (dashed curves) hence extended further than the axis, while the simulated image noise has a finite range.

For the decomposition of two materials, the agreement between the predicted and simulated σ^2 values were achieved within the limit on the largest possible matrix size in Matlab. The theoretical model was therefore applied to estimate the photon counts required to confidently decompose a small amount of calcification within breast tissue, which will be presented in section 4.3.1, in order to compare with the optimisation of dual-energy mammography (Johns & Yaffe 1985).

With regard to the precision and accuracy of material decomposition, Alvarez (2011) demonstrated that his proposed maximum likelihood estimator achieved the CRLB. Our MSE is shown to be dominated by the variances, indicating
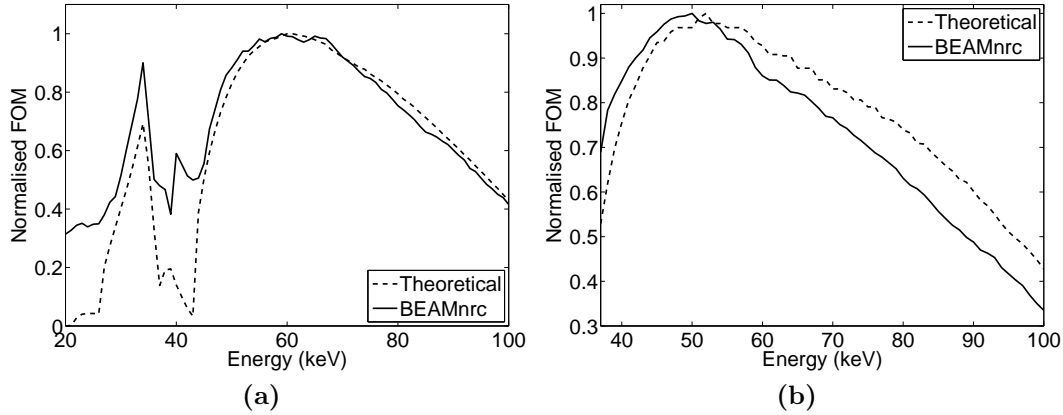
Figure 4.10: Consistencies between the simulated and the theoretical optimal
bin border energies. (a) In particular, the highest FOM value obtained with the
BEAMnrc model differs by 2 keV from the theoretical optimum of 60 keV for the
decomposition of iodine and water. (b) Likewise, for the decomposition of three
materials, optimal $E_{(h,2)}$ was located at 51 keV and 49 keV for the theoretical and
the BEAMnrc simulation, respectively.

that our estimator is unbiased. It should be emphasised that, for computational
efficiency and hardware limitations, the simulations were performed below the
typical clinical settings of standard x-ray photon flux rates. Simulated detected
counts were less than 900 per pixels for all cases. The random nature of the simu-
lated detected spectrum when compared to the expected photon counts provided
by the theoretical model is depicted in figure 4.11.

Although the BEAMnrc was setup in this work to enable separate simulations
of the x-ray tube and transmission through the imaging object, the generation of
x-rays was largely inefficient, particularly for tube voltages comparatively lower
than 120 kVp. Only the tungsten spectrum of 120 kVp was simulated in this work,
as a result. Furthermore, the in-house Matlab code to translate phsp information
into projection image increase proportionally to the number of incident particles.
The pixel size on the detector plane (phsp2) was set to be four times that of
the Medipix detector (220 µm) to partially compensate for the limitations. It

is expected that increasing the number of detected counts can facilitate noise reduction in the simulated spectrum (solid curve) in figure 4.11 and thereby provide improved agreements between variance$_{A_i}$ and variance$_{B_i}$ in table 4.1. As such, spectra of smaller pixel pitches can be simulated too.
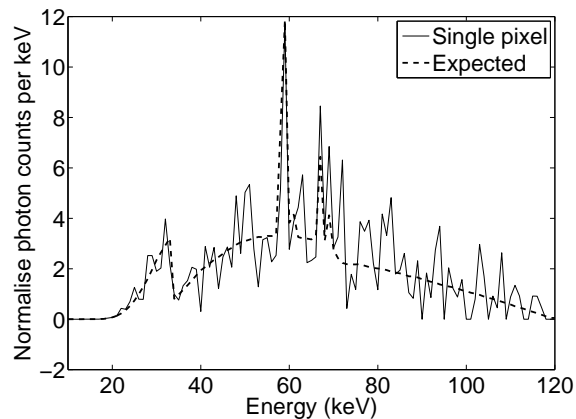
Figure 4.11: *An example of the detected spectrum incident on a 220 µm pixel generated using BEAMDP. Although it shows a similar trend as the expected spectrum given by the Beer-Lambert equation, the noisy spectrum for a particular pixel within the overlapping region may also contribute to the discrepancy of variance estimations between the BEAMnrc and the theoretical models.*

The scatter contribution between 10 keV and 60 keV for the three material decomposition was 25%, which contributed to the 11% bias in calcium thickness estimation in table 4.1. The quantification and rejection of scattered radiation was enabled by the ability for particle interaction tracking in the BEAMnrc simulation (Rogers et al. 2004). While the rejection of scattered radiation lowered the bias in the decomposition, the reduction in simulated detected photon counts resulted in a marginally higher image noise in the decomposition of three materials (see table 4.1). The 10% scattered radiation between 10 keV and 60 keV for the decomposition of iodine and water does not result in a considerable bias in thickness estimation (variance ≈ MSE) and was thus ignored. Note that practical implementation of scatter rejection, such as a multi-slit collimators have been

implemented by other groups (Ding & Molloi 2012, Shikhaliev 2008*a*). Another
future applications is therefore scatter correction utilising the particle tracking
(LATCH) function in BEAMnrc for material decomposition, which may help
reducing the impact of scattered radiation in spectral x-ray imaging (Wiegert
et al. 2009).

4.3.1 Dose comparisons with dual-energy mammography

To relate image quality to patient dose in dual-energy mammography, a theory
was presented to determine the ideal monoenergetic exposures (Johns & Yaffe
1985). In their analysis, they aimed at achieving a SNR of 5 in the detection of
calcification with the removal of breast tissue contrast. As reported by Johns &
Yaffe (1985), a SNR of 5 can be obtained for the detection of 0.02 cm calcification
within a 4.2 cm breast with a dose of 4.2 mGy. This was achieved using an ideal
pair of theoretical monoenergtic beams at 19 keV and 68 keV. By smoothing the
high energy image prior to the removal of breast tissue contrast, it was noted that
the dose can be reduced to 1.6 mGy with SNR = 5. In a follow-up experiment
of dual-energy mammography (Johns et al. 1985), however, the optimal dose was
affected by the implementation of a polychromatic beam, as well as by the use of
a non-mammographic digital scanning system.

Given a tungsten spectrum of a Source-Ray (Source-Ray Inc, Ronkonkoma,
NY, USA) x-ray tube available at the University of Canterbury, a 0.02 cm calci-
fication was decomposed from within 4.2 cm of breast tissue using our method of
decomposition in chapter 4.1.3. The mean glandular dose (MGD) for achieving
a SNR $\geq$ 5 in the decomposed calcification image was estimated to be 1.67 mGy
for the polychromatic spectrum. This can be achieved using a 50 kVp tube volt-
age, an ideal 1 mm CdTe sensor layer and the recommended pixel size of 85 μm
(Bushberg et al. 2003). The optimal bin border energy was optimised using our

theoretical model in chapter 3 to be 29 keV for this configuration.

Similarly, the optimal MGD was computed for the minimum operating voltage of the tube at 35kVp to be 3.65 mGy, with an optimal bin border energy of 26 keV. MGD was determined to be comparatively higher for the silicon sensor layer commonly found in the Medipix detector (Llopart et al. 2002, Doesburg et al. 2012), due to the lower absorption probability of the material (Aamir et al. 2011a). Details on the optimisations of spectral mammography can be found in Appendix A. A means of converting photon counts to MGD is presented in section A.1.

4.4   Concluding remarks

A model for simulating spectral x-ray projection was setup using the BEAMnrc code system. The uniform object in the simulations was conveniently designed to enable the calculation of image noise. The decomposition method provides negligible bias in thickness estimation, which is demonstrated in the similar values for MSE and variance for the decomposition of two materials. For the case of three materials, the particle interaction tracking (LATCH) function in the BEAMnrc framework was applied to investigate the effect of scattered radiation on material thickness estimation. The bias in one particular material basis image was increased considerably with the inclusion of scattered photons in the simulated spectrum.

However, scattered radiation was shown to only minimally affect the optimal bin borders and the optimisation of photon counts per pixel. A thorough analysis on the simulated noise was performed and compared with the theoretical prediction to provide a validation of the optimisation algorithm without the technical complications of PCD. The theoretical prediction of optimal energy bin borders

was accurate to within $2\,\mathrm{keV}$ for the decomposition of $0.01\,\mathrm{cm}$ of iodine within $1.5\,\mathrm{cm}$ of water when compared to the BEAMnrc model. The FOM for bin border energies of $\pm 2\,\mathrm{keV}$ around the theoretical peak were at least 96% of the optimum FOM value. Similar results were obtained for the 3-material decomposition of $0.01\,\mathrm{cm}$ of iodine and $0.22\,\mathrm{cm}$ of calcium with $1.5\,\mathrm{cm}$ of water background.

The image noise prediction for the decomposition of three materials was impeded by the largest possible matrix size allowed in Matlab, as discussed in section 3.4. However, the theoretical and simulated image noise demonstrated excellent agreements for the decomposition of two materials. This leads us to a prediction of mean glandular dose required to effectively quantify a calcified feature within a breast. The dose required to achieve a SNR of ≥ 5 in the decomposition of calcification using spectral imaging was estimated to be similar to that of using two monoenergetic beams in dual-energy mammography.

Chapter 5

Experimental and development work on the MARS spectral CT scanner

The initial aim of this chapter was to report on the experimental verification of the work in the previous chapters. However, due to technical difficulties with the imaging hardware, the focus was shifted to further develop the MARS imaging system, as well as experimental measurements with the Medipix detector.

This chapter provides an overview of the MARS-CT scanner. The technical details of the Medipix detectors will be introduced and the distinctions between the Medipix2 and the Medipix3 ranges of detectors will be summarised. The system development and the experimental work the candidate was involved in will be presented. The initially proposed experiments for the verification of the theoretical model will be discussed.

Due to unavoidable manufacturing variations, pixels across a Medipix detector respond unequally when exposed to a homogenous x-ray flux. The dispersion (standard deviation) of the Gaussian response function for a Medipix2MXR de-

tector may be as wide as $2.65\,\mathrm{keV}$ and can be optimised to be less than $1\,\mathrm{keV}$ (Procz et al. 2009). To reduce the inhomogeneities in the Medipix2MXR, the candidate was largely responsible for the implementation of a Matlab software within the research group. Upon acquisition, normalisations using open beam images and corrections of detector defects (e.g. unresponsive pixels) were required to reduce artefacts prior to image reconstruction. The image processing method to which the candidate has contributed will be presented. Specifically, the candidate improved the identification of malfunctioning pixels and sped up the entire process considerably.

The Medipix3 features the CSM with inter-pixel communication logic to improve spectroscopic performance (Ballabriga et al. 2011a). The spectrum of a comparatively intense americium gamma source was measured in this work to examine the CSM. While the data analysis was performed by another team member, the candidate presented the results at the *14th International Workshop on Radiation Imaging Detectors (iWoRID 2012)* and personally prepared the corresponding article for publication in the conference proceedings (Doesburg et al. 2012). Furthermore, the candidate has made a considerable contribution towards enabling the spectroscopic mode of acquisition, as well as the preparation of another article on the topic (Walsh et al. 2013) for submission to the same journal.

5.1 Medipix All Resolution System

The MARS project is a research team consists of more than 20 members based at the University of Canterbury and the University of Otago in Christchurch, New Zealand. The MARS research team is administered by a spin-off company[1],

---

[1] http://www.marsbioimaging.com

to construct a spectral CT scanning system based on the Medipix detector (figure 5.1a). While the MARS group receives the detector from the Medipix consortium[1], local developments include the manufacturing of readout electronics, called the MARS camera, and the CT gantry. A MARS camera consists of the Medipix assembly and locally produced readout electronics, mounted within a fan-cooled container. The components of a MARS camera are displayed in figure 5.1b. The custom built *libMars* C library and Python interface offer communication with the Medipix chip through a Gigabit Ethernet cable and allow for stand-alone operation of the MARS camera.

The MARS-CT is comprised of the MARS camera and an x-ray tube, rotating around a translatable specimen holder. The MARS-CT gantry features independent translation of the camera and the x-ray tube for adjustable magnification. A single Medipix detector has an imaging area of $14.02 \times 14.02 \, \text{mm}^2$. Using a multi-chip carrier, a MARS camera can be installed with up to 6 Medipix chips. A maximum field of view (FOV) of $10 \, \text{cm}$ at each projection angle is enabled by translating the camera, and subsequent tiling of the images in the image processing software. CT images of human specimen and laboratory animals captured using the MARS camera have been demonstrated in e.g. Walsh et al. (2011a) and Ronaldson et al. (2011).

5.2 Technical details of the Medipix detectors

A complete Medipix detector consists of a semiconductor sensor layer and an underlying ASIC, with the two layers connected by conducting bump-bonds (see figure 5.2a). Silicon (Si), gallium-arsenide (GaAs) and cadmium-telluride (CdTe) sensor layers are currently available for the Medipix detectors, while cadmium

---

[1] http://medipix.web.cern.ch/MEDIPIX/
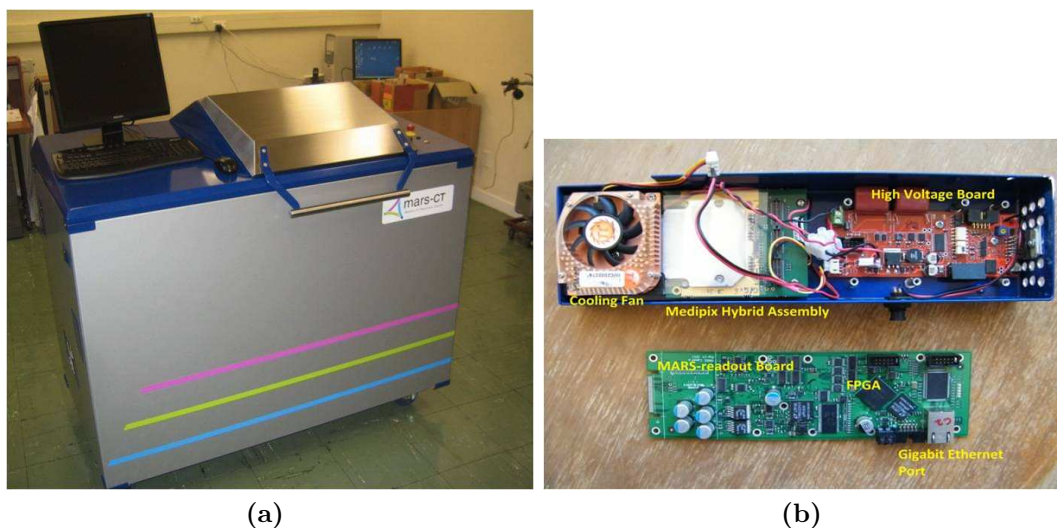
Figure 5.1: *(a) The MARS-CT system is equipped with (b) the MARS camera and an x-ray tube within a lead shielded container. (b) Components of a MARS camera include a Medipix assembly and the readout electronics. MARS camera allows for independent operation via the locally developed* libMars *C library and Python interface.*

zinc telluride (CdZnTe or CZT) is generally considered as another auspicious candidate sensor layer material (Overdick et al. 2009, Bornefalk & Danielsson 2010). As mentioned in section 2.5, a photon detection event is converted into an electronic pulse in the semiconductor sensor layer in a PCD and the pulse height is dictated by the photon energy. In a Si sensor layer, a 36 keV photon, for example, creates 10,000 electron-hole pairs, since 1 electron-hole pair is generated for every 3.6 eV of photon energy absorbed by the Si sensor. For a common Si Medipix detector, a bias voltage of 100 V is applied across the 300 μm of Si sensor layer by a couple of conducting electrodes to create a depletion zone free of charge. Under the influence of the electric field, the positively charged holes drift to the ASIC end of the field and induce a pulse in the electrode, as illustrated in figure 5.2b. The pulse contains energy information regarding the photon and is subsequently processed by the ASIC. A higher bias voltage is commonly applied for thicker materials and different semiconductors may require an opposite polarity. CdTe

is more efficient in carrying electrons and an opposite bias to that for Si and
GaAs is applied. As an x-ray detection layer, CdTe and GaAs have comparably
higher absorption efficiencies for the detection of a broader x-ray spectrum (Aamir
et al. 2011a) and are therefore materials of interest for Medipix. However, the
Si sensor layer comes with several industrial advantages (Bornefalk & Danielsson
2010), including being relatively low-cost and easier to be manufactured. A study
by our group has shown prominent wrinkle patterns and inhomogeneous detector
regions in a CdTe sensor layer (Aamir et al. 2011a). The availability of GaAs
Medipix detectors is relatively sparse in the MARS group but a study using a
GaAs Medipix3 detector is underway during the write-up of the thesis.

(a)   (b)
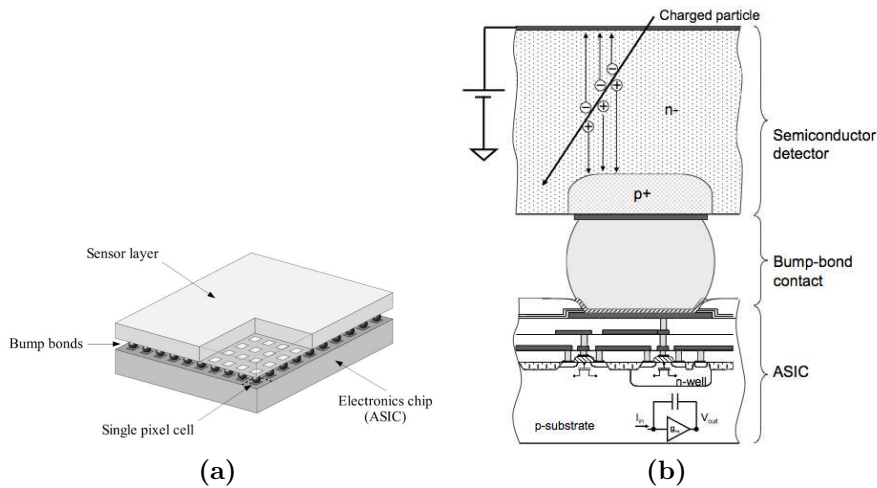
Figure 5.2: *(a) A schematic of the Medipix detector (Pfeiffer 2004) and (b) the
side view of a pixel (Ballabriga 2009) showing the semiconductor sensor layer and
the ASIC. Different semiconductor materials can be bump-bonded to the electronic
chip to act as an x-ray detection layer. When a photon is detected, an electron
and hole pair is created, as shown in (b). The applied bias voltage drifts one of the
charge clouds to the ASIC end of the sensor layer. The polarity and the voltage
of the applied bias are dependent on the type and thickness of the semiconductor,
respectively. A silicon sensor layer is assumed in (b). Drawings are not to scale.*

Since the second version of the Medipix design, the Medipix2, the ASIC has
been capable of handling negative and positive pulses induced by different semi-

conductor materials. The energy sensitivity of the Medipix detectors originates from the discriminator placed before the counting circuitry. The "front-end circuitry" in the ASIC is responsible for transforming every incoming signal into a smooth curve to be compatible with the discriminator. The discriminator serves as a voltage comparator, which is triggered only when the pulse height exceeds a tunable threshold. Finally, triggering the discriminator causes the digital counter to be incremented and the photon counting process is concluded. The dynamic range in the Medipix detectors is defined by the counter size. In addition to a larger dynamic range, the Medipix2MXR also includes an overflow control (Tlustos et al. 2006). The MXR can record up to a maximum of 11,810 pulses per pixel. The photon count saturates at this value with any further incoming photons ignored (c.f. 8001 counts with Medipix2 without saturation control). With the MARS camera, the counter size of the Medipix3 is programmed to be 4095 (12-bit counter).

The subsections below present some specific technicalities with regard to the discriminators of the two Medipix detectors. However, the full operation of the Medipix2MXR and the Medipix3 are controlled by 13 and 25 global Digital to Analogue Converters (DACs), respectively. A comprehensive description of detectors and the DACs can be found in the respective user manuals, as well as in the theses of the corresponding developers, Llopart (2007) and Ballabriga (2009). DAC values recommended by the developers were generally employed in the MARS camera. A summary of the DAC functionalities and their nominal values have been provided in the published theses within the MARS research team (see e.g. Doesburg (2012) and Ronaldson (2012)).

5.2.1 Medipix2

The dual discriminators in Medipix2MXR allow for energy windowing during acquisition. The discriminator thresholds are controlled by two offset currents, the THL and THH DACs, which in turns control the threshold voltages $V_{th}Low$ and $V_{th}High$ in figure 5.3, respectively. Due to a manufacturing defect, imaging performance degraded when the windowed mode was enabled. Experiments were conducted with setting THH to its highest possible value to deactivate the energy window mode (Aamir et al. 2011a, Aamir et al. 2011b). When measurements of multiple thresholds were required, THL was varied with several values, as described in Firsching et al. (2009) and Anderson et al. (2010). Calibration of DAC values to photon energy in keV can be established and has been performed within our group by means of measuring fluorescence peaks of metallic foils (Ronaldson et al. 2011). Furthermore, fabrication variations in the electronics and the sensor layer caused pixel-to-pixel inhomogeneities in the discriminator threshold. The resulting offset is sufficiently large to, for examples, randomly vary the discriminator's response to a homogeneous flux across the chip, and to reduce the accuracy of the energy calibration of the threshold value. An algorithm to minimise the dispersion in the THL sensitivity using the 3-bit adjustment DAC depicted in figure 5.3 will be described in the next section.

5.2.2 Medipix3

The SPM of the Medipix3 features dual thresholds that differ from those in the MXR. In the Medipix3, the two discriminators are associated with two counters, providing two pulse height analysers per pixel. The discriminators are controlled by the Threshold0 and Threshold1 DACs, which are represented by *THA* and *THB* in figure 5.4, respectively. As introduced in section 2.5.1, bump-bonding the Medipix3 at a 110 μm pixel pitch combines eight discriminators from four
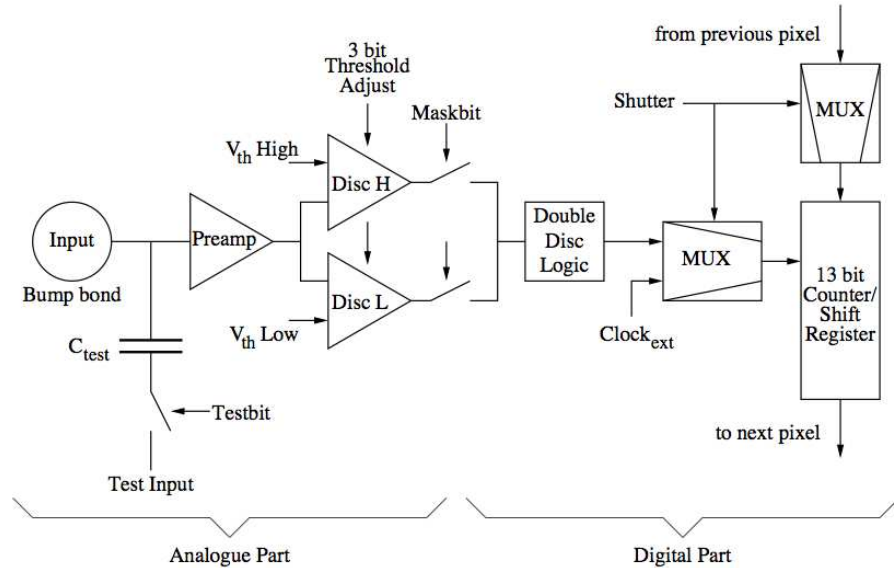
Figure 5.3: *Block diagram of the Medipix2 pixel electronics (Pfeiffer 2004) to show the low ($V_{th}Low$) and high ($V_{th}High$) threshold voltages, which are controlled by the THL and THH DACs, respectively. The 3-bit adjustment DAC designed to minimise the dispersion of the THL sensitivity (see section 5.3) is also represented. The digital part of the circuitry is responsible of counting the individual induced pulses.*

adjacent ASIC pixels. Electronically, the spectroscopic mode is activated by enabling the ColorMode bit in the operation mode register (OMR) of the Medipix3 (Ballabriga 2009). The Threshold0...7 DACs control the threshold value of the eight discriminators. At the time of writing, devices bump-bonded specifically for the spectroscopic mode are not yet available to the MARS group. However, partial spectroscopic mode was still enabled using a MARS camera with pixels bump-bonded at 55 μm pixel pitch, which will be presented in section 5.6.

The SPM often suffers from degraded spectroscopic performance, due to a phenomenon known as the charge sharing effect. Electrons or holes generated in the sensor layer are likely to be scattered as they travel towards the electrodes. Pulses may be induced in more than one pixel as the initial charge cloud diffuses into a broader area. The neighbouring pixels inadvertently detect independent

apparent photons of lower energies. When prompted by the EnablePixelCom bit in the OMR, the CSM of the Medipix3 has the ability to communicate among four abutting pixels. Given the diffused signals, the summing nodes located at the edge of the four pixels can reconstruct the initial pulse height. The arbitration circuitry shown in figure 5.4 allocates the combined signal as a single photon count to the pixel with the largest portion of the distributed charge, according to the 'winner takes all' scheme in figure 2.7b. Section 5.5 examines the CSM performance of a 1 mm CdTe Medipix3 (Doesburg et al. 2012).

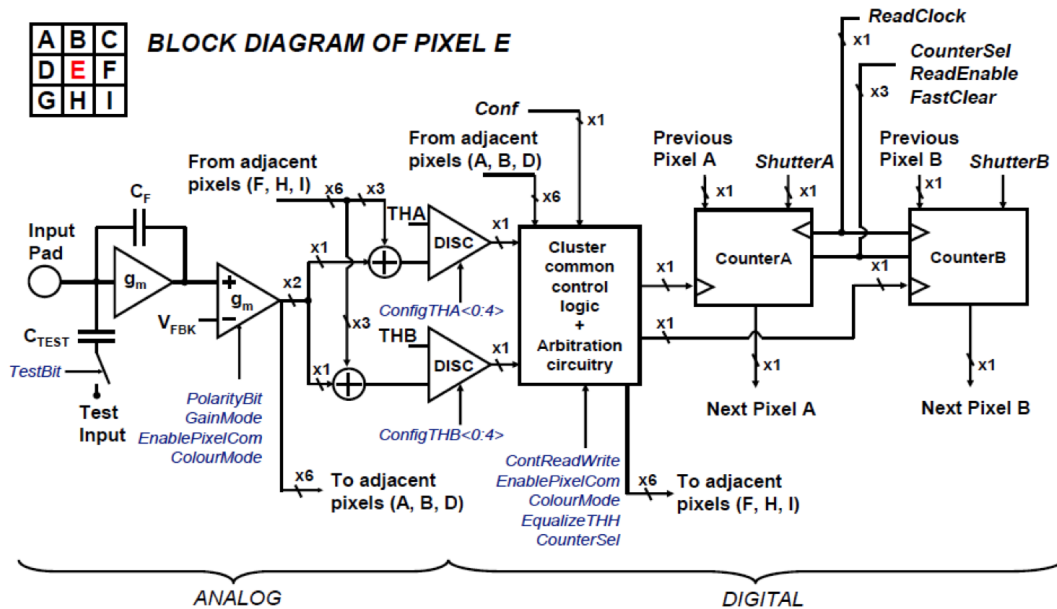**Figure 5.4:** *Block diagram of the Medipix3 pixel electronics (Ballabriga 2009) to indicate the threshold levels THA and THB, which correspond to the Threshold0 and Threshold1 DACs, respectively. The ColorMode bit in the OMR triggers the CSM of operation (see section 5.5), which requires the arbitration circuitry for charge allocation, while the spectroscopic mode (see section 5.6) can be enabled by the ColorMode bit.*

5.3   Implementation of pixel equalisation in Medipix2

For an acceptable imaging quality, it is necessary to minimise the inconsistency between pixels in the discriminator's response to the same pulse height. A 3-bit adjustment DAC is supplied in each pixel of the Medipix2MXR detector to correct for the inter-pixel variation. The process of fine-tuning these adjustment bits to produce an optimal uniformity of the thresholds is known as *equalisation.* The equalisation process adopted for the work in this chapter was based on that proposed by Tlustos et al. (2006). To create an equalisation mask, it is possible to use an external monoenergtic gamma source and to adjust each pixel so that the count rates at a given THL are approximately equal. However, the yields of available radioactive isotopes or fluorescing metallic foils are too low for a prompt equalisation. For simplicity, the Medipix2 equalisation method employed at the University of Canterbury uses the *noisefloor*, without requiring any external source. Comparisons between the two methods have been well studied, e.g. by Procz et al. (2009).

While it is usually avoided during image acquisition, the electronic noise serves as a definitive signal intrinsic to every pixel. A noisefloor dispersion curve is the distribution of THL values at which the pixels encountered the intrinsic signal and started to register apparent count. The goal of the equalisation process is to obtain a matrix containing the fine-tuned adjustment value, between 0 and 7, for all pixels. Upon loading the equalisation mask, every pixel across the chip encounters the noisefloor at an approximately constant threshold level. Note that the noisefloor level may differ from one chip to another.

Prior to equalisation, an additional matrix was used to switch off unresponsive pixels suffering from imperfect production or bump-bonding. The corresponding

pixels in the resultant projection image are rectified in the *pre-processing* chain, which will be described in the next section. In the lowest adjustment settings (adj. low = 0), a noisefloor dispersion curve was generated with the 3 adjustment bits for every pixel set to off (000). At the other extremity (adj. high = 7), a similar noisefloor distribution was measured by setting the adjustment bits to 111 for all pixels. In the MXR, the input current to the pixel equalisation DACs is controlled by THS. With regard to equalisation process, THS determines the overlap between the two dispersion curves. An ideal THS setting overlaps these two distributions by one eighth of their widths. Given the optimal THS, the equalised noisefloor distribution is expected to be centered around the mid-value of the overlap region, with its width compressed to be one seventh of the distance between the 000 and 111 distributions.

To determine the THS value with this optimal overlap, the distance between the two dispersion curves was measured over the entire range of THS DAC values (0 to 255). The distance closest to the optimal one-eighth overlap value provided the optimum THS value, which was set to determine the adjustment bits for each pixel. In addition to the low and high adjustment settings, the remaining noisefloor distributions were computed for the intermediate adjustment values (1-6). Of the eight possible settings, each pixel is assigned the adjustment bits that locate its noisefloor at the threshold value closest to the centre of the overlap region and an equalisation mask is constructed. A final noisefloor measurement reveals the equalised noisefloor, as depicted in figure 5.5.

Similar equalisation procedures for THH have been reported by other groups (Procz et al. 2009), while Llopart (2007) stated that the same adjustment mask may be applied to THH. In the Medipix3, the global positive and negative currents are determined by DAC_pixel and ThresholdN, respectively. Generally speaking, the DAC_pixel and ThresholdN DACs combined to have a similar effect as the THS
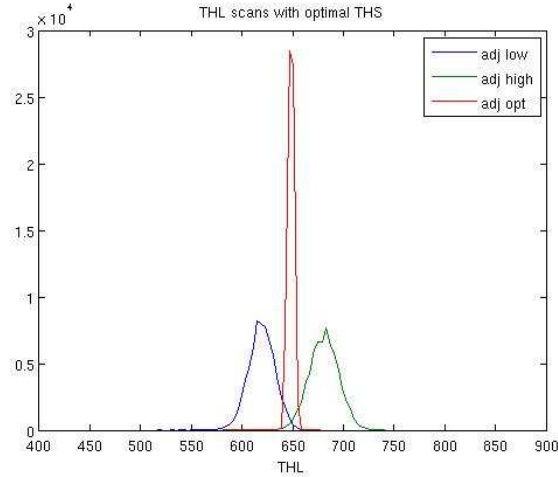
Figure 5.5: *An example of threshold equalisation in Medipix2MXR compared the equalised noisefloor dispersion (red) to the wider unadjusted distributions obtained with the lowest (blue) and highest (green) adjustment bits of 000 and 111, respectively.*

in the MXR and the Medipix3's equalisation mask can be provided by a 4-bit adjustment DAC for each of the two discriminators. Walsh et al. (2011b), Ronaldson (2012) and Doesburg (2012) detailed the equalisation process of Medipix3 for the MARS camera.

5.4   Image pre-processing for the MARS-CT

Equalisation ensures the dispersion in pixel response is minimised for image acquisition. However, imperfections remained in the current production of the Medipix sensor and/or ASIC layer(s). Silicon sensor layers often demonstrate a comparatively higher quality, but defects are particularly obvious with the higher-Z sensor layers such as GaAs and CdTe (Aamir et al. 2011a). Furthermore, malfunctioning detector elements spotted during equalisation were typically inhibited. Bump-bonding failures or radiation damage may result in a larger group of pixels being disabled. An image *pre-processing* chain was required for the projection images

to avoid artefacts (such as ring artefact) in the reconstructed images. Figure 5.6 shows an example of images obtained using a GaAs Medipix2MXR detector prior to and after pre-processing. Damaged pixel clusters and a column of malfunctioning pixels in this particular detector are apparent in figure 5.6a. These detector regions were necessarily avoided during image acquisition and were overlapped using the remaining detector area in the pre-processing steps.

Pre-processing of MARS images was initially performed in Matlab. Improvisation of the Matlab framework led to an in-house software (Tang et al. 2012). As mentioned in section 5.1, the MARS-CT scanner allows for acquisition using several lengths of detectors to compensate for the relatively small size of the Medipix. By translating the camera over several detector lengths, the entire imaging object (e.g. a rat in figure 5.6) can be covered in the FOV. Image stitching is thus the first process of pre-processing. When imaging across a larger FOV, a correction using an open beam image of air is required to normalise the x-ray intensity variation across the FOV. The subsequent step involves the interpolation, or inpainting, of inhibited pixels. Every inhibited pixel acquired the average value of its eight adjacent pixels. Unstable pixels that did not behave within the allowed photon counting noise were also identified and corrected in this process. As presented in Tang et al. (2012), the inpainting and stitching processes may be omitted when the algebraic reconstruction technique is employed. However, the traditional filtered back-projection reconstruction of MARS-CT images using Octopus (Dierick et al. 2004) still requires the entire pre-processing procedure to obtain a final projection image as shown in figure 5.6b.

(a)

(b)

Figure 5.6: (a) Initial projection image showing several damaged pixel clusters and a few malfunctioning columns. They repeated in the projection image (a) as the camera was translated across seven detector lengths to encompass the entire FOV. These faulty regions were overlapped with the remaining detector area upon image *stitching*. The pre-processing chain continued with the normalisation using an open beam (air) measurement and the interpolation of irresponsive or unstable detector elements. The final result of a pre-preprocessed image is shown in (b).

5.5 Spectrum measurement in Charge Summing Mode

Using a 300 μm Si Medipix3.0, CSM has been previously demonstrated by our group to reduce the misallocation of multiple counts at lower energies (Ronaldson et al. 2011). For a given pixel size, the effect of charge sharing is proportional to the thickness of the sensor layer (Llopart 2007). The aim of this work was to examine the performance of the 1 mm CdTe Medipix3.0 in CSM.

5.5.1 Methods

A MARS camera was installed with 6 Medipix3.0 chips bump-bonded to a 1 mm thick CdTe sensor layer. The americium source had an approximated activity

of 1.6 GBq (initial activity was 1.7 GBq in 1974) and was placed approximately 5 mm in front of the MARS camera. Because of its small spot size, the americium source was directed to the centre of only one of the CdTe Medipix chips. A bias voltage of 400V was applied. `Threshold0` was varied from 511 to 0 in steps of 3. 40 exposures of 3 seconds were taken at each threshold step for increased signal-to-noise ratio. It was reported that flaws in the arbitration circuitry design preferentially allocate counts to the pixels with lower thresholds (Ballabriga et al. 2011b). The detector's global pixel variation was therefore not equalised prior to this measurement to avoid the reported behaviour.

To post-process the measurements, pixels with unexpected CSM behavior were ignored. These include pixels which showed rapid changes within a small number of steps and pixels that did not rise from or fall back to zero. The threshold counts were differentiated to form a spectrum for each of the remaining (approximately 6000) pixels. The differentiated spectra were grouped (and averaged) according to the total intensity and were aligned on the 59.5 keV peak. The full width at half maximum of the 59.5 keV americium-241 peak was measured to provide an estimate on the energy resolution of the unequalised chip.

5.5.2   Results

Figure 5.7a shows the integrated counts of the 40 frames summed over all threshold steps. Different ranges of total intensity were grouped and plotted using various colors. The top left corner of the image revealed a region of missing bump bonds. The americium-241 characteristic peak at 59.5 keV is apparent in figure 5.7b. The spectra were scaled to the spectrum for the pixels with the highest total counts (the red spectrum). In addition, cadmium and tellurium have respective fluorescence energies at 23.2 keV and 27.5 keV. The corresponding escape peaks as a result of the Am-241 gamma source of 59.5 keV were partially

resolved, at 36.8 keV and 32.6 keV respectively, and are shown towards the left of the 59.5 keV peak (solid arrow). The combined Cd and Te fluorescences can be seen on the far left of the spectra (dashed arrow). The energy resolution of the unequalised chip was estimated to be 7 keV.

5.6 Spectral CT data acquisition using Medipix3.1

The equalisation and several DAC values of the first Medipix3 design (Medipix3.0) was prone to destabilise over a relatively short period of time (Ronaldson et al. 2011, Walsh et al. 2011b). Although the stability was not quantified, the Medipix3.1 was observed to be a more stable chip. The equalisations were particularly stable over comparatively longer times of weeks rather than days. A MARS camera with four Medipix3.1 detectors was therefore equalised and operated in spectroscopic mode. Charges were collected and compared from a $55 \times 55 \, \mu m^2$ region with the charge to the other 3 pixels being discarded (Walsh et al. 2013), since every pixel of the quad Si Medipix3.1 assembly used in this work was bump-bonded at manufacture. Note that the actual spectroscopic mode requires only one in every four ASIC pixel terminals to be connected to the semiconductor sensor layer (Ballabriga et al. 2011a).

5.6.1 Methods

A *spectral phantom* was designed and created by the MARS group. It contained two concentric rings of 7 evenly spaced capillaries each. The outer capillaries contained calcium chloride, "iodixanol" iodine complex, "Dimeglumine Gadopentetate" gadolinium complex, a contrast agent containing gold nano-particles, canola

(a)

(b)
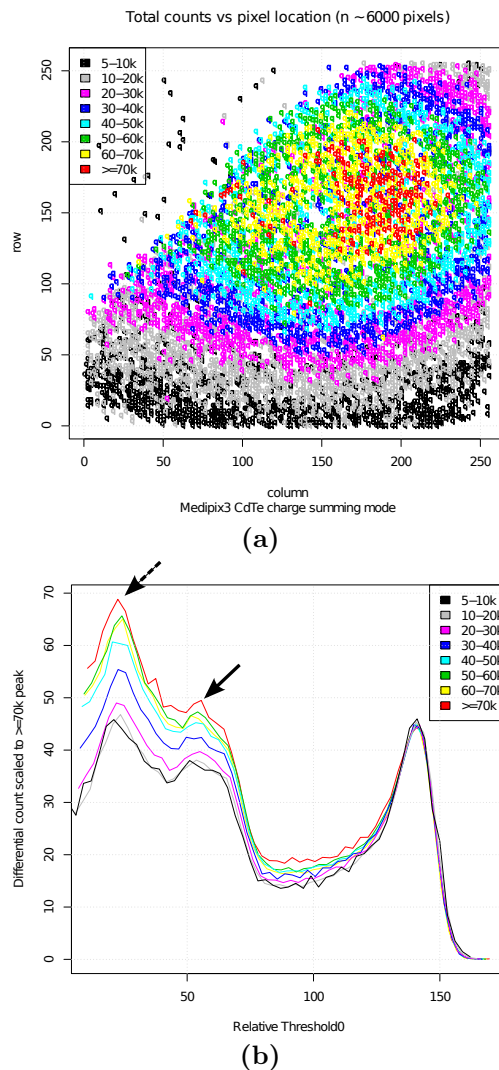
Figure 5.7: *(a) The integrated counts over the 40 frames versus pixel locations. A detector defect due to bump-bonding failure is visible at the top left corner of the image. (b) The differentiated spectra were color-coded to show a break down according to total intensity, which is correlated with the pixel location in (a). The americium characteristic peak of 59.5 keV is clearly depicted. The escape peaks of cadmium and tellurium were partially resolved and visible towards the left (solid arrow). The dashed arrow indicates the location of the combined Cd and Te fluoresences. Based on the locations of the 59.5 keV, the escape and the fluorescence peaks, the full width at half maximum of the americium-241 peak was measured to be approximately 7 keV.*

oil (to represent fat), water and air, respectively. The inner capillaries were not filled in this experiment.

A MARS-CT scanner, comprised of a MARS camera with four Medipix3.1 detectors and a micro-focus x-ray source (Source-Ray Inc, Ronkonkoma, NY, USA), was employed in this work. The x-ray source had a tungsten anode and 1.8 mm of aluminium (equivalent) intrinsic filtration. The spectral phantom was measured with the quad Si Medipix3.1 array, which was equalised using the standard MARS equalisation procedure (Walsh et al. 2011b). A bias voltage of 100 V was applied. The Source-Ray tube was set to 50 kVp and 100 µA. 720 projections were taken over 360 degrees to ensure sufficient data sampling. A study comparing image noise using different projection angles can be found in Tang et al. (2012). The MARS camera was operated in the spectroscopic mode, allowing for acquisition with 8 discriminators and 8 counters. CSM was disabled during the measurements. Due to the low absorption efficiencies of the silicon sensor layer, the 8 thresholds were spread evenly, at intervals of 2 keV, up to only 30 keV. 15 keV, 17 keV, 19 keV, 21 keV, 23 keV, 25 keV, 27 keV and 29 keV were measured in a single acquisition as a proof-of-concept study for the spectroscopic mode. Images were reconstructed using the commercial Octopus software (Dierick et al. 2004). A simple signal-to-noise ratio assessment was performed for the spectroscopic mode acquisition to evaluate the performance of the two individual Medipix3 counters.

5.6.2 Results

The eight images from the spectroscopic dataset are shown in figure 5.8. Starting from top position going clockwise, the materials are a gadolinium complex, an iodine complex, calcium chloride, canola oil, water, air and gold nano-particle contrast agent. The projection images were captured in a single acquisition, since

Threshold0 and Threshold1 of the four pixels alternate to form the eight threshold energies. Images at the threshold energies of {15, 19, 23, 27}keV were acquired by the four Threshold0's counters (counters {0, 2, 4, 6}). Likewise, counters {1, 3, 5, 7} of Threshold1 provided images at the threshold energies of {17, 21, 25, 29}keV.

Figure 5.9 shows the measured signal to noise ratio (SNR) of the 7 capillaries at 8 energies. SNRs for the low-Z (air, oil and water) and high-Z (calcium, iodine, gadolinium and gold) materials in the spectral phantom are plotted in figure 5.9a and figure 5.9b, respectively. SNRs for the counters associated with Threshold0 (bottom axis) are plotted with solid lines, whereas the dashed lines in figure 5.9 indicate the corresponding SNRs for the Threshold1's counters (top axis). In general, the Threshold0's counters show comparatively lower SNR performance than the Threshold1's counters and for all materials, SNR for e.g. counter 1 at 17 keV (lowest energy of Threshold0) was lower than the SNR for counter 4 at 23 keV (third energy of Threshold1)
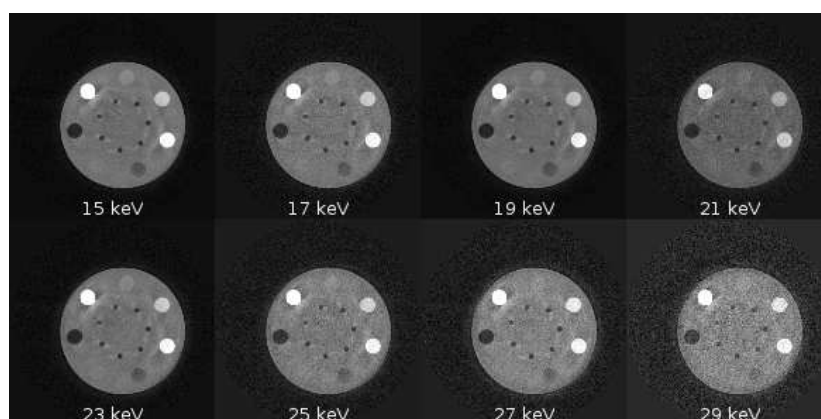
Figure 5.8: *A montage of a spectroscopic mode acquisition using Medipix3.1. The capillaries contain (from the top position and going clockwise) a gadolinium complex, an iodine complex, calcium chloride, canola oil, water, air and a contrast agent containing gold nano-particles, respectively. All 8 energies were acquired in one exposure.*
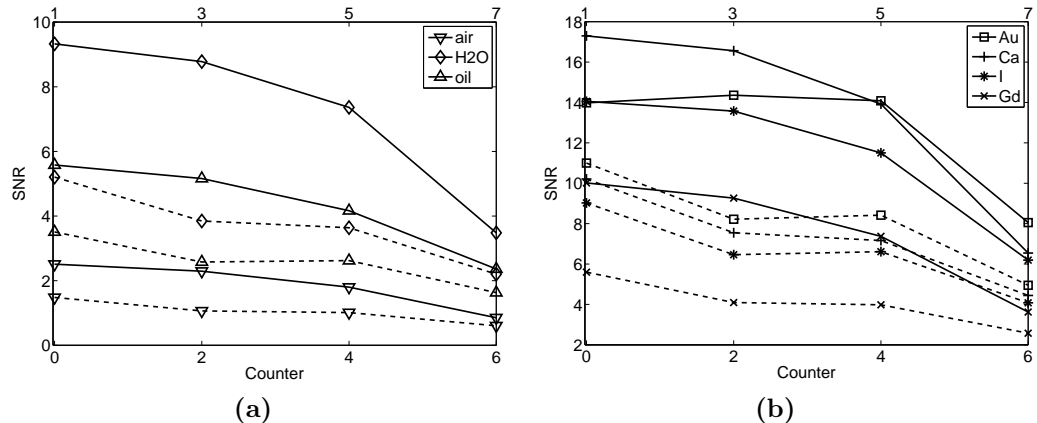
Figure 5.9: *SNR of the seven capillaries within the spectral phantom with relatively (a) low-Z and (b) high-Z materials. The* Threshold0*'s counters (solid lines) are numbered even (counters {0, 2, 4, 6}) and counters {1, 3, 5, 7}) are associated with* Threshold1*.* Threshold0*'s and* Threshold1*'s counters are labelled on the bottom and top horizontal axes, respectively. SNR for the image at 17 keV (lowest energy of* Threshold1*) was shown be lower than SNR at e.g. at 23 keV (third energy of* Threshold0*) for all materials and in general,* Threshold1 *has comparatively lower SNR performance, which shows a limitation in the Medipix3.1's spectroscopic mode.*

5.7 Discussion

The CSM of Medipix3.0 was demonstrated to be relatively effective in allocating shared signal in a single pixel and to depict the characteristic peaks of an americium-241 gamma source. Surprisingly high pixel variations were reported for this version of Medipix3 (Ballabriga et al. 2011b). Given that the resultant misallocation of photon counts has been previously observed (Gimenez et al. 2011) and that the limitations with the CSM has been revealed in studies within the MARS group (Doesburg 2012, Ronaldson 2012), the CSM measurement in this work produced encouraging performance. In particular, the spectra obtained with CSM at 55 µm pixel pitch resemble that of 110 µm² pixels in SPM (Koenig et al. 2012). However, the energy resolution of the Medipix3.0 detector used for the work in section 5.5 is approximately 2.5 times worse compared to the SPM

spectrum using the $110\,\mu m^2$ pixels in Koenig et al. (2012). The full width at half maximum of the 59.5 keV peak in figure 5.7b was widened by the residual charge sharing tail immediately to the left of the peak. An increase in pixel size can directly reduce charge sharing, which may thereby enhance the energy resolution of the detector, as shown in the work of Koenig et al.'s (2012). An improved charge summing arbitration is also believed to be capable of further reducing the charge sharing tail. A narrower full width at half maximum can be expected as a result.

This preliminary spectral measurement using CSM has provided the opportunity to explore the novel feature of pixel communication and charge summing in Medipix3 with the MARS camera. In figure 5.7b, counts were still registered at energies between the 59.5 keV Am-241 peak and the escape peaks of cadmium and tellurium. This suboptimal outcome of the CSM may be attributed to the chip not being equalised. The candidate attempted to acquire similar spectrum upon equalising using the MARS Medipix3 equalisation procedure (Walsh et al. 2011b). However, measurements using a MARS camera with a Si Medipix3 were unsuccessful in providing similar analysis, which may be due to the low absorption probability of the sensor layer at the characteristic Am-241 energy. Limitations of the Medipix3.0 have been reportedly corrected with a redesigned charge summing arbitration architecture in the next version of the Medipix3 family, called Medipix3RX (Ballabriga et al. 2012). The Am-241 spectrum measurement in section 5.5 hence promises improved spectroscopic performance with the integration of the Medipix3RX into the MARS camera.

Similarly, the compatibility of the MARS camera with the spectroscopic mode was demonstrated using a Si Medipix3.1 detector. The candidate tested the implementation of the feature in the MARS Python library with pilot studies before images of a spectral phantom at 8 simultaneous energies were acquired (Walsh

et al. 2013). Previous images of multiple energy ranges were acquired independently at different threshold energies (e.g. in Ronaldson et al. (2012)). Subtracting counts of one threshold from another include quantum noise from both measurements. In addition to shortening the exposure time, forming energy bins using acquisition in the spectroscopic mode does not introduce further photon counting noise, since all counters share a single x-ray exposure. However, due to its bump-bond configuration at manufacture, the Si Medipix3.1 detector used for the work in section 5.6 only counted photons from a $55 \times 55\,\mu m^2$ area, which is 4 times smaller than the $110 \times 110\,\mu m^2$ area expected for the spectroscopic mode. Even with the hardware limitation, this work demonstrates that the Medipix3.1 ASIC is capable of imaging in spectroscopic mode with $55\,\mu m$ bump-bonding.

In the spectroscopic mode, the 2 counters of each pixel are multiplexed in a 2×2 configuration to create the 8 counters. Consequently, the image quality of the 8 counters is related to the performance of the individual counters in a pixel. In our spectroscopic measurements, the 8 counters were specifically shown separately as counters $\{0, 2, 4, 6\}$ from Threshold0 in SPM and counters $\{1, 3, 5, 7\}$ of Threshold1 in SPM. Threshold1 has poorer equalisation, which resulted in the comparatively lower SNR in counters $\{1, 3, 5, 7\}$ in spectroscopic mode (figure 5.9). It is expected that the redesigned chip of the Medipix3RX will have equalisation and imaging performance independent of the discriminator.

5.7.1 Proposed measurements to verify the theoretical model

In practice, a PCD such as the Medipix detector may fail to respond to each photon if the detector's count rate is slower than the incoming flux rate and the detected spectrum will be distorted (Taguchi et al. 2010, Wang et al. 2011). While the BEAMnrc model incorporates the consideration of scattered radia-

tion, the effects of pulse pileup and finite energy resolution of a PCD on the optimisation can be examined, provided that the Medipix PCD can perform adequately in the charge summing and spectroscopic modes of operation. In order to validate the theoretical and simulation models, it was initially intended in this thesis to apply the decomposition method presented in section 4.1.3 to identify e.g. the microcalcification regions within a Gammex 156 American College of Radiology mammography accreditation phantom (Gammex Inc, Middleton, WI, USA) available to the MARS team. The optimal energy bins for decomposing calcifications from breast-like tissue (Gammex Inc. 1997) can be experimentally validated upon measuring the Gammex 156 phantom using an exhaustive range of bin border energies. Similarly, the SNR of the decomposition can be compared to the theoretical predictions for the tube voltages of $35\,\mathrm{kVp}$ and $50\,\mathrm{kVp}$ (see Appendix A) and the theoretical optimisation of count per pixel for achieving a SNR of ≥ 5 can be verified for the Si or CdTe Medipix detectors.

5.8 Concluding remarks

The candidate's contribution towards multiple aspects of the MARS-CT spectral scanning system was presented in this chapter. The candidate implemented the threshold equalisation for the Medipix2MXR detector in Matlab and contributed to the improvement of a Matlab image *pre-processing* algorithm to correct for faulty and unstable pixels. These two processes improved the quality of the photon counting projection images prior to and after the acquisition, respectively.

Measurements using a Si Medipix3.0 detector with comparatively lower absorption at the Am-241 characteristic energy were unsuccessful in depicting the spectroscopic features, the results were presented at the *14th International Workshop on Radiation Imaging Detectors*. Also, the corresponding manuscript was

prepared for publication in the conference proceedings by the candidate. To realise the Medipix3's potential of imaging with 8 simultaneous threshold energies, the candidate implemented the spectroscopic mode in the MARS Python library and tested the feature with pilot studies. A set of preliminary measurements to examine the Medipix3.1 in the spectroscopic mode was acquire in collaboration of other team members and overseas collaborators (see Walsh et al. (2013)).

As discussed in section 5.7, the performance of the available Medipix3 detectors was limited due to the known issues with the detector's electronics, which prohibited an effective equalisation in the CSM in section 5.5 and the equalisation in the spectroscopic mode in section 5.6 was shown to be dependent on the discriminator (Threshold0 or Threshold1 in SPM) used. A highly accurate measurement of an x-ray spectrum in the CSM to decompose materials was not possible at this time, as a result. While the measurements presented several limitations (see figure 5.7b and figure 5.9), they demonstrated the integration of the Medipix3 detectors in the MARS camera, particularly in the spectroscopic and charge summing modes. Furthermore, the unwanted behaviour of charge misallocation in the Medipix3.0's CSM has been corrected in the Medipix3RX (Ballabriga et al. 2012).

Together with the ongoing development of the equalisation routine, the availability of Medipix detectors bump-bonded specifically for the spectroscopic mode can provide improved spectroscopic measurements. Once the limitations have been overcome, the Medipix detector can be used to measure the Gammex 156 phantom with microcalcification regions, to verify the theoretical and simulation models presented in chapter 3 and chapter 4, respectively. Specifically, the estimation of pixel counts required and the optimal bin border energy provided by the theoretical model can be applied on the measurements using e.g. the next variant of Medipix3, Medipix3RX (Ballabriga et al. 2012).

Chapter 6

General conclusions and discussion

6.1 General conclusions

The work presented in this thesis investigated the optimisation of material discrimination using spectral x-ray imaging. This has been achieved through the development of a novel theoretical algorithm in Chapter 3 to optimise bin border energies for maximum material discrimination. The proposed model does not assume the knowledge of material quantity for the determination of the effective attenuation basis functions. The matrix manipulation required to determine the Fisher information matrix can be avoided, too. In concurrence with other methods, our model shows that the benefits of spectral imaging can be maximised by the optimisation of energy bins to provide improved confidence in material thickness estimation. It is also a strength of the theoretical model to be able to estimate the pixellated dose (photon counts) required for achieving a desired signal-to-noise ratio in a decomposed image.

The decomposition method in this thesis was derived from the optimisation

model. Simulated spectra can be decomposed into two non-K-edge and a K-edge materials, as expected. This has been demonstrated in Chapter 4 by decomposing the simulated projection measurements into basis images of up to two contrast agents (calcium and iodine) within a water cylinder. For the validation of the theoretical model, scattered radiation was included in the simulated projections and the theoretical predictions demonstrated excellent agreement with the MC simulations on the estimation of image noise (figure 4.8 and figure 4.9), as well as on the optimal bin border positions (figure 4.10).

Upon validation, the theoretical model was applied to optimise mean glandular dose required to effectively decompose calcification from within breast tissue in order to compare the benefits of spectral imaging with dual-energy mammography. It was estimated that spectral imaging is capable of achieving the same image quality in the calcification image at a similar dose level as two optimised monoenergetic beams (see section 4.3.1).

It was initially the aim of the this thesis to apply the theoretical optimal parameters and the decomposition method on spectral measurements obtained using the Medipix PCD. However, electronic issues had been known to exist with the detector versions available for the work in this thesis. The focus was thus shifted to contributions on the development of the MARS spectral scanning system and experimental work on the Medipix detector. Preliminary measurements using the charge summing and spectroscopic modes, presented in section 5.5 and section 5.6, respectively, indicated that the integration of the Medipix detector into the MARS camera is promising in providing spectral x-ray measurement of up to 8 energies, with the expected limitations due to the known problems related to the equalisation process. It is expected that, when available, the revised version of Medipix detector (Medipix3RX) can provide spectra with improved spectroscopic accuracy. The optimsed scanning parameters can be applied on

measurements of a mammography phantom using the Medipix3RX detector and thereby provide verifications to the theoretical optimisations.

6.2 Discussion

The penultimate sections of the previous chapters provided discussions on the respective topics. A more general discussion and the identified areas of future research, based on the overall work presented in this thesis, are highlighted here.

6.2.1 Limitations of approach

The theoretical model does not account for the finite energy resolution of a PCD and the pulse pileup effect. Both of the effects degrade the performance of material decomposition and may affect the optimsation of material discrimination. The decomposition method used in this work therefore requires an additional detector response function. Suggestions on how to improve the theoretical model by incorporating the respective effects of energy resolution and pulse pileup have been identified as areas of further work.

The agreements between the theoretical and simulation models were generally limited by computational and hardware efficiency. While the largest allowable matrix size was imposed by Matlab on the theoretical model, the simulation model is limited by the relative inefficiency of generating incident photons and the computing time required to readout the phsp information.

The accuracy of the material decomposition method can be affected by scattered radiation, which had to be taken in account using the particle interaction tracking function in the BEAMnrc simulation. A similar approach of accounting for scattered photons must be considered when decomposing a spectrum measured using the Medipix detector.

Experimental work on the Medipix detector in this thesis was limited to demonstrating its implementation in spectral imaging. Technical limitations with the electronics of the Medipix3.0 and 3.1 detectors have adversely affected the functionality of the charge summing mode, which was necessary for an accurate measurement of an x-ray spectrum required for the projection-based decomposition in this work. It was reported that the electronic issues has been addressed with the improved in chip design in the Medipix3RX detector (Ballabriga et al. 2012). An important piece of future work is therefore to experimentally verify the theoretical optimisations with the revised version of Medipix3.

6.2.2 Suggestions for future work

The proposed decomposition method has been applied on K-edge imaging to discriminate up to three materials. Without the existence of a suitable K-edge within the imaging energy range, only 2 non K-edge materials can be decomposed, as dictated by the linear dependency of the Compton and photoelectric components of x-ray attenuations. Decomposition of multiple (>2) non K-edge materials is only feasible by incorporating additional steps in the decomposition technique or by augmenting the existing system of equations with further information. Both techniques have been demonstrated in the image-space decomposition. Segmentation of the reconstructed pixels into classes of materials (Le & Molloi 2011, Alessio & MacDonald 2013) or inclusion of a volume conservation constraint within a pixel (Ronaldson et al. 2012) can be performed prior to the estimation of material/attenuation concentrations using e.g. the least squares minimisation. An interesting approach to decompose more than 2 attenuation components or materials in the projection space can be tested by the incorporation of up to 4 principal attenuation components as observed by Bornefalk (2012).

The presented BEAMnrc projection framework can be extended to simulate a

CT gantry rotation by duplicating a first generation CT geometry. A pencil x-ray beam can be translated before being rotated over a full rotation as demonstrated by Bazalova et al. (2012). A more straightforward CT simulation is deemed feasible with an EGSnrc's user code, called egs_cbct, currently under development (Thing 2013). Similarly, the theoretical algorithm can be applied to optimise energy selection and to estimate count required for a cylindrical, symmetrical imaging object, as demonstrated by Roessl et al. (2011).

It should be noted that the estimated MGD in section 4.3.1 and Appendix A were based on a practical polychromatic source, for comparisons with the optimisation of two monoenergtic beams by Johns & Yaffe (1985). As seen in the subsequent experimental implementation of dual-energy mammography (Johns et al. 1985), a polychromatic source exposes a higher patient dose compared to the monoenergtic sources. This is, of course, coupled with the technical complexities of their radiography system. For the given image quality, however, an even lower MGD may be achieved in this work with an optimal kVp of the tungsten anode, by using a different anode target and filtration (e.g. a molybdenum/rhodium combination), or by means of image smoothing as in Johns & Yaffe (1985).

Acquisition with the advanced features of the Medipix detector in this work encountered limitations related primarily to the equalisation process. While the multi-energy acquisition of the Medipix3 has been realised, its performance hinges on the equalisation of pixel sensitivity dispersion (see figure 5.9). Deterioration in the equalisation mask over time can directly affect energy resolution and CT number calibration. The improved equalisation process in the latest Medipix3RX detector with new charge summing logic (Ballabriga et al. 2012) will lead to a higher consistency in using the Medipix detectors.

Given the improved spectroscopic performance in the CSM, the theoretical algorithm can be implemented to optimise projection measurement using the

Medipix detector. A Gaussian resolution function and pulse-pileup models such as Taguchi et al.'s (2010) or Wang et al.'s (2011) can be incorporated in (3.2), as part of the forward projection process in the optimisation algorithm and the decomposition method, to account for the detector's finite energy resolution and read-out speed, respectively. Finally, the theoretical model can also be applied to, e.g. investigate the minimum contrast agent quantity required for a sufficient image quality with and without the influence of technical complications of PCD.

6.2.3 Outlook

This thesis focused on spectral x-ray projection imaging. The clinical applications of photon counting technology has been demonstrated in mammography (Fredenberg et al. 2010, Danielsson 2012) and there is a growing interest in applying PCDs to replace dual-energy CT as the next generation of energy-sensitive clinical CT imaging. Several technical challenges, of course, must be addressed before energy-resolving PCDs can be applied to clinical CT imaging. One primary limitation of the current PCD technology has been widely identified to be the count rate capability (Taguchi et al. 2010, Roessl et al. 2010). In a clinical x-ray examination, a patient may be exposed with 10^7 to 10^9 photons per mm^2 per second, depending on the imaging task (Overdick et al. 2009). Count rate of the detectors listed in table 2.5.2 ranges from 6×10^6 to 1.5×10^8 photons per mm^2 per second (Overdick et al. 2009, Roessl et al. 2010). A PCD may fail to respond to each photon if the detector cannot maintain the clinical count rate, or pulses may temporally pileup and the detected spectrum will be distorted. The essential hardware improvements in spectral x-ray imaging therefore include increasing the count rate capabilities of PCDs, in addition to the development of sensor layers with suitable properties and sizes for clinical imaging.

Alternatively, pulse pileup models have been proposed as possible solutions to

mitigate the effect (Taguchi et al. 2010, Wang et al. 2011). The development of similar algorithms to account for e.g. scattered radiation with energy sensitivity is critical and, as shown in this thesis, it is equally important to optimise the energy-sensitive photon counting measurements for the maximum benefits of spectral imaging. With the ongoing development in all aspects of spectral x-ray imaging, as reflected by the active research in micro-CT imaging of small animal and human specimen, including the MARS-CT scanner, it is believed that the photon counting technology is promised a very bright future in clinical imaging.

Appendix A

Mammography dose calculations and optimisations

This appendix presents a method to calculate MGD, which enables the determination of dose required for decomposing calcification from breast tissue using spectral x-ray imaging. Given a tungsten spectrum based on an x-ray tube available at the University of Canterbury, the MGD required for the SNR threshold of 5 was estimated to evaluate the advantage of spectral x-ray imaging.

A.1   Mean glandular dose calculation

Using the theoretical model in chapter 3, the optimal photon counts for achieving a given SNR in a material basis image can be calculated. The breast entrance photon fluence for energy, $\Phi(E)$ in units of photons/mm^2/keV, can be converted into MGD (Boone 2002, Boone & Seibert 1997):

$$MGD = \int_{E_l}^{E_h} \Phi(E) \cdot \frac{\chi}{\Phi}(E) \cdot DgN(E) \, dE. \tag{A.1}$$

$\frac{\chi}{\Phi}$(E) denotes the exposure per photons/mm^2 in an energy interval (in units of mR per photons/mm^2) and has been derived by Johns & Cunningham (1983) to be:

$$\frac{\Phi}{\chi}(E) = 0.00873 \cdot \left(h\upsilon(\mu_{ab}/\rho)_{air}\right)^{-1} \text{J/kg/R}, \tag{A.2}$$

where hυ represents the energy of the photon. Substituting hυ with E, the energy of the photon in keV, the number of photons/mm^2 per roentgen (R) is

$$\frac{\Phi}{\chi}(E) = 5.45 \times 10^8 \cdot \left(E(\mu_{ab}/\rho)_{air}\right)^{-1} \text{keV/mm/R}, \tag{A.3}$$

after some unit conversions including $1\,\text{keV} = 1.602 \times 10^{-16}\,\text{J}$. Note that the *Système International* (SI) unit of radiation exposure is coulomb per kg (C/kg), whereby $1\,\text{C/kg}$ equals to approximately $3876\,\text{R}$. Values for the mass energy absorption coefficient $(\mu_{ab}/\rho)_{air})$ can be obtained from the NIST database (Hubbell & Seltzer 1996). DgN(E) in (A.1) is the normalized glandular dose coefficient (in units of mGy/R). The fit equations of the DgN(E) values for three glandular compositions (0%, 50% and 100%) were reported by Boone (2002) for breast thicknesses between $2\,\text{cm}$ and $10\,\text{cm}$. The equation for a $4\,\text{cm}$ breast of 50% glandularity was used in this work.

A.2   Mean glandular dose optimisation

Given the benchmark of $4.2\,\text{mGy}$ in Johns & Yaffe (1985), the Source-Ray SB-80-1K x-ray tube (Source-Ray Inc, Ronkonkoma, NY, USA) utilised in previous spectral CT experiments was modelled (Ronaldson et al. 2011, Walsh et al. 2011a). The tube comprises a tungsten anode with an $1.8\,\text{mm}$ of aluminium (equivalent) intrinsic filtration. Calculation was performed for a tube voltage of $35\,\text{kVp}$, which is the minimum operating voltage of the tube (see tube's operation manual), as

well as for another tube voltage of 50 kVp previously used in studies by our group (Ronaldson et al. 2011, Ronaldson et al. 2012). The bin border energy for two abutted bins was optimised for both spectra. The detection quantum efficiency (DQE) and the energy resolution of the PCD was assumed to be ideal. In addition, the optimal MGD was calculated for a PCD with a 300 µm silicon, which is a common type of sensor layer for the Medipix detector (see e.g. Llopart et al. (2002) and Doesburg et al. (2012)). The spectral response of the silicon detector was incorporated into (3.2) while the 1 mm CdTe sensor layer was demonstrated to be ideal at below 50 keV (Aamir et al. 2011a). Two pixel sizes were employed: the 55 µm² typically found in the Medipix and the 85 µm² recommended for mammography by Bushberg et al. (2003).

The attenuation coefficients of calcium carbonate (CaCO3) and the ICRU-44 breast tissue (ICRU 1989) were obtained from Berger et al. (2005). The density of CaCO3 was defined to be 2.93 g/cm³ as in Lemacks et al. (2002) to mimic the calcification. Given the above options of exposure configurations, the lowest MGD was determined to be 1.67 mGy with the 1 mm CdTe sensor layer of 85 µm² pixel size and the 50 kVp tube voltage, using a bin border energy of 29 keV. The same detector yields the the minimum dose is 3.65 mGy for the 35 kVp spectrum, with a bin border energy of 26 keV.

The optimal dose to achieve a SNR of 5 in quantifying the calcified feature was tabulated in table A.1 and table A.2 for the 35 kVp and 50 kVp spectra, respectively. MGD was calculated using (A.3) whereas the skin exposure was given by (A.1).

Detector	Skin exposure (mR)	MGD (mGy)	Optimal bin border (keV)
DQE = 1 85 µm	736	3.65	26
300 µm Si 85 µm	918	4.55	26
DQE = 1 55 µm	1756	8.70	26
300 µm Si 55 µm	2192	10.87	26

Table A.1: MGD required for SNR $\geq$ 5 in the CaCO3 basis image estimated using the theoretical model. The entrance skin exposure and optimised bin border position are also tabulated. 85 µm is the recommended pixel size for mammography in (Bushberg et al. 2003). 55 µm is the pixel size for the Medipix detector. The minimum dose for the 35 kVp SourceRay spectrum was 3.65 mGy using a 1 mm CdTe detector with 85 µm^2 pixels.

Detector	Skin exposure (mR)	MGD (mGy)	Optimal bin border (keV)
DQE = 1 85 µm	285	1.67	29
300 µm Si 85 µm	1269	7.43	27
DQE = 1 55 µm	682	3.99	29
300 µm Si 55 µm	801	4.69	27

Table A.2: The 50 kVp SourceRay spectrum was modelled and shown to be more optimal compared to the 35 kVp spectrum. The lowest achievable dose for a SNR $\geq$ 5 is 1.67 mGy.

Appendix B

Implementation of backprojection-filtration reconstruction on synthetically truncated data

In x-ray computed tomography imaging, the FOV of the imaging system can be smaller than the imaging object. It is also not uncommon that only the volume-of-interest (VOI) is irradiated for the reduction of radiation dose delivered to the subject. Under these conditions, the conventional Feldkamp-Davis-Kress (FDK) algorithm (Feldkamp et al. 1984) yields reconstructed images with artefacts when the projection data are truncated (Ogawa et al. 1984, Yu et al. 2006, Cho et al. 2007, MacDonald 2010).

An algorithm known as the backprojection-filtration (BPF) algorithm has recently been developed for exact image reconstruction from helical (Yu & Pan 2004) and circular (Yu et al. 2006, Cho et al. 2007) cone-beam CT data. The BPF approach is based on the lines connecting any two points on the source

trajectory specifically defined for helical cone-beam CT, known as the Pi-lines. For circular cone-beam CT, actual Pi-lines exist only on the midplane, as illustrated in figure B.1. Virtual trajectory and virtual Pi-lines have been introduced on the off-midplanes for the realisation of the approximated BPF algorithm (Yu et al. 2006, Cho et al. 2007). In the BPF algorithm for both helical and circular cone-beam CT, the one dimensional data filtration occurs in the image space, following the backprojection of the cone-beam data derivatives onto the Pi-lines. This reconstruction technique therefore requires only the projection data from the VOI. The filtering process in the FDK algorithm, however, takes place in the projection space, prior to the data rebinning. This leads to a larger data requirement compared to the BPF algorithm for artefact-free reconstructed images (Cho et al. 2007).
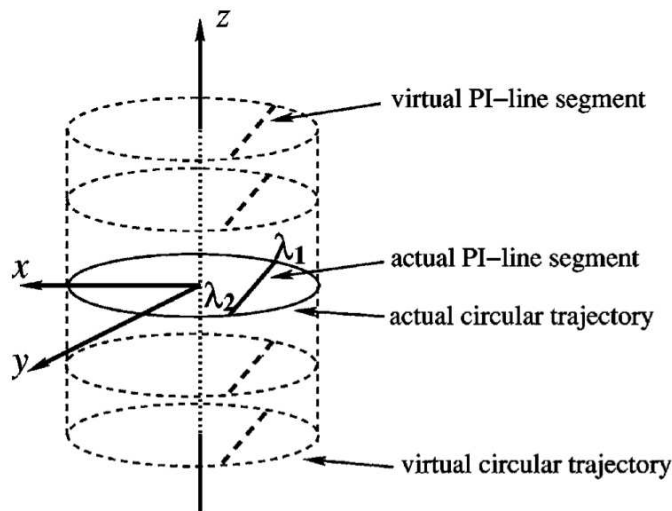
Figure B.1: *An illustration of actual and virtual Pi-lines in circular cone-beam CT by Yu et al. (2006) and Cho et al. (2007). Actual Pi-lines exist only on the midplane in circular cone-beam CT. The approximated BPF reconstruction can be achieved by introducing virtual trajectory and virtual Pi-lines on the off-midplanes.*

This appendix reports on a project that transpired from the temporary closure of the University of Canterbury due to the Canterbury earthquakes in 2011.

APPENDIX B. IMPLEMENTATION OF BACKPROJECTION-FILTRATION RECONSTRUCTION

As mentioned in section 1.2, the work in this appendix was carried out at the Nova Scotia Cancer Center in Halifax, Canada. The goal of this project was to implement the BPF reconstruction algorithm on synthetically truncated circular cone-beam CT data acquired on a megavoltage imaging system with low atomic number external targets in the linear accelerator (Robar et al. 2009). A Matlab code with a graphical user interface (GUI) was built to import Digital Imaging and Communications in Medicine (DICOM) projection data and to reconstruct based on the BPF algorithm developed by Yu et al. (2006) and Cho et al. (2007). Verification against a previously implemented FDK algorithm (Robar et al. 2009) as well as the qualitative and quantitative comparisons with the FDK reconstructed images were performed.

To ensure a sufficiently large field-of-view, the MARS CT scanner translates the Medipix detector over several detector lengths. This approach, however, lengthens the scanning time. The BPF reconstruction can be employed when the projection images are truncated as a result of the small detector size and may potentially be applied to small animal spectral CT imaging. Spectral CT may therefore benefit from the BPF reconstruction, even though the algorithm does not exploit the energy domain of spectral x-ray imaging.

B.1 Methods

B.1.1 BPF algorithm for circular cone-beam CT

The Pi-line based BPF reconstruction algorithm was first proposed by Yu & Pan (2004) for applications on helical cone-beam CT data. Based on Yu & Pan's (2004) works, Yu et al. (2006) and Cho et al. (2007) demonstrated an approximated BPF algorithm for reconstruction from computer simulated and experimental circular cone-beam CT data. In their works, four Pi-line parameters

$(x_\pi, \lambda_1, \lambda_2$ and $z_0)$ were introduced, with x_π being a point on a Pi-line connecting two points, λ_1 and λ_2, on a circular plane at $z = z_0$, as shown in figure B.2. The source rotates on the $z_0 = 0$ plane at a distance R (R $= 100\,$cm in this work) away from the rotational axis, with the source trajectory governed by

$$\vec{r_c}(\lambda) = (Rcos(\lambda), Rsin(\lambda), 0), \tag{B.1}$$

at an projection angle λ.

For a set of Pi-line coordinates $(x_\pi, \lambda_1, \lambda_2$ and $z_0)$, its location $\vec{r}$ relative to the axis of rotation can be expressed as (Yu et al. 2006, Cho et al. 2007)

$$\vec{r} = \frac{\vec{r_c}(\lambda_2) + \vec{r_c}(\lambda_1)}{2} + z_0\hat{e_v} + x_\pi\hat{e_\pi}, \tag{B.2}$$

where the direction of a Pi-line segment, $\hat{e_\pi}$, is given by

$$\hat{e_\pi} = \frac{r_c(\lambda_2) + r_c(\lambda_1)}{|r_c(\lambda_2) + r_c(\lambda_1)|}. \tag{B.3}$$

$\hat{e_v}$ in (B.2) denotes the unit vector along the vertical detector axis (see figure B.2). $\{\hat{e_u}, \hat{e_v}, \hat{e_w}\}$ thus describes the unit vectors of the rotation coordinate system and can be written as:

$$\begin{aligned} \hat{e_u} &= (-sin(\lambda), cos(\lambda), 0)' \\ \hat{e_v} &= (0, 0, 1)' \\ \hat{e_w} &= (cos(\lambda), sin(\lambda), 0)'. \end{aligned} \tag{B.4}$$

For the SDD (S in figure B.2) of $130\,$cm, the corresponding pixel coordinates (u_d, v_d) on our detector panel can then be related via fundamental trigonometry to be (Yu et al. 2006):

$$u_d = \frac{S\vec{r} \cdot \hat{e_u}(\lambda)}{R - \vec{r} \cdot \hat{e_w}(\lambda)}, \qquad v_d = \frac{S\vec{r} \cdot \hat{e_v}(\lambda)}{R - \vec{r} \cdot \hat{e_w}(\lambda)}, \tag{B.5}$$

APPENDIX B. IMPLEMENTATION OF BACKPROJECTION-FILTRATION RECONSTRUCTION
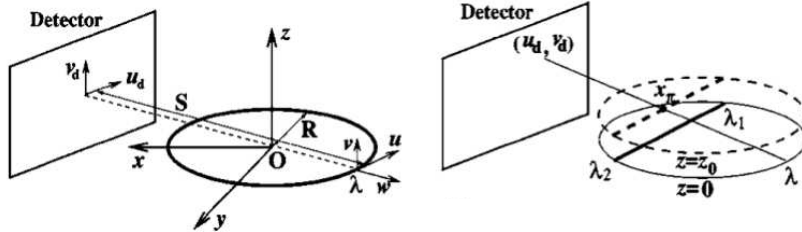
as depicted in figure B.2.

Figure B.2: *Pi-line coordinates as defined by Cho et al. (2007). $\{\hat{e_u}, \hat{e_v}, \hat{e_w}\}$ are the respective unit vectors along the $\{u,v,w\}$ directions, as shown on the left panel. Given the SDD, S, and the source's rotational radius, R, the detector element (u_d, v_d) is related to a point on the Pi-line x_π located at $\vec{r}$ via (B.5), for the midplane and off-midplanes (right panel).*

Given the Pi-line (B.2) and the pixel (B.5) coordinates above, a backprojected image, g_π, can be formed. A point x_π within the VOI can be reconstructed using

$$
\begin{aligned}
f_\pi(x_\pi, \lambda_1, \lambda_2, z_0) = &\Bigg[\int_{x_{\pi\lambda1}}^{x_{\pi\lambda2}} dx'_\pi \frac{\sqrt{(x_{\pi\lambda2} - x'_\pi)(x'_\pi - x_{\pi\lambda1})}}{x_\pi - x'_\pi} \\
&\times g_\pi(x'_\pi, \lambda_1, \lambda_2, z_0) + 2\pi P_0 \Bigg] \\
&\times \frac{1}{2\pi^2} \frac{1}{\sqrt{(x_{\pi\lambda2} - x_\pi)(x_\pi - x_{\pi\lambda1})}},
\end{aligned}
\tag{B.6}
$$

where P_0 represents the projection along the ray coinciding with the Pi-line segment. $x_{\pi\lambda1}$ and $x_{\pi\lambda2}$ denote the two ends of a Pi-line *support segment* (Cho et al. 2007). An example of the support segment is demonstrated in figure B.3. The reconstruction image is assumed to be empty beyond the support segments, or mathematically, $f_\pi(x_\pi, \lambda_1, \lambda_2, z_0) = 0$ for $x_\pi \notin [x_{\pi\lambda1}, x_{\pi\lambda2}]$. Defining ample x_π points and support segments allows for the entire VOI to be reconstructed (see figure B.3b). In this work, the default reconstructed image dimension was defined to be 796×796 pixels of size $0.3\,\text{mm}^2$ to enable direct comparisons with the results from Robar et al.'s (2009) FDK algorithm. However, the GUI offers the

specification of any desired image size and resolution, as well as several optional parameters.
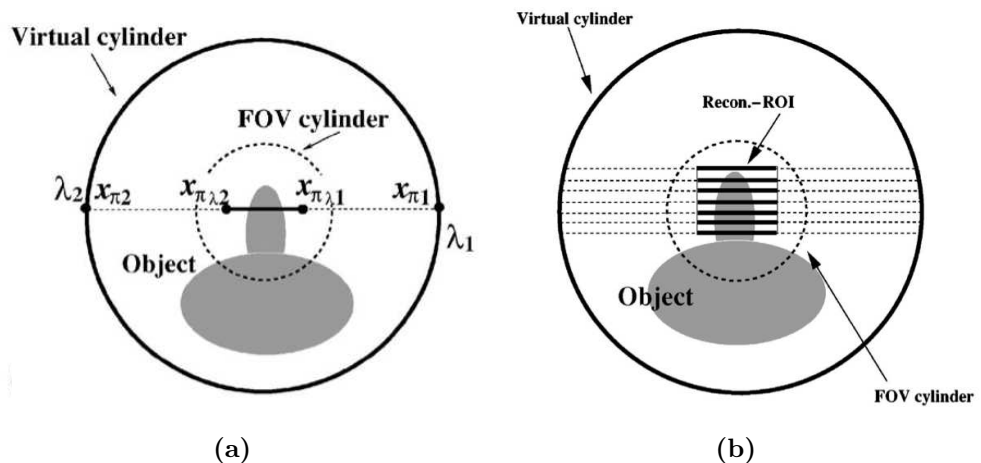

Figure B.3: *(a) A Pi-line support segment (straight solid line) defined by two end points $x_{\pi\lambda1}$ and $x_{\pi\lambda2}$ is part of the Pi-line, indicated by the straight dotted line. $x_{\pi1}$ and $x_{\pi2}$ mark the ends of the entire Pi-line. (b) A Pi-line support segment is selected to be wider than the imaging object within the FOV cylinder, which is determined by the beam angle. The reconstruction ROI on a $z = z_0$ plane can be defined to be, e.g. a rectangle with sufficient Pi-line support segments, as represented by the bold solid lines in (b). From Cho et al. (2007).*

In the BPF algorithm, the backprojected image (g_π) is composed of the cone-beam CT projection data, $P(u_d, v_d, \lambda)$, and its derivates (Yu et al. 2006):

$$
\begin{aligned}
g_\pi(x'_\pi, \lambda_1, \lambda_2, z_0) = &\int_{\lambda_1}^{\lambda_2} d\lambda \frac{S^2}{[R - \vec{r'} \cdot \hat{e_w}(\lambda)]^2} \\
&\times \frac{\delta}{\delta u} \left[\frac{R(P(u_d, v_d, \lambda))}{\sqrt{u^2 + v^2 + S^2}} \right] + \left. \frac{P(u_d, v_d, \lambda)}{\vec{r'} - \vec{r}(\lambda)} \right|_{\lambda_1}^{\lambda_2}.
\end{aligned}
\tag{B.7}
$$

Our cone-beam CT data typically contain 180 projections at an increment of 2° covering the entire 360° but may not include view angles that correspond exactly to λ_1 and λ_2. While an interpolation of the projection data is possible, our BPF reconstruction was designed to regard the closest projection angles as λ_1 and λ_2

for all Pi-lines. Furthermore, the constant term (P_0) in the integration over x'_π in (B.6) cannot be obtained for planes $z \neq 0$ (Yu et al. 2006). For the reconstruction on an off-midplane, P_0 can be approximated by the mean of the central point from projection λ_1 and λ_2, i.e.

$$P_0 = \frac{1}{2}[P(u_d, v_d, \lambda_1) + P(u_d, v_d, \lambda_2)], \tag{B.8}$$

where $P(u_d, v_d, \lambda_1)$ and $P(u_d, v_d, \lambda_2)$ are the projection of the central point $((x_{\pi 1} + x_{\pi 2})/2, \lambda_1, \lambda_2, z_0)$ from λ_1 and λ_2, respectively. It should also be noted that our reconstruction software treats the integral in the reconstruction algorithm as a Cauchy Principal Value (Yu et al. 2006) by considering only the finite terms. Although the weighted BPF algorithm may be useful in exploiting the redundant data (Yu et al. 2006, Cho et al. 2007, Xia et al. 2010), the BPF reconstruction weighs data from a full range of 2π equally in this work.

B.1.2 BPF reconstruction of synthetically truncated data

The reconstruction algorithms have been implemented on two datasets with contrast materials arranged within the same plane (see Robar et al. (2009)) and stacked off-axis inside a cylindrical water container (see Berman (2010)). The former and latter arrangements are visible in figure B.4a and figure B.4d, respectively. The contrast objects include lung inhale ($\rho = 0.195\,\mathrm{g\,cm^{-3}}$), water-equivalent ($\rho = 1.013\,\mathrm{g\,cm^{-3}}$), trabecular bone ($\rho = 1.161\,\mathrm{g\,cm^{-3}}$) and dense bone ($\rho = 1.609\,\mathrm{g\,cm^{-3}}$) materials. Henceforth, the two arrangements will be referred to as the Quasar[1] phantom and the stacked phantom, respectively. Details on the cone-beam CT imaging system has been previously presented in Robar et al. (2009).

---

[1] http://modusmed.com/multi-purpose-body-qa-phantom

The projection data has a dimension of 768 rows $\times$ 1024 columns. For data truncation, 300 columns on each side of the projections has been manually deleted to correspond to a FOV of 12.5 cm. With the source to detector distance of 130 cm, the projected FOV covered 425 pixels on the imaging panel. Truncated projections for the Quasar and stacked phantoms are shown in figures B.4b and B.4d, respectively. The left column of figure B.4 display the full-field projections. The water container for the stacked phantom has an inner diameter of 21.5 cm (Berman 2010), approximately 42% of which has been truncated. The diameter of the Quasar phantom, however, is only 13 cm. The corresponding truncation is therefore less than 5%.

The truncated projections were reconstruted using the conventional FDK with a Hamming filter (Robar et al. 2009) and the BPF algorithms described in section B.1.1 (Yu et al. 2006, Cho et al. 2007). A slice thickness of 0.3mm was used for all reconstruction. Reconstructed images were calibrated to the the physical density (ρ) in $\mathrm{g\,cm^{-3}}$ and were displayed to show the effects of data truncation on both algorithms. For a more quantitative comparison, the line profiles along the central row (y=0 cm) of slices containing contrast materials as well as uniform slices with water were plotted. Mean profiles across 6 slices were computed for less noisy plots.

B.2 Results

B.2.1 BPF reconstruction of synthetically truncated data

The reconstructed images for the Quasar phantom obtained using the two algorithms from the truncated data are shown in figure B.5. The images were calibrated to the known material densities presented in section B.1.2. It is evident that images obtained using the FDK technique suffer from more severe
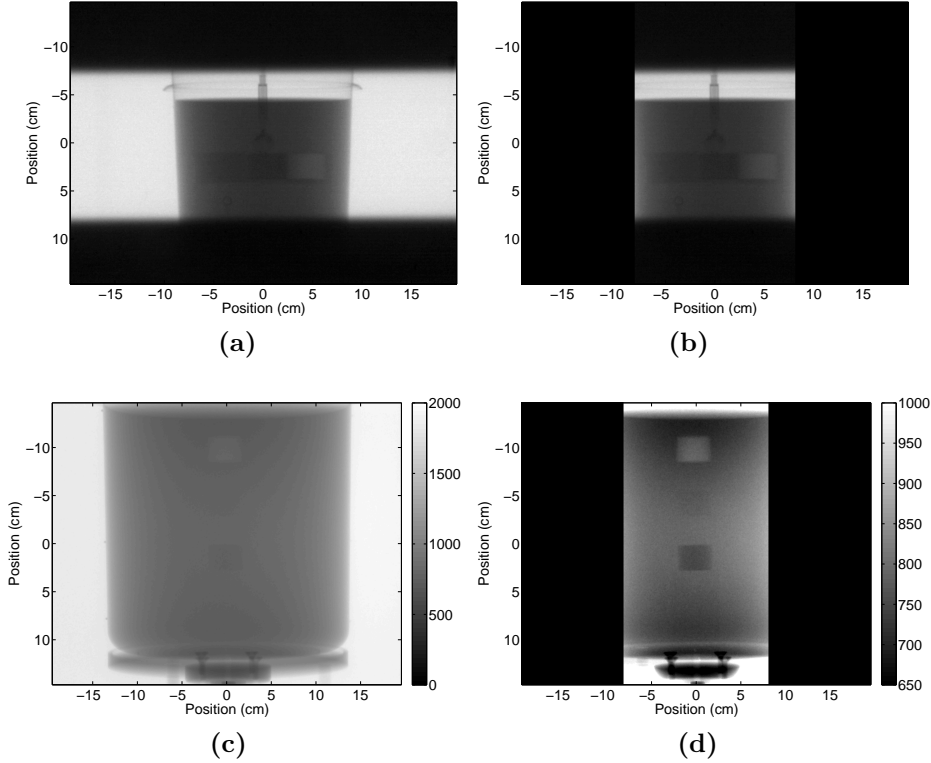
Figure B.4: *Full-field (left) and truncated (right) projections of the Quasar and the stacked phantoms. Both the full-filed and truncated projections of the Quasar phantom have the same display window. The display window for the stacked phantom is adjusted to show the entire water container in the full-field projection and the three materials in the truncated projection. Note the faint trabecular bone cylinder between the dense bone (bottom) and lung inhale (top) materials in (d).*

truncated artefact when compared to the BPF algorithm. The dense bone cylinder at three o'clock and the lung inhale cylinder at six o'clock position are both partially obscured by the dark boundary ring at the edge of the reconstructed FOV as a result of data truncation. An increase in density value is also visible in figure B.6b due to the dense bone contrast material along the profile. Although the profiles agree with negligible differences, it can be seen from figure B.6 that the pixel values by the use of FDK (dotted lines) started to decrease from an earlier position on the x-axis, which corresponds to the wider boundary rings in

figure B.5b and figure B.5d.

The effect of the boundary ring artefact is more pronounced in the reconstructed slices for the stacked phantom due to the more severe data truncation as described in section B.1.2. In the FDK reconstructed slice, the dense bone object is almost completely concealed by the boundary ring. Furthermore, when superimposed on the mean profiles for the uniform slices, an increase in the density value can be clearly seen on the BPF reconstructed profile (circles in figure B.8b), corresponding to the actual object width of 3 cm. Although the pixel values for the FDK reconstructed profile started to increase at the same x-position of 1.2 cm, the width of the dense bone material cannot be accurately identified. Furthermore, an intensity-drop artefact was observed in the reconstruction, as indicated by the decrease in the density values (from negative to positive x positions), especially in figure B.8.

B.3 Discussion

As explained in Cho et al. (2007), the calculation of filtering in the FDK and the BPF algorithms occurs on the detector plane and the backprojected image, respectively. To reconstruct the Pi-line support segment defined in figure B.3, the FDK algorithm requires the FOV to fully encompass the object at any view angles, in order to avoid truncation artefacts in the reconstructed images. In contrast, the projection data is backprojected and subsequently filtered along the PI-line support segments by the BPF reconstruction (see (B.6)). Data truncated with respect to the entire object are therefore sufficient for an exact reconstruction of ROI images using the BPF algorithm, provided the ROI is completely covered by the Pi-line support segments, as illustrated in figure B.9. Only projection of length L_{BPF} is needed at the view angle for the exact reconstruction of the

Figure B.5: *Calibrated slice images of the Quasar phantom reconstructed using BPF (left) and FDK (right) algorithms within the planes with (top) and without (bottom) contrast materials. The display window is $[0\,\mathrm{g\,cm^{-3}},\ 2\,\mathrm{g\,cm^{-3}}]$.*

Pi-line support segment, as a result. As such, the data requirement by the BPF for exact image reconstruction of an ROI can be comparatively smaller than the FDK algorithm. The longer detector length required by the FDK algorithm is indicated by L_{FDK} in figure B.9 to conceptually compare with the shorter L_{BPF}. Reconstructed images obtained using the FDK technique presented in section B.2 thus suffered from more severe truncated artefact when compared to the BPF algorithm.

Artificially truncated both sides of the projection data in this work represented
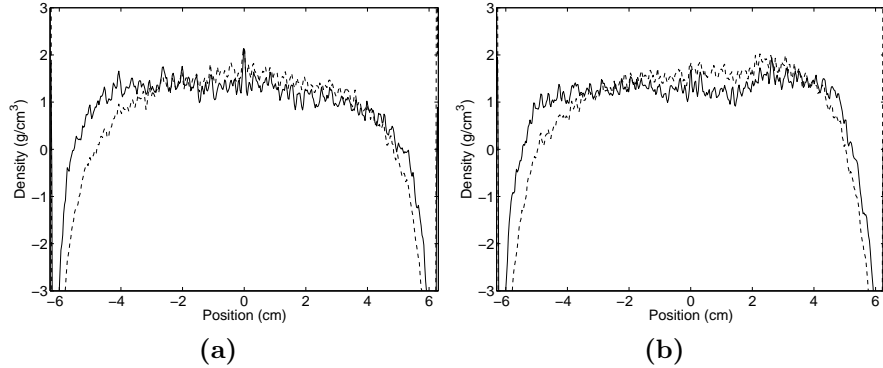
Figure B.6: *Mean profiles along y=0 cm in figure B.5 for the slices (a) without and (b) with the contrast materials. z = 4 cm to 5.8 cm in (a) and 1.6 cm to 3.1 cm in (b). Dotted curve represent the results obtained from FDK algorithm and solid curve from the BPF algorithm.*

an interior problem, for which a mathematically exact reconstruction is impossible (Zhang & Zeng 2007). Nonetheless, the reconstructed images presented in section B.2 are sufficient to demonstrate the benefits of BPF reconstruction over the FDK algorithm. Since the entire truncated projection data in figure B.4b and figure B.4d was reconstructed, the reconstruction ROI for a given plane in this work was as wide as the FOV. It is believed reconstructing an ROI sufficiently encompassed by the FOV, as in figure B.3b, can eliminate the boundary ring artefacts. The interior problem can be avoided by e.g. placing the phantom off-axis and modifying the FOV cylinder to irradiate only the VOI. Furthermore, Zou & et al. (2005) illustrated the reconstruction for a cone-beam CT scan with a varying beam angle, which can be applied on the VOI images obtained using truncated beam modulated by the multi-leaf collimator (MacDonald 2010, Berman 2010). While the truncation artefact can be improved by the use of the BPF algorithm, the calibrated pixel values remain slightly inaccurate when the relative data truncation is large. In figure B.8, the reconstructed densities for the stacked phantom show larger deviations from the true density values for the uniform slice as well as
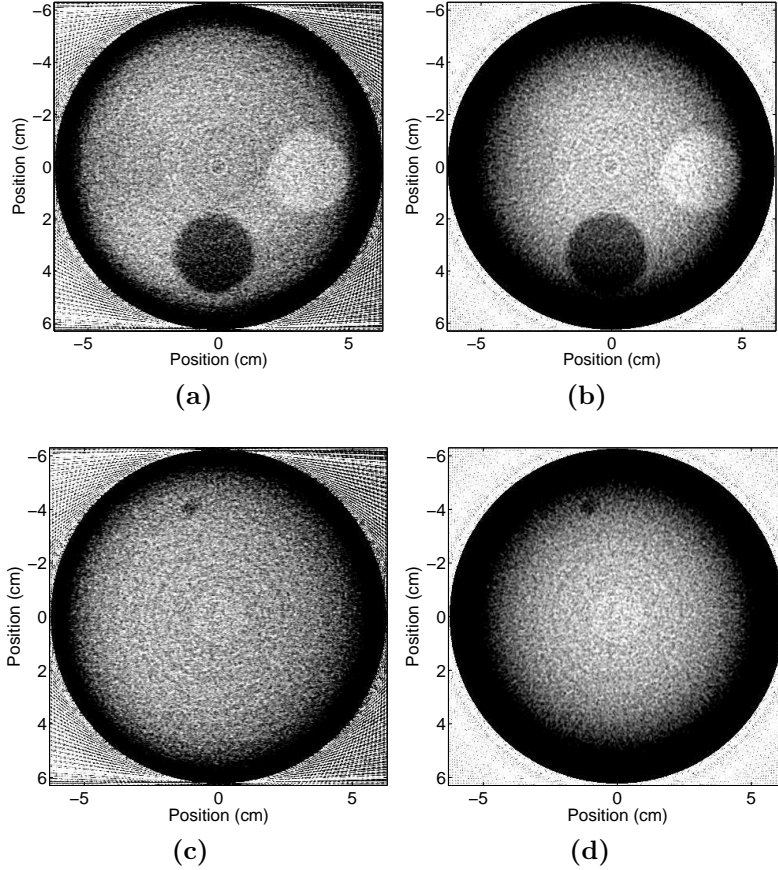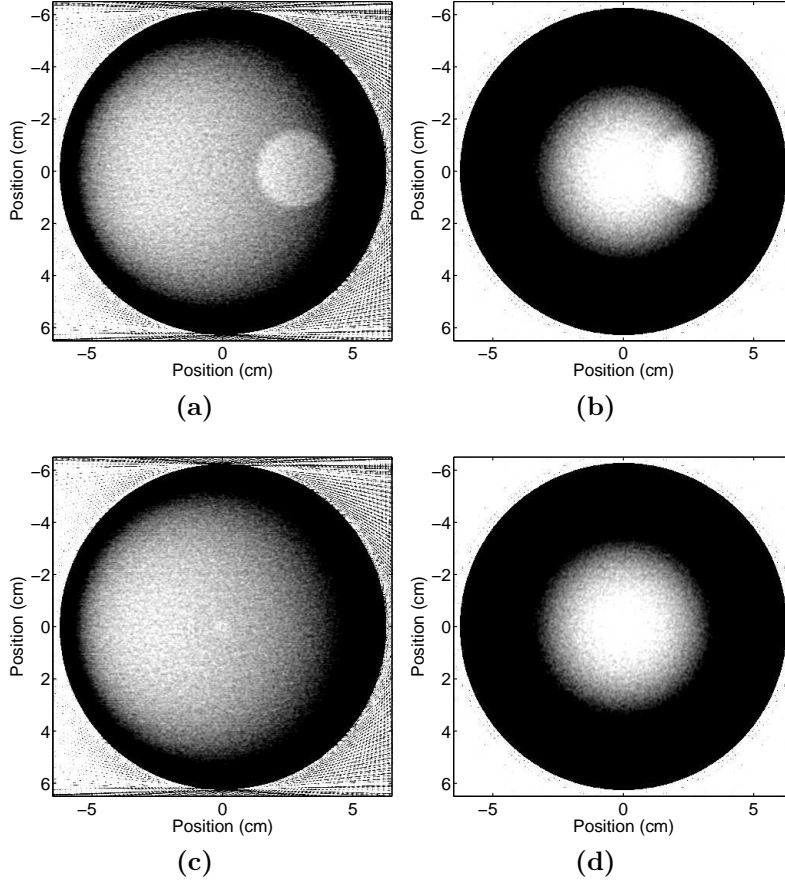
Figure B.7: *Calibrated slice images of the stacked phantom reconstructed using
BPF (left) and FDK (right) algorithms within the planes with (top) and without
(bottom) the dense bone material. The display window is $[0\,\mathrm{g\,cm^{-3}},\, 2\,\mathrm{g\,cm^{-3}}]$.*

the dense bone VOI, due to the comparatively larger data truncation of 42% (c.f.
5% for the Quasar phantom), as mentioned in section B.1.2. The mean profiles
for the Quasar phantom in figure B.6 generally show more accurate reconstructed
density.

It can be also seen from (B.7) that the numerical calculation of the backpro-
jection process in the BPF algorithm contains a spatially varying weighting factor
$(1/[\vec{r'} - r(\vec{\lambda})])$. The integral over x'_π in obtaining the image on a Pi-line leads to
brighter pixels on the upper section and conversely darker lower sections in Yu

Figure B.8: *(a) Mean profiles along y=0 cm in figure B.7 for the slices without the dense bone object ($z = -0.5$ cm to 2.0 cm). Dotted curve represent the results obtained from FDK algorithm and solid curve from the BPF algorithm. (b) A bump is apparent in each of the mean profiles for the slices containing dense bone ($z = 0.7$ cm to 2.2 cm). Profiles in (a) are superimposed in (b) for comparisons. Crosses and circles represent results for FDK and BPF, respectively.*
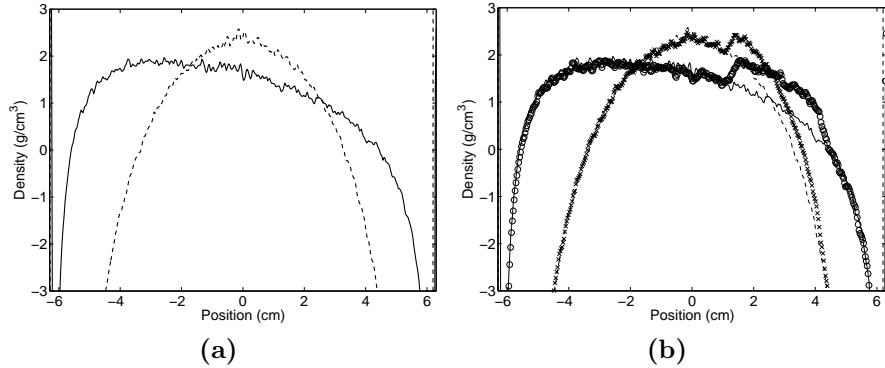
et al.'s (2006) BPF reconstructed images. The reconstructed images and profiles for the stacked phantoms were moderately affected by the same transition, apparent from positive to negative x-positions in figure B.7a and figure B.7c. The BPF backprojection technique with a spatially constant weighting factor proposed by Xia et al. (2010), may be applied to obtain images with less intensity-drop artefacts.

B.4 Concluding remarks

The BPF reconstruction algorithm has been implemented in Matlab based on the work of Yu et al.'s (2006) and Cho et al.'s (2007). When compared to the conventional FDK algorithm, the BPF reconstruction technique shows a reduction of truncation artefacts. Specifically, the size of the boundary ring at the edge of reconstructed FOV was reduced. The calibrated pixel values largely correspond to the true physical densities of the contrast materials. For a more severe trunca-
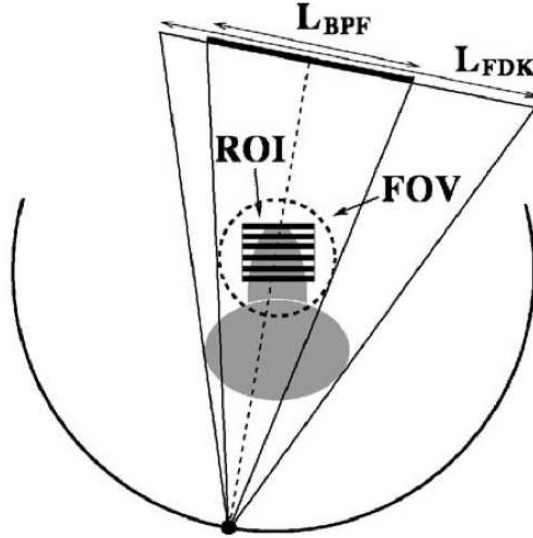
Figure B.9: *A comparison of the data requirement for the BPF and the FDK algorithms (Cho et al. 2007). To reconstruct the ROI defined in figure B.3, the FDK algorithm requires the FOV to fully encompass the object and data of detector length L_{FDK} is needed at every view angle. In contrast, only data from a shorter length of L_{BPF} is required to cover the projection of the support segments needed by the BPF algorithm. The FDK reconstruction thus suffered from more severe truncated artefact when compared to the BPF algorithm, as presented by the reconstructed images in section B.2.*

tion in the projection domain (more than 40% of the data truncated), while the mean profiles for both reconstruction algorithms show deviations from the actual densities, the line profiles obtained from the BPF reconstruction reveals an accurate width of the contrast object. The line profiles from the FDK reconstruction started to increase at the same location but do not demonstrate the true width of the contrast material due to the larger boundary ring.

This work was conducted as an additional project, which came about after the temporary closure of the University of Canterbury as a result of the Canterbury earthquakes. While it has not been implemented in spectral CT, it may be potentially beneficial when the projections were truncated as a result of smaller

detector sizes of the current PCD, e.g. the Medipix detector.

Synthetically truncating the FOV to be as wide as the reconstruction ROI in this work introduced an interior reconstruction problem (Zhang & Zeng 2007). Reconstructing a ROI entirely encompassed by the FOV cylinder but not within the object using our BPF reconstruction (see figure B.3b) is expected to reduce the boundary ring and to negate the interior problem. Furthermore, the implemented reconstruction algorithm may be optimised by considering different weighting schemes. In particular, the intensity-drop artefacts can be improved upon realising a backprojection without a spatially varying weighting factor (Xia et al. 2010). Data redundancy over a full scan can also be exploited using a weighted BPF algorithm.

References

Aamir R, Anderson N, Butler A, Butler P, Lansley S, Doesburg R, Walsh M & Mohr J 2011a Characterization of Si and CdTe sensor layers in Medipix assemblies using a microfocus x-ray source *IEEE Nuclear Science Symposium and Medical Imaging Conference, 2011* pp. 4766 – 4769.

Aamir R, Lansley S, Zainon R, Fiederle M, Fauler A, Greiffenberg D, Butler A & Butler P 2011b Pixel sensitivity variations in a CdTe-Medipix2 detector using poly-energetic x-rays *Journal of Instrumentation* **6**(01), C01059.

Alessio A M & MacDonald L R 2013 Quantitative material characterization from multi-energy photon counting ct *Medical Physics* **40**, 031108.

Alvarez R E 2010 Near optimal energy selective x-ray imaging system performance with simple detectors *Medical Physics* **37**(2), 822–841.

Alvarez R E 2011 Estimator for photon counting energy selective x-ray imaging with multibin pulse height analysis *Medical Physics* **38**(5), 2324–2334.

Alvarez R E & Macovski A 1976 Energy-selective reconstructions in x-ray computerised tomography *Physics in Medicine and Biology* **21**(5), 733–744.

Anderson N, Butler A, Scott N, Cook N, Butzer J, Schleich N, Firsching M, Grasset R, de Ruiter N, Campbell M & Butler P 2010 Spectroscopic (multi-energy) CT distinguishes iodine and barium contrast material in MICE *European Radiology* **20**(9), 2126–2134.

Ballabriga R 2009 The Design and Implementation in 0.13 micron CMOS of an Algorithm Permitting Spectroscopic Imaging with High Spatial Resolution for Hybrid Pixel Detectors, *PhD thesis* Ramon Llull University, Barcelona, Spain.

Ballabriga R, Alozy J, Blaj G, Campbell M, Fiederle M, Frojdh E, Heijne E, Llopart X, Pichotka M, Procz S, Tlustos L & Wong W 2012 The Medipix3RX: a high resolution, zero dead-time pixel detector readout chip allowing spectroscopic imaging *Journal of Instrumentation* **8**(02), C02016.

Ballabriga R, Blaj G, Campbell M, Fiederle M, Greiffenberg D, Heijne E, Llopart X, Plackett R, Procz S, Tlustos L, Turecek D & Wong W 2011b Characterization of the Medipix3 pixel readout chip *Journal of Instrumentation* **6**(01), C01052.

Ballabriga R, Campbell M, Heijne E, Llopart X, Tlustos L & Wong W 2011a Medipix3: A 64k pixel detector readout chip working in single photon counting mode with improved spectrometric performance *Nuclear Instruments and Methods in Physics Research Section A: Accelerators, Spectrometers, Detectors and Associated Equipment* **633**, S15–S18.

Bazalova M, Jean-Francois C, Beaulieu L & Verhaegen F 2008 Dual-energy CT-based material extraction for tissue segmentation in Monte Carlo dose calculations *Physics in Medicine and Biology* **52**(9), 2439–2456.

Bazalova M & Verhaegen F 2007 Monte Carlo simulation of a computed tomography x-ray tube *Physics in Medicine and Biology* **52**(19), 5945–5955.

Bazalova M, Yu K, Pratx G & Lei X 2012 Investigation of x-ray fluorescence computed tomography (XFCT) and k-edge imaging *IEEE Transactions on Medical Imaging* **31**(8), 1620–1627.

Bech M, Bunk O, David C, Kraft P, Brönnimann C, Eikenberry E & Pfeiffer F 2008 X-ray imaging with the PILATUS 100k detector *Applied Radiation and Isotopes* **66**(4), 474–478.

Berger M, Hubbell J, Seltzer S, Chang J, Coursey J, Sukumar R & Zucker D 2005 'XCOM: Photon Cross Section Database (version 1.3)'. National Institute of Standards and Technology (Gaithersburg, MD, USA).

Berman A 2010 VOI CBCT Progress *Technical report* Department of Physics and Atmospheric Science, Dalhousie University, Halifax, Nova Scotia, Canada.

Bones P J, Butler A P H, Ronaldson J P & Opie A M T 2010 Development of a CT scanner based on the Medipix family of detectors *Proceedings of SPIE* **7804**, 12–16.

REFERENCES

Boone J M 2002 Normalized glandular dose (DgN) coefficients for arbitrary x-ray spectra in mammography: Computer-fit values of Monte Carlo derived data *Medical Physics* **29**(5), 869–875.

Boone J M & Seibert J A 1997 An accurate method for computer-generating tungsten anode x-ray spectra from 30 to 140 kV *Medical Physics* **24**(11), 1661–1670.

Bornefalk H 2012 Xcom intrinsic dimensionality for low-z elements at diagnostic energies *Medical Physics* **39**(2), 654–657.

Bornefalk H & Danielsson M 2010 Photon-counting spectral computed tomography using silicon strip detectors: a feasibility study *Physics in Medicine and Biology* **55**(7), 1999–2022.

BreastScreen Aotearoa 2013 Private communication. via Executive Assistant of BreastScreen Aotearoa
http://www.nsu.govt.nz/current-nsu-programmes/breastscreen-aotearoa.aspx.

Broennimann C, Eikenberry E F, Henrich B, Horisberger R, Huelsen G, Pohl E, Schmitt B, Schulze-Briese C, Suzuki M, Tomizaki T, Toyokawa H & Wagner A 2006 The PILATUS 1M detector *Journal of Synchrotron Radiation* **13**(2), 120–130.

Brown F B 2003 MCNP general Monte Carlo N-particle transport code, version 5 *Technical report* Los Alamos, NM: Los Alamos National Laboratory.

Bushberg J T, Seibert J A, Leidholdt E M J, Boone J M & Goldschmidt E J J 2003 *The Essential Physics of Medical Imaging* Lippincott Williams & Wilkins (Baltimore, MD).

Butler A, Anderson N, Tipples R, Cook N, Watts R, Meyer J, Bell A, Melzer T & Butler P H 2008 Bio-medical X-ray imaging with spectroscopic pixel detectors *Nuclear Instruments and Methods in Physics Research Section A: Accelerators, Spectrometers, Detectors and Associated Equipment* **591**, 141–146.

Campbell M, Heijne E, Meddeler G, Pernigotti E & Snoeys W 1998 A readout chip for a 64× 64 pixel matrix with 15-bit single photon counting *IEEE Transactions on Nuclear Science* **45**(3), 751–753.

Cho S, Junguo B, Charles A P, Chin-Tu C, Tong-Chuan H & Xiaochuan P 2007 Region-of-interest image reconstruction in circular cone-beam microCT *Medical Physics* **34**, 4923–4933.

Cormack A 1963 Representation of a function by its line integrals, with some radiological applications *Journal of Applied Physics* **34**(9), 2722–2727.

Currie B E 2007 Monte Carlo investigation into superficial cancer treatments of the head and neck, *Master's thesis* Department of Physics and Astronomy, University of Canterbury, Christchurch, New Zealand.

Danielsson M 2012 Philips microdose mammography - the technology and physics behind the first fda approved photon counting x-ray imaging system *Medical Physics* **39**(6), 4017–4017.

Delpierre P, Berar J F, Blanquart L, Boudet N, Breugnon P, Caillot B, Clemens J C, Mouget C, Potheau R & Valin I 2002 Large surface x-ray pixel detector *IEEE Transactions on Nuclear Science* **49**(4), 1709–1711.

Deslattes R, Kessler Jr. E, Indelicato P, de Billy L, Lindroth E, Anton J, Coursey J, Schwab D, Chang C, Sukumar R, Olsen K & Dragoset R 2005 'X-ray Transition Energies (version 1.2)'. Available online at
http://www.nist.gov/physlab/data/xraytrans/index.cfm Accessed: 2010-05-11.

Dierick M, Masschaele B & Hoorebeke L V 2004 Octopus, a fast and user-friendly tomographic reconstruction package developed in LabView® *Measurement Science and Technology* **15**(7), 1366–1370.

Ding H & Molloi S 2012 Quantification of breast density with spectral mammography based on a scanned multi-slit photon-counting detector: a feasibility study *Physics in Medicine and Biology* **57**(15), 4719–4738.

Doesburg R M N 2012 The MARS Photon Processing Cameras for Spectral CT, *PhD thesis* Department of Physics and Astronomy, University of Canterbury, Christchurch, New Zealand.

Doesburg R M N, Koenig T, Nik S J, Bell S T, Ronaldson J P, Walsh M F, Butler A P H & Butler P H 2012 Spectrum measurement using Medipix3 in Charge Summing Mode *Journal of Instrumentation* **7**(11), C11004.

Ducote J, Alivov Y & Molloi S 2011 Imaging of nanoparticles with dual-energy computed tomography *Physics in Medicine and Biology* **56**(7), 2031–2044.

Edling F, Bingefors N, Brenner R, Fransson K, Gustafsson L, del Risco Norrlid L & Rönnqvist C 2004 Characterisation of a pixel readout chip for medical x-ray imag-

REFERENCES

ing *Nuclear Instruments and Methods in Physics Research Section A: Accelerators, Spectrometers, Detectors and Associated Equipment* **525**(1), 217–220.

Feldkamp L A, Davis L C & Kress J W 1984 Practical cone-beam algorithm *Journal of the Optical Society of America A* **1**, 612–619.

Firsching M, Butler A P, Scott N, Anderson N G, Michel T & Anton G 2009 Contrast agent recognition in small animal CT using the Medipix2 detector *Nuclear Instruments and Methods in Physics Research Section A: Accelerators, Spectrometers, Detectors and Associated Equipment* **607**(1), 179–182.

Firsching M, Niederlöhner D, Michel T & Anton G 2006 Quantitative material reconstruction in CT with spectroscopic x-ray pixel detectors - a simulation study *IEEE Nuclear Science Symposium Conference Record, 2006* **4**, 2257–2259.

Flohr T G, McCollough C H, Bruder H, Petersilka M, Gruber K, Süß C, Grasruck M, Stierstorfer K, Krauss B, Raupach R, Primak A, Küttner A, Achenbach S, Becker C, Kopp A & Ohnesorge B 2006 First performance evaluation of a Dual-Source CT (DSCT) system *European Radiology* **16**(2), 256–268.

Fredenberg E, Lundqvist M, Cederström B, Åslund M & Danielsson M 2010 Energy resolution of a photon-counting silicon strip detector *Nuclear Instruments and Methods in Physics Research Section A: Accelerators, Spectrometers, Detectors and Associated Equipment* **613**(1), 156–162.

Frey E C, Wang X, Du Y, Taguchi K, Xu J & Tsui B M W 2007 Investigation of the use of photon counting x-ray detectors with energy discrimination capability for material decomposition in micro-computed tomography *Proceedings of SPIE* **6510**, 65100A.

Gammex Inc. 1997 '156 mammographic accreditation phantom users guide'. Gammex Inc, Middleton, WI, USA.

Giersch J, Firsching M, Niederlöhner D & Anton G 2005 Material reconstruction with spectroscopic pixel x-ray detectors *Nuclear Instruments and Methods in Physics Research Section A: Accelerators, Spectrometers, Detectors and Associated Equipment* **546**(1-2), 125–130.

Giersch J, Niederlöhner D & Anton G 2004 The influence of energy weighting on x-ray imaging quality *Nuclear Instruments and Methods in Physics Research Section A: Accelerators, Spectrometers, Detectors and Associated Equipment* **531**(1), 68–74.

Giersch J, Weidemann A & Anton G 2003 Rosi–an object-oriented and parallel-computing monte carlo simulation for x-ray imaging *Nuclear Instruments and Methods in Physics Research Section A: Accelerators, Spectrometers, Detectors and Associated Equipment* **509**(1-3), 151–156.

Gimenez E N, Ballabriga R, Campbell M, Horswell I, Llopart X, Marchal J, Sawhney K J S, Tartoni N & Turecek D 2011 Characterization of Medipix3 with synchrotron radiation *IEEE Transactions on Nuclear Science* **58**(1), 323–332.

Graser A, Johnson T, Chandarana H & Macari M 2009 Dual energy CT: preliminary observations and potential clinical applications in the abdomen *European Radiology* **19**(1), 13–23.

Grasruck M, Kappler S, Reinwand M & Stierstorfer K 2009 Dual energy with dual source CT and kVp switching with single source CT: a comparison of dual energy performance *Proceedings of SPIE* **7258**(2), 72583R.

Heismann B, Schmidt B & Flohr T 2012 *Spectral Computed Tomography* SPIE Press Book (Bellingham, WA, USA).

Hounsfield G 1973 Computerized transverse axial scanning (tomography): Part 1. description of system *British Journal of Radiology* **46**(552), 1016–1022.

Hubbell J & Seltzer S 1996 'Tables of X-Ray Mass Attenuation Coefficients and Mass Energy-Absorption Coefficients from 1 keV to 20 MeV for Elements Z = 1 to 92 and 48 Additional Substances of Dosimetric Interest'. Available online at http://www.nist.gov/pml/data/xraycoef/index.cfm. Accessed: 2012-09-29.

ICRU 1989 *Tissue Substitutes in Radiation Dosimetry and Measurement, Report 44* International Commission on Radiation Units and Measurements (Bethesda, MD, USA).

James F 2006 *Statistical methods in experimental physics* World Scientific Publishing (Singapore).

Johns H & Cunningham J 1983 *The physics of radiology* Charles C. Thomas (Springfield, IL, USA).

Johns P C, Drost D J, Yaffe M J & Fenster A 1985 Dual-energy mammography: Initial experimental results *Medical Physics* **12**, 297–284.

REFERENCES

Johns P C & Yaffe M J 1985 Theoretical optimization of dual-energy x-ray imaging with application to mammography. *Medical Physics* **12**(3), 289–296.

Johnson T, Fink C, Schönberg S & Reiser M 2010 *Dual energy CT in clinical practice* Springer-Verlag (Berlin and Heidelberg, Germany).

Johnson T, Krauβ B, Sedlmair M, Grasruck M, Bruder H, Morhard D, Fink C, Weckbach S, Lenhard M, Schmidt B, Flohr T, Reiser M & Becker C 2007 Material differentiation by dual energy CT: initial experience *European Radiology* **17**(6), 1510–1517.

Kalender W 2006 X-ray computed tomography *Physics in Medicine and Biology* **51**(13), R29–R43.

Kalender W A, Perman W H, Vetter J R & Klotz E 1986 Evaluation of a prototype dual-energy computed tomographic apparatus. I. Phantom studies *Medical Physics* **13**(3), 334–339.

Kawrakow I, Mainegra-Hing E, Rogers D, Tessier F & Walters B 2011 'The EGSnrc code system: Monte Carlo simulation of electron and photon transport'. NRCC Report PIRS-701, National Research Council of Canada.

Kawrakow I, Mainegra-Hing E & Rogers D W O 2006 'EGSnrcMP: the multi-platform environment for EGSnrc'. NRCC Report PIRS-877, National Research Council of Canada.

Kirkpatrick S 1984 Optimization by simulated annealing: quantitative studies *Journal of Statistical Physics* **34**(5), 975–986.

Koenig T, Schulze J, Zuber M, Rink K, Butzer J, Hamann E, Cecilia A, Zwerger A, Fauler A, Fiederle M & Oelfke U 2012 Imaging properties of small-pixel spectroscopic x-ray detectors based on cadmium telluride sensors *Physics in Medicine and Biology* **57**(21), 6743–6759.

Krüger H, Fink J, Kraft E, Wermes N, Fischer P, Peric I, Herrmann C, Overdick M & Rütten W 2008 CIX: a detector for spectrally enhanced x-ray imaging by simultaneous counting and integrating *Proceedings of SPIE* **6913**, 69130P.

Lagarias, Jeffrey C, Reeds, James A, Wright, Margaret H & Wright, Paul E 1998 Convergence properties of the Nelder–Mead simplex method in low dimensions *SIAM Journal on Optimization* **9**(1), 112–147.

Le H Q & Molloi S 2010 Least squares parameter estimation methods for material decomposition with energy discriminating detectors *Medical Physics* **38**(1), 245–255.

Le H Q & Molloi S 2011 Segmentation and quantification of materials with energy discriminating computed tomography: A phantom study *Medical Physics* **38**, 228.

Lehmann L A, Alvarez R E, Macovski A, Brody W R, Pelc N J, Riederer S J & Hall A L 1981 Generalized image combinations in dual kVp digital radiography *Medical Physics* **8**(5), 659–667.

Lemacks M R, Kappadath S C, Shaw C C, Liu X & Whitman G J 2002 A dual-energy subtraction technique for microcalcification imaging in digital mammographya signal-to-noise analysis *Medical Physics* **29**, 1739–1751.

Leng S, Yu L, Wang J, Fletcher J G, Mistretta C A & McCollough C H 2011 Noise reduction in spectral CT: Reducing dose and breaking the trade-off between image noise and energy bin selection *Medical Physics* **38**(9), 4946–4957.

Lindner M, Blanquart L, Fischer P, Krüger H & Wermes N 2001 Medical x-ray imaging with energy windowing *Nuclear Instruments and Methods in Physics Research Section A: Accelerators, Spectrometers, Detectors and Associated Equipment* **465**(1), 229–234.

Liu X, Yu L, Primak A N & McCollough C H 2009 Quantitative imaging of element composition and mass fraction using dual-energy CT: three-material decomposition *Medical Physics* **36**(5), 1602–1609.

Llopart X 2007 Design and Characterization of 64K Pixels Chips Working in Single Photon Processing Mode, *PhD thesis* Mid Sweden University, Sundsvall, Sweden.

Llopart X, Campbell M, Dinapoli R, San Segundo D & Pernigotti E 2002 Medipix2: A 64-k pixel readout chip with 55μm square elements working in single photon counting mode *IEEE Transactions on Nuclear Science* **49**(5), 2279–2283.

Ma C M & Rogers D W O 2009 'BEAMDP as a general-purpose utility'. NRC Report PIRS-0509(revA), National Research Council of Canada.

MacDonald A O 2010 Investigation of Volume-of-Interest Megavoltage Cone-beam CT, *Master's thesis* Department of Physics and Atmospheric Science, Dalhousie University, Halifax, Nova Scotia, Canada.

REFERENCES

Macovski A 1983 *Medical imaging systems* Prentice-Hall (Englewood Cliffs, New Jersey, USA).

McCollough C H, Primak A N, Braun N, Kofler J, Yu L & Christner J 2009 Strategies for reducing radiation dose in CT *Radiologic Clinics of North America* **47**(1), 27–40.

McCullough E 1975 Photon attenuation in computed tomography *Medical Physics* **2**(6), 307–320.

Mettler F A J, Thomadsen B R, Bhargavan M, Gilley D B, Gray J E, Lipoti J A, McCrohan J, Yoshizumi T T & Mahesh M 2008 Medical radiation exposure in the US in 2006: preliminary results *Health Physics* **95**(5), 502–507.

Meyer P, Buffard E, Mertz L, Kennel C, Constantinesco A & Siffert P 2004 Evaluation of the use of six diagnostic x-ray spectra computer codes *British Journal of Radiology* **77**, 224–230.

Niederlöhner D, Karg J, Giersch J & Anton G 2005 The energy weighting technique: measurements and simulations *Nuclear Instruments and Methods in Physics Research Section A: Accelerators, Spectrometers, Detectors and Associated Equipment* **546**(1), 37–41.

Nik S J, Meyer J & Watts R 2011 Optimal material discrimination using spectral x-ray imaging *Physics in Medicine and Biology* **56**(18), 5969–5983.

Nik S J, Thing R S, Watts R, Dale T, Currie B & Meyer J 2013 ' Optimal material discrimination using spectral x-ray imaging: Monte Carlo validation and application to mammography'. In preparation.

Nik S, Thing R, Watts R & Meyer J 2012 SU-D-218-05: Material quantification in spectral x-ray imaging: Optimization and validation *Medical Physics* **39**(6), 3623.

Ogawa K, Nakajima M & Yuta S 1984 A reconstruction algorithm from truncated projections *IEEE Transactions on Medical Imaging* **3**(1), 34–40.

Overdick M, Baumer C, Engel K, Fink J, Herrmann C, Kruger H, Simon M, Steadman R & Zeitler G 2009 Status of direct conversion detectors for medical imaging with x-rays *IEEE Transactions on Nuclear Science* **56**(4), 1800–1809.

Pangaud P, Basolo S, Boudet N, Berar J F c, Chantepie B, Delpierre P, Dinkespiler B, Hustache S, Menouni M & Morel C 2007 XPAD3: A new photon counting chip

for x-ray CT-scanner *Nuclear Instruments and Methods in Physics Research Section A: Accelerators, Spectrometers, Detectors and Associated Equipment* **571**(1-2), 321–324.

Pfeiffer K F 2004 Evaluation of the Medipix detectors for medical X-ray imaging, with special consideration of mammography *PhD thesis* Friedrich-Alexander-Universität Erlangen-Nürnberg.

Procz S, Lubke J, Zwerger A, Mix M & Fiederle M 2009 Optimization of Medipix-2 threshold masks for spectroscopic x-ray imaging *IEEE Transactions on Nuclear Science* **56**(4), 1795–1799.

Rencher A C 1995 *Methods of Multivariate Analysis* Wiley (Hoboken, New Jersey, USA).

Riederer S & Mistretta C 1977 Selective iodine imaging using K-edge energies in computerized x-ray tomography *Medical Physics* **4**(6), 474–481.

Robar J L, Connell T, Huang W & Kelly R G 2009 Megavoltage planar and cone-beam imaging with low-Z targets: Dependence of image quality improvement on beam energy and patient separation *Medical Physics* **36**, 3955–3963.

Roessl E, Brendel B, Engel K J, Schlomka J P, Thran A & Proksa R 2011 Sensitivity of photon-counting based k-edge imaging in x-ray computed tomography *IEEE Transactions on Medical Imaging* **30**(9), 1678–1690.

Roessl E, Cormode D, Brendel B, Jürgen Engel K, Martens G, Thran A, Fayad Z & Proksa R 2010 Preclinical spectral computed tomography of gold nano-particles *Nuclear Instruments and Methods in Physics Research Section A: Accelerators, Spectrometers, Detectors and Associated Equipment* **648**, S259–S264.

Roessl E & Herrmann C 2009 Cramér-Rao lower bound of basis image noise in multiple-energy x-ray imaging *Physics in Medicine and Biology* **54**(5), 1307–18.

Roessl E & Proksa R 2006 Optimal energy threshold arrangement in photon-counting spectral x-ray imaging *IEEE Nuclear Science Symposium Conference Record, 2006* **3**, 1950–1954.

Roessl E & Proksa R 2007 K-edge imaging in x-ray computed tomography using multi-bin photon counting detectors *Physics in Medicine and Biology* **52**(15), 4679–4696.

REFERENCES

Rogers D W O 2006 Fifty years of Monte Carlo simulations for medical physics *Physics in Medicine and Biology* **51**(13), R287–R301.

Rogers D W O, Faddegon B A, Ding G X, Ma C M, We J & Mackie T R 1995 BEAM: A Monte Carlo code to simulate radiotherapy treatment units *Medical Physics* **22**(5), 503–524.

Rogers D W O, Walters B R & Kawrakow I 2004 'BEAMnrc users manual'. NRC Report PIRS-0509(revK), National Research Council of Canada.

Ronaldson J P 2012 Quantitative soft-tissue imaging by spectral CT with Medipix3, *PhD thesis* Centre for Bioengineering and Nanomedicine, University of Otago, Christchurch, New Zealand.

Ronaldson J P, Walsh M, Nik S J, Donaldson J, Doesburg R M N, Leeuwen D v, Ballabriga R, Clyne M N, Butler A P H & Butler P H 2011 Characterization of Medipix3 with the mars readout and software *Journal of Instrumentation* **6**(01), C01056.

Ronaldson J, Zainon R, Scott N, Gieseg S, Butler A, Butler P & Anderson N 2012 Toward quantifying the composition of soft tissues by spectral CT with Medipix3 *Medical Physics* **39**, 6847–6857.

Rose A 1946 A unified approach to the performance of photographic film, television pickup tubes, and the human eye *Journal of the Society of Motion Picture Engineers* **47**(4), 273–294.

Schlomka J P, Roessl E, Dorscheid R, Dill S, Martens G, Istel T, Baumer C, Herrmann C, Steadman R, Zeitler G, Livne A & Proksa R 2008 Experimental feasibility of multi-energy photon-counting K-edge imaging in pre-clinical computed tomography *Physics in Medicine and Biology* **53**(15), 4031–4037.

Shikhaliev P 2005 Beam hardening artefacts in computed tomography with photon counting, charge integrating and energy weighting detectors: a simulation study *Physics in Medicine and Biology* **50**(24), 5813–5827.

Shikhaliev P M 2006 Tilted angle CZT detector for photon counting/energy weighting x-ray and CT imaging *Physics in Medicine and Biology* **51**(17), 4267–4287.

Shikhaliev P M 2008*a* Computed tomography with energy-resolved detection: a feasibility study *Physics in Medicine and Biology* **53**(5), 1475–1495.

Shikhaliev P M 2008*b* Energy-resolved computed tomography: first experimental results *Physics in Medicine and Biology* **53**(20), 5595–5613.

Shikhaliev P M & Fritz S G 2011 Photon counting spectral CT versus conventional CT: comparative evaluation for breast imaging application *Physics in Medicine and Biology* **56**(7), 1905–1930.

Slaney M & Kak A 2001 *Principles of computerized tomographic imaging* Society of Industrial and Applied Mathematics (Philadelphia, PA, USA).

Slovis T 2003 Children, computed tomography radiation dose, and the As Low As Reasonably Achievable (ALARA) concept *Pediatrics* **112**(4), 971–972.

Steadman R, Herrmann C, Mülhens O & Maeding D 2011 ChromAIX: Fast photon-counting ASIC for spectral computed tomography *Nuclear Instruments and Methods in Physics Research Section A: Accelerators, Spectrometers, Detectors and Associated Equipment* **648**, S211–S215.

Stirling G 2013 Unpublished survey.

Stirling G & Cotterill A 2009 Computed tomography in diagnostic radiology: a survey of use and patient doses for New Zealand, 2007 *Technical report* National Radiation Laboratory.

Sukovle P & Clinthorne N 1999 Basis material decomposition using triple-energy x-ray computed tomography *Proceedings of the 16th IEEE Instrumentation and Measurement Technology Conference* **3**, 1615–1618.

Taguchi K, Frey E C, Wang X, Iwanczyk J S & Barber W C 2010 An analytical model of the effects of pulse pileup on the energy spectrum recorded by energy resolved photon counting x-ray detectors *Medical Physics* **37**(8), 3957–3969.

Tang N D, de Ruiter N, Mohr J, Butler A, Butler P & Aamir R 2012 Using algebraic reconstruction in computed tomography *Proceedings of the 27th Conference on Image and Vision Computing New Zealand* pp. 216–221.

Tapiovaara M J & Wagner R 1985 SNR and DQE analysis of broad spectrum X-ray imaging *Physics in Medicine and Biology* **30**(6), 519–529.

Thing R S 2010 Simulation of energy selective x-ray projection data for material discrimination *Technical report* Department of Physics and Astronomy, University of Canterbury, Christchurch, New Zealand.

REFERENCES

Thing R S 2013 Monte carlo simulation of cone beam computed tomography imaging, *Master's thesis* Department of Physics, Chemistry and Pharmacy, University of Southern Denmark, Odense, Denmark.

Thing R S, Nik S, Currie B, Dale T, Watts R & Meyer J 2011 A virtual spectral CT scanner *Australasian Physical & Engineering Sciences in Medicine* **34**, 123–124.

Tlustos L, Ballabriga R, Campbell M, Heijne E, Kincade K, Llopart X & Stejskal P 2006 Imaging properties of the Medipix2 system exploiting single and dual energy thresholds *IEEE Transactions on Nuclear Science* **53**(1), 367– 372.

Treurniet J R, Walters B R, Kawrakow I & Rogers D W O 2009 'BEAMnrc, DOSXYZnrc and BEAMDP GUI user's manual'. NRCC Report PIRS-0623(rev C), National Research Council of Canada.

Tucker D M, Barnes G T & Chakraborty D P 1991 Semiempirical model for generating tungsten target x-ray spectra *Medical Physics* **18**(2), 211–218.

Tucker D M, Barnes G T & Wu X 1991 Molybdenum target x-ray spectra: a semiempirical model *Medical Physics* **18**(3), 402–407.

Walsh M, Doesburg R, Mohr J, Ballabriga R, Butler A & Butler P 2011b Improving and characterising the threshold equalisation process for multi-chip Medipix3 cameras in Single Pixel Mode *IEEE Nuclear Science Symposium and Medical Imaging Conference, 2011* pp. 1718 –1721.

Walsh M F, Nik S J, Procz S, Pichotkac M, Bell S T, Doesburg R M N, De Ruiter N, Bateman C J, Chernoglazove A I, Panta R K, Butler A P H & Butler P H 2013 Spectroscopic CT data acquisition with Medipix3.1 *Journal of Instrumentation* . Preprint.

Walsh M F, Opie A M T, Ronaldson J P, Doesburg R M N, Nik S J, Mohr J L, Ballabriga R, Butler A P H & Butler P H 2011a First CT using Medipix3 and the MARS-CT-3 spectral scanner *Journal of Instrumentation* **6**(01), C01095.

Wang A S, Harrison D, Lobastov V & Tkaczyk J E 2011 Pulse pileup statistics for energy discriminating photon counting x-ray detectors *Medical Physics* **38**, 4265– 4275.

Wang A S & Pelc N J 2011 Sufficient statistics as a generalization of binning in spectral x-ray imaging *IEEE Transactions on Medical Imaging* **30**(1), 84–93.

Weigel M, Vollmar S V & Kalender W A 2011 Spectral optimization for dedicated breast CT *Medical Physics* **38**(1), 114–124.

Wiegert J, Engel K J & Herrmann C 2009 Impact of scattered radiation on spectral CT *Proceedings of SPIE* **7258**, 72583X.

Xia D, Cho S & Pan X 2010 Backprojection-filtration reconstruction without invoking a spatially varying weighting factor *Medical Physics* **37**, 1201–1210.

Yu L, Zou Y, Sidky E Y, Pelizzari C A, Munro P & Xiaochuan P 2006 Region of interest reconstruction from truncated data in circular cone-beam CT *IEEE Transactions on Medical Imaging* **25**, 869–881.

Yu Z & Pan X 2004 Exact image reconstruction on PI-lines from minimum data in helical cone-beam CT *Physics in Medicine and Biology* **49**(6), 941–959.

Zhang B & Zeng G L 2007 Two-dimensional iterative region-of-interest (ROI) reconstruction from truncated projection data *Medical Physics* **34**, 935–944.

Zou Y & et al. 2005 Image reconstruction in regions-of-interest from truncated projections in a reduced fan-beam scan *Physics in Medicine and Biology* **50**(1), 13–27.